

From the clinic for Urology and Urosurgery of the Medical Faculty Mannheim

Director: Univ.-Prof. Dr. med. Maurice Stephan Michel

## Extracellular Matrix in muscle-invasive Bladder Cancer

Identification and validation of ECM related mechanisms in MIBC: A multi-omics  
analysis of a novel interpreted 3D *in vitro* model

Inaugural dissertation

For the purpose of obtaining a Doctor scientiarum humanarum (Dr. sc. hum.)

The Medical Faculty Mannheim of the Ruprecht-Karls-University to  
Heidelberg

Submitted by  
Sarah Wahby

from  
Heidelberg  
2021

Dean: Prof. Dr. med. Sergij Goerd  
Doctoral supervisor: Prof. Dr. med. Philipp Erben

Dedicated to my Ronja

# TABLE OF CONTENT

	Page
ABSTRACT.....	I
ABBREVIATIONS.....	II
1 INTRODUCTION .....	1
1.1 Bladder cancer-clinical relevance .....	1
1.2 The extracellular matrix in BC .....	2
1.3 Translational BC <i>in vitro</i> models .....	5
2 OBJECTIVES.....	8
3 MATERIAL AND METHODS .....	9
3.1 Material .....	9
3.1.1 BC cell lines .....	9
3.2 Methods .....	13
3.2.1 2D cell culture of BC cell lines.....	13
3.2.2 pH and oxygen monitoring of BC cell lines in 2D <i>in vitro</i> model.....	13
3.2.3 Primary normal bladder fibroblast-derived conditioned medium .....	13
3.3 Establishment of BC cell lines in 3D <i>in vitro</i> model.....	14
3.4 Immunofluorescence imaging of BC spheroids by confocal microscopy .....	15
3.5 Multi-omics analysis of BC 2D and 3D <i>in vitro</i> model.....	16
3.5.1 Protein mass spectrometry.....	16

3.5.2	RNA microarray .....	18
3.5.3	Python-based evaluation and <i>in silico</i> validation of multi-omics data .....	19
<b>4</b>	<b>RESULTS.....</b>	<b>21</b>
4.1	Identification of a uniform medium condition by pH and oxygen monitoring for BC cell lines	21
4.2	BC cell line establishment of an 3D <i>in vitro</i> ultra-low-attachment system.....	24
4.2.1	Evaluation of different medium conditions by spheroid growth rate .....	25
4.2.2	Identification of spheroid integrity by confocal imaging .....	27
4.2.3	Established 3D model and its final sample production .....	29
4.3	Multi-omics analysis of BC cell line spheroids .....	31
4.3.1	Global perspective of differential expressed proteins and genes.....	31
4.3.2	Evaluation of proteomic-based gene set enrichment analysis .....	35
4.3.3	ECM-based targets selection and <i>in silico</i> validation in clinical samples .....	38
4.3.4	ECM-based biological mechanisms of <i>in silico</i> validated targets.....	50
<b>5</b>	<b>DISCUSSION.....</b>	<b>51</b>
5.1	3D BC cell line <i>in vitro</i> model .....	51
5.1.1	Environmental setting for 3D <i>in vitro</i> system.....	51
5.2	Impact of UCM and CM on T24/83 spheroid formation and growth.....	53
5.3	Invasive T24 spheroids harbor particular characteristics of 3D <i>in vitro</i> models.....	55
5.4	Predomination of ECM-related malignant features and targets in the invasive T24/83 3D <i>in vitro</i> model.....	56
5.4.1	Validated ECM-based targets .....	57
5.4.2	Validated ECM-interacting targets .....	58
5.4.3	Advances and limitations of the study.....	63

6 CONCLUSION & OUTLOOK.....	65
7 REFERENCES .....	66
8 APPENDIX.....	83
9 CURRICULUM VITAE .....	91
10 ACKNOWLEDGEMENT .....	92

## ABSTRACT

Bladder cancer (BC) is the second leading cause of cancer death in the world. Treatment options for muscle-invasive bladder cancer (MIBC) are limited, with poor prognosis and incomplete molecular tumor classification posing a significant problem. BC onset and progression is highly dependent on extracellular matrix (ECM) remodeling. Moreover, the use or development of translational 3D *in vitro* models is rare in BC research, thus the mechanistically background underlying the interaction between MIBC tumor cells and ECM, as well as the identification of novel therapeutic targets and biomarker needs to be further investigated.

In this study, the BC cell lines (UROtsa, RT4, T24/83, SCaBER) were applied to the 3D *in vitro* ultra-low-attachment (ULA) method under Matrigel-free conditions. Intact spheroids were analyzed by a transcriptomic microarray and proteomic approach, and were compared to the regular used 2D model. Based on the protein level, gene set enrichment analysis was performed and pathways related to ECM proteins were identified. Resulting targets were further validated by public available mRNA sequencing data from MIBC patients. The targets gene expression was related to clinicopathological parameters, overall survival (OS), and disease-free survival (DFS).

Intact spheroid formation and growth was realized for T24/83 and RT4, while T24/83 needed the addition of 50% unconditioned fibroblast basal medium (UCM) or fibroblast conditioned medium (CM). A combination of ECM-based and -interacting targets (n=10) were significantly increased on protein level and mRNA level for the invasive T24/83 spheroids, compared to 2D culture. 6(10) targets were elevated under CM (CALU, CD109, FBN1, HTRA1, LAMC1, LRP1), 2(10) in both (P4HA2 and PLOD1), and 2(10) under UCM condition (DPYSL3 and SUMF2). Furthermore, increased levels of these targets correlated with worse OS, DFS and advanced MIBC features. Mechanistically, these targets were found to act in epithelial to mesenchymal transition (EMT), embryonic stem cell signature (ESC), neurological activity, cancer pathways, and posttranslational modification (PTM). For RT4, no ECM-related target was valid.

Spheroids of the invasive T24/83 BC cell line expressed malignant features more abundant compared to the 2D standard condition. Under CM, more targets were validated compared to UCM conditions, indicating more distinct MIBC properties under CM condition. Thus, T24/83 spheroids cultured under CM conditions can serve as a valid *in vitro* 3D model to study invasive BC mechanisms (EMT, ESC, RAF1/MAP2K1/ERK pathway, ERBB2) and treatment options for future projects. Furthermore, follow up the 10 identified ECM-related targets could lead to promising molecular biomarker or future therapeutic targets, which is urgent to improve personalized stratification, and therapy for MIBC patients.

## ABBREVIATIONS

2D	two-dimensional
3D	three-dimensional
BC	Bladder cancer
CALU	Calumenin
CD109	CD109 antigen
CM	Conditioned medium from pnBF
DEG	Differential expressed genes
DEP	Differential expressed proteins
DFS	Disease-free survival
DPYSL3	Dihydropyrimidinase-related protein 3
ECM	Extracellular matrix
EGFR	Epidermal growth factor receptor
EMT	Epithelial to mesenchymal transition
ESC	Embryonic stem cell signature
FBN1	Fibrillin-1
GSEA	Gene set enrichment analysis
HTRA1	High-temperature requirement A serine peptidase 1
ITGB3	Integrin beta-3
LAMC1	Laminin gamma 1 subunit
LRP1	Low-density lipoprotein receptor-related protein 1
MIBC	Muscle-invasive bladder cancer
OS	Overall survival
P4HA2	prolyl 4-hydroxylase subunit alpha-2
PLOD1	Procollagen-lysine,2-oxoglutarate 5-dioxygenase 1
pN	Lymph node metastasis
pnBF	Primary normal bladder fibroblasts
PTM	Posttranslational modification
SUMF2	sulfatase-modifying factor 2
TNM	Tumor- node- metastasis system
UCM	Unconditioned fibroblast basal medium
ULA	Ultra-low-attachment



# 1 INTRODUCTION

## 1.1 Bladder cancer-clinical relevance

Bladder cancer (BC) is the second leading cause of cancer death in the world. It accounts for 3% of new cancer diagnoses worldwide and is particularly prevalent in industrialized countries(1), while 2.1% of global cancer death are BC cases(2).

The majority of patients are diagnosed with BC at age 60 and older(2), indicating a disease progression that requires decades after exposure to mutagens to overcome tumor suppressor mechanisms and culminate in cancer development. Tobacco smoking is considered the greatest risk factor for BC, accounting for approximately 50%-65% new cases per year. Smoking has been shown to increase the risk of BC by three to four times. Occupational exposure to carcinogens is considered the second largest preventable risk factor for BC, including aromatic amines, polycyclic aromatic hydrocarbons, and chlorinated hydrocarbons. These compounds are frequently found in industrial manufacturing. In addition, high processed meat consumption increased the risk of BC by about 20%, caused by nitrosamines formed from nitrates which induce carcinogenesis. Also obesity is linked to BC development, while increases the risk by 10%. The protozoan schistosomiasis, which infects about 240 million humans worldwide is associated to an increased risk of squamous cell carcinoma of the bladder. It is frequently occurring in the Middle-East and Africa, where it accounts for the second most common form of cancer(1).

BC is over four times more common in men than women, with a global incidence of 9.6/100,000 in men and 2.4/100,000 in women. Since BC is the 10th most common neoplasm worldwide, it is the 13th deadliest, estimated to accounts for nearly 200,000 deaths per year. Mortality rates reflect incidence rates in terms of gender differences, with a mortality of 3.2/100,000 in men, and 0.9/100,000 in women. The observed gender discrepancy for BC incidence and mortality is likely most attributable to gender differences in smoking tobacco, which may also explain why cancer is rising among women in the developed world. Worldwide, accurate survival data on BC are rare, especially for developing countries. Using the USA as an example, the 5-year survival rate for BC is 77.1%. However, the survival rate is highly changing considering the different BC variants(1).

90% of BC cases, especially those in the developed countries are urothelial carcinoma, mainly occurring in the bladder, and less frequent in the urinary tract(3). About 80% of urothelial carcinoma correspond to the non-muscle-invasive variant, including non-invasive papillary urothelial carcinoma (pTa), carcinoma *in situ* (Cis, pTis) or invasive but non-muscle-invasive (pT1). These indicate a recurrence rate of 50%-70% but a limited potential to become muscle-invasive (10%-20%), with a 5-year survival rate of 90%(4). The remaining 20% of urothelial

carcinoma belong to the muscle-invasive variant (pT2-pT4), which can arise *de novo* or originate out of high-grade carcinoma *in situ* (pTis), with a dropped 5-year survival rate to 6%. At least 50% of muscle-invasive patients die by the reason of metastasis(5,6).

BC is a molecularly heterogeneous disease that has different clinical courses and responds to different therapies(7). High recurrence rates and intensive surveillance strategies lead to expensive costs for treatment of urothelial carcinoma, independent on its phenotype(8). Although since two decades, there was few progress in treatment of muscle invasive BC (MIBC) the patient's outcome did not change significantly(9). Consequently, the treatment of choice is based on a combination of cisplatin chemotherapy and radical cystectomy. Among other malignancies, targeting immune suppressing mechanisms has become a promising strategy for BC treatment. The PD-1 and PD-L1 antibodies showed persistent anticancer activity especially in non-responding MIBC patients to first-line cisplatin-based chemotherapy(9).

The evaluation of patient's treatment option and prognosis is based on the histological outcome of the malignant tissue obtained after tumor resection or cystectomy. According to the tumor/node/metastasis staging method, T-stage, lymph node and distant metastasis serve as the most important parameters for BC evaluation(10). However, due to observer-induced variations in visual assessment, these parameters showing limitation in their ability to accurately identify an individualized therapy strategy and predict clinical outcomes. With respect to personalized medicine, molecular identification of BC would support the implementation of tailored therapy, including valid biomarkers and patient management(11).

## 1.2 The extracellular matrix in BC

The extracellular matrix (ECM) describes a complex part of the cellular environment, and it is a dynamic network of interacting proteins, glycosaminoglycans, and proteoglycans. The ECM properties include structural function, cell-signaling responses, and cytoskeleton tension support. Its dynamic and remodeling structure constantly changes ECM interaction to cells, by influencing adhesion, expression of matrix components, growth, migration, or differentiation(12). By the interaction of cell-surface receptors with ECM components, intracellular signaling or structural changes can be induced by directly gene expression modification(13). The cellular response to the matrix can remodel the ECM structure, and leads to further interactions between the ECM and cells in a dynamic interplay(12). The ECM network also regulates the activity and release of cytokines and growth factors in a location-dependent manner. While bound to glycosylated ECM components, these factors are in a close proximity to their place of action, and their release is regulated by ECM remodeling. To get a better overview of the ECM components and their functions, *Hynes and Naba (2012)* categorized ECM components into structural molecules (the core matrisome, consists of 200 glycoproteins,

43 collagen subunits and 35 proteoglycans), and matrisome-associated components (176 ECM-affiliated proteins, 250 ECM regulators, 352 secreted factors bound to the ECM, such as matrix metalloproteinases, mucins, matrix metalloproteinase inhibitors and TGF- $\beta$ ) which possess regulating or remodeling function(14).

Since few years, there is intensive research ongoing in terms of ECM function in the bladder. Several genes or proteins were identified and found to remodel the ECM, and can be associated to BC progression and worse prognosis. The ECM composition of the basal membrane, and the submucosa have been investigated for normal and tumor tissue, however its detailed function is still not completely understood(15). Urothelial cells are lined by glycosaminoglycans (such as hyaluronic acid, heparan sulfate, heparin, chondroitin sulfate, dermatan sulfate and keratan sulfate), which serve as a barrier against urine and bacteria(16,17).

The main structural component of the ECM is collagen, providing a scaffold for proper function in the bladder(18). Particular collagens (collagen I, III, IV, VI and XII)(17) were found to occur in a specific relation in women to maintain bladder function(19). Collagen degradation is executed by collagenases which are responsible for scaffold remodeling and turnover(20,21). Based on omics technologies, the transformation of non-muscle-invasive BC to MIBC was found to be related to higher collagen expression in MIBC, indicating increased collagen stiffness in MIBC development(22,23). Collagenases such as matrix metalloproteinases have been associated with invasive potential in BC, occurrence of metastasis, and correlation to advanced progression factors and poor outcome(24–27). By evidence they play a crucial role in BC development and progression, however, they were never proofed successfully as biomarker or therapeutic target(28).

The bladder also expresses ECM-related glycoproteins as osteopontin, fibronectin, tenascin, and nidogen. Osteopontin is a matrix protein mainly expressed in bone matrix(29) but is highly associated with BC. Osteopontin was found to be overexpressed in invasive cancer compared to healthy tissue, and correlates with advanced tumors and poor prognosis. Furthermore, its expression is significantly linked to increased matrix metalloproteinase 9 and S100 calcium-binding protein A8(30,31). Osteopontin also promotes invasion and clonal growth by interacting with CD44 surface molecules on tumor cells(32). It is suggested to act via JAK1/STAT1 signaling pathway, enhance proliferation, inhibit apoptosis and promote metastasis(33). Fibronectin is a multifunctional and widely distributed glycoprotein. It interacts with components, such as collagen, fibrin, integrins and syndecans(15). Fibronectin could be of potential use as therapeutic target to treat BC. It was reported to promote cell proliferation *in vitro* and *in vivo*, including tumor formation(34,35). Tenascin-C is a large, ECM glycoprotein, and is the most intensively studied member of the tenascin family. It is rarely expressed in adult tissue but detected to be persistent expressed in cancer(36). It consists of two domains, namely domain B and C, which were significantly increased in urinary samples derived from

patients with BC progression. Further, the B domain value was identified to be able to distinguish between non-muscle-invasive and muscle-invasive outgrowth(37,38).

Laminins act through binding to integrins and interact between epithelial cells and the ECM(39). They are crucial for cell proliferation, adhesion and migration(40). In BC, staining of whole Laminin layer of the basal membrane could be used to differentiate non-invasive variants from invasive ones(41). Laminin alpha 3, a specific isoform, was reported to be higher expressed in more advanced tumors, and *in vitro* experiments linked its expression to invasion and cell motility in BC(42). Another isoform, laminin gamma 2, promoted invasive tumor growth *in vivo*(43). In combination with elastic fibers, laminins are also responsible for proper bladder function(44).

Elastin accounts to ECM proteins with structural and mechanical properties. The covalent linkage of elastin to fibrillin, fibulin and microfibril-associated glycoprotein leads to the formation of elastic fibers. This linkage is executed by the enzyme lysyl oxidase, which have been reported with elevated levels, and increased stiffness in different cancer entities in contrast to normal tissue. In addition, lysyl oxidase expression showed correlation with poor prognosis(15). However, in BC the data present contrary findings. Epigenetically silencing of lysyl-like oxidase 1 and 4, and loss of their expression was frequently observed in BC. It is suggested that lysyl-like oxidase 1 and 4 inhibit cell growth by impairing Ras/ERK signaling(45). In contrast, a high fibulin 2 expression was determined in human clinical BC tissue, and correlated with adverse pathologic features and worse patient outcomes(46).

Proteoglycans are glycoconjugates, attached to at least one glycosaminoglycan chain. They are known to occur at, the cellular surface (transmembrane syndecans or glypicans), the ECM (lecticans (aggrecan, versican, brevican and neurocan) or small leucine-rich proteoglycans (decorin, biglycan and lumican)), the basement membrane (perlecan, agrin and collagen XVIII), and intracellular (serglycin)(47). Studies have shown a relation of biglycan expression and its function as endogenous inhibitor of cell proliferation in BC. Its expression was reported to be associated with better outcome(48). Decorin, another small leucine-rich ECM proteoglycan, was found to be not expressed in *in vitro* and *in vivo* BC models, while its expression in BC patients exhibited decreased expression in malignant BC tissue(49). On the other hand, the proteoglycan versican was mechanistically related to fibrillin 1 and the ECM remodeling matrix metalloproteinases 1 and 2, thus it is suggested to be involved in BC formation and prognosis (50).

Altogether, the current data situation elucidated a lot of ECM-related components for BC so far, however there is more research necessary to study the mechanistically interplay between the ECM and the bladder tissue cells. In the current time, where omics technologies are frequently more applied, in-depth investigation of the ECM and its underlining dysregulation in BC is possible. The highly dynamic features of the ECM compartment are crucial factors

associated to epithelial to mesenchymal transition (EMT), invasive cell motility, proliferation, and cancer signaling, as erb-b2 receptor tyrosine kinase 2/ erb-b2 receptor tyrosine kinase 3(51). As a consequence, the ECM has a distinct impact on BC onset and malignant progression(52) that is not to be neglected. Thus, the compartment offers a promising platform for future investigations of valid biomarker and new treatment strategies for BC.

### 1.3 Translational BC *in vitro* models

The heterogeneous nature of BC and the clearly impact of the ECM on BC onset and progression require meaningful and valid *in vitro* models to generate transferable knowledge of BC pathology from the lab to the clinic. In general, cellular-based *in vitro* systems are a very common tool in translational research. Traditionally, adherent cells are cultured in a 2D (two-dimensional) orientation, which can be entitled as gold standard of *in vitro* systems, by offering a standardized, less complex, and cost effective approach. However, culturing cells in a planar orientation surely lacks cellular arrangements, and the interaction with the ECM compared to the physiology of an organism(53). Recently, the methodology of de-cellularization of whole rodent organs, including the urinary bladder, displayed native 3D (three-dimensional) ECM scaffolds with preserved structure and composition(54). Another group demonstrated a de-epithelialized rat bladder as *in vitro* model to study BC invasion to enable ECM interaction with tumor cells(55). The application of animal-based experiments could fix the lack of physiology but is connected to highly costs, specialized skills and strict legal regulations. Thus, it was of significant advance when patient-derived BC tissue was cultured as organoids *in vitro*. This method allows the maintenance of individual tumors to identify best treatment options *in vitro*, and reanalyze the tissue at later time points as required(56). A very comprehensive study from 2018 investigated an entire biobank of BC organoids, which reflected molecular and histopathological diversity of the disease, and validated personalized drug response and associated resistance *in vivo*(57). BC patient-derived organoids demonstrate a promising approach to improve patient treatment and surveillance, however, due to its dependency on clinical post-surgery tissue samples, organoids harbor a limiting factor for intensive BC research. Apart from patient-derived *in vitro* models, several 3D *in vitro* applications with established cell lines were developed by diverse techniques. For instance, 3D microfluidic devices or 3D gelatin-based bio-printed scaffolds were used for *in vitro* mono- or co-culture of BC. These models enable a platform for drug screening(58), the measurement of cell-cell interactions(59), to study migration and proliferation of metastatic BC cell lines(60), and the communication between cancer cells and fibroblasts(61). Furthermore, a 3D vesical-like structure was engineered from primary human endothelial cells, and BC spheroids were incorporated to investigate invading cells(62). In consideration to reduced animal-based experiments, these models are of big advantage, however they remain complex and elaborate,

while specific equipment and skills are needed. To overcome these barriers, 3D *in vitro* spheroids can be cultured by far simpler applications, and were already described to show more similarities to physiological conditions in several cancer-related studies(63). Hence, spheroid-based 3D *in vitro* models can be applied to better recapitulate the phenotypic and cellular heterogeneity. In addition, the incorporation of the ECM supports the reflection of realistic tumor conditions and characteristics. Spheroids are being easy to develop and more flexible to conduct repeated experiments. Compared to the 2D culture model, the diffusion of nutrients and oxygen to the inner zones of spheroids is limited. Therefore, hypoxia, one of the major hallmarks of solid tumors, can be caused in spheroids larger than 1–2mm(53).

Vasyutin *et al.* (2019) summarized the semiliquid technique (seeding cells on pre-coated agarose plates) as the most applied spheroid technique for BC so far(64). As an example, the accumulation of a photosensitizer and its therapeutic effect was investigated in normal and carcinoma cell line, grown as spheroids on agarose(65). To generate single and uniformly sized spheroids, the semiliquid overlay method seems to be inadequate, since the formation of multiple spheroids of different size were observed(66). Two other used techniques, namely hanging-drop method and ultra-low-attachment (ULA )method, were investigated using the RT4 cell line(67). The authors observed for the spheroid treatment with doxorubicin a higher drug resistance in comparison to 2D culture within a similar concentration for both methods. However, due to the lower working volume of the hanging-drop method (40µl), larger spheroids can be produced by the ULA method, and keeping the spheroids moisturized could be challenging for long term culture. Thus, the authors mentioned the ULA method as more straightforward(67). The ULA method belongs to the forced-floating methods, and provides a non-adherent surface, thus the cells have the only possibility to attach to each other, and form a spherical arrangement. This principle was previous used in BC research for high-throughput drug screening(68) and BC subtype expression in comparison to 2D culture(69). This recent study demonstrated a stronger expression of the luminal subtype in 3D, showed a reduced proliferation rate, and were therefore less sensitive to cisplatin and gemcitabine, in contrast to 2D culture(69). Moreover, the ULA method is also applicable for co-culturing, which was published as 3D BC invasion model(70). They co-cultured tumor with stroma cells (fibroblasts and immune cells), and enriched the ECM components derived from rat tail to reflect *in vivo* conditions occurring in the BC microenvironment. Due to the current knowledge, the ULA application was chosen because of few advantages. The use of ULA microplates is less complex in handling, less time consuming, and exhibits moderate costs compared to other 3D *in vitro* systems. Moreover, the ULA platform is highly reproducible in terms of high-throughput production and the uniformly growth of single spheroids. In addition, spheroids would be not incorporated into solid phases, which could be challenging to remove for further analysis. The ULA method was proved to represent gene expression and biology of BC more realistic

compared to 2D *in vitro* system(71), and was previously applied only rarely in translational BC research.

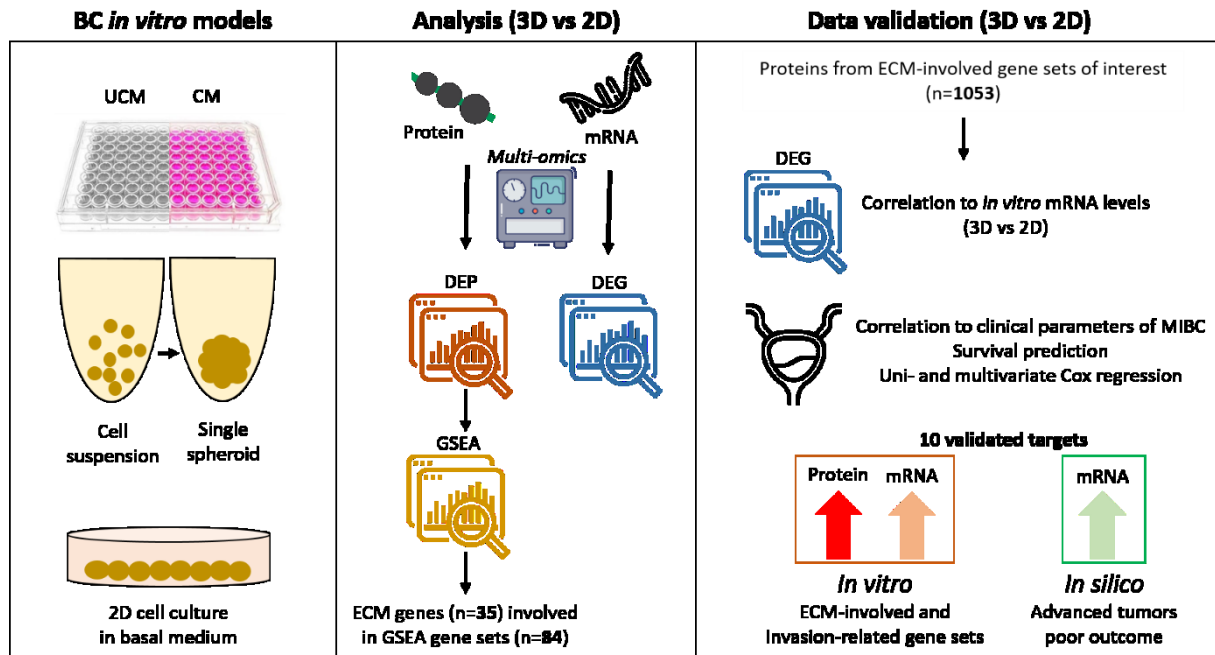
## 2 OBJECTIVES

Since the onset of BC and malignant progression, as invasion and metastasis, to MIBC is highly dependent on ECM remodeling. Treatment options for patients are restricted, why poor prognosis is a significant problem, and BC molecular classification is incomplete so far. Furthermore, the use and development of translational 3D *in vitro* models is rare in BC research, hence valid models are needed to study the mechanistically background underlying BC tumor cells and ECM interaction. Equally, the identification of novel therapeutic targets and biomarker needs to be further investigated.

Considering these facts, in this study a series of different BC cell lines (UROtsa, RT4, T24/83, SCaBER) was cultured by the 3D *in vitro* ULA method, and needed to be established by ECM-related medium compositions. To keep pace with the times, valid spheroids were analyzed by a microarray transcriptomic and proteomic approach, compared to the 2D model. Based on the protein level, Gene Set Enrichment Analysis (GSEA) was performed and pathways related to the ECM were identified. As result, 10 ECM-based and –interacting targets were significantly differential expressed on protein level, mRNA level, and correlated with worse survival and advanced features in MIBC patients. Mechanistically, these targets act in EMT, embryonic stem cell signature (ESC), neurological activity, cancer pathways, and posttranslational modifications (PTM).



### 3 MATERIAL AND METHODS



Experimental and analytical scheme

#### 3.1 Material

##### 3.1.1 BC cell lines

**UROtsa** was established from the urothelium lining ureter of a 12-year old girl and immortalized by temperature-sensitive SV40 large T-antigen gene construct. This cell line provides an *in vitro* model of normal urothelium, because *in vitro* they show no malignant transformation, like growth in soft agar or tumorigenicity in nude mice. Additionally, chromosomal appearance and number was observed to be normal in metaphase(72). UROtsa cell line was provided by Prof. Dr. med. Ruth Knüchel-Clarke (University medical center Regensburg, now in RTWH Aachen). The transitional cell papilloma cell line **RT4**, derived from a 62-years old male patient with a recurring papillary tumor of the bladder, in 1970(73). The cell line is characterized by aneuploidy with a modal chromosome number of 49 with four marker chromosomes identified. RT4 has been shown tumorigenic potential in cheek pouch of steroid-treated hamsters. The cell line was purchased from ATCC.

**T24/83** is a derivative of the *in vitro* established T24 cell line. T24 originates from an 82-years old Swedish male patient diagnosed with a G3 urothelial carcinoma, in 1970(74). The generation time constitutes of about 19 h and exhibit a disordered multilayer growth with chromosomal hypodiploid to hypopentaploid characteristics. Tumorigenic potential was confirmed in hamster cheek pouches but not in nude mice. T24/83 cells were purchased from *European Collection of Authenticated Cell Cultures* (ECACC).

In 1976, **SCaBER** was established from a squamous cell carcinoma of the urinary bladder. The cell line derived from a 58-years old patient and retained morphological properties of the tumor for 40 passages *in vitro*(75). The chromosome number is hypotetraploid with thirteen marker chromosomes and a male karyotype. SCaBER is tumorigenic and forms epidermoid carcinoma in nude mice. The cell line was purchased from ATCC.

In 1982, **UMUC-3** cells derived from a human male urothelial bladder carcinoma(76) and are known to be tumorigenic in nude mice when  $10^7$  cells administrated subcutaneously. These cells exhibit a hypertriploid karyotype with a modal chromosome number of 78-80 and 30 or more marker chromosomes. UMUC-3 was purchased from *European Collection of Authenticated Cell Cultures* (ECACC).

**RT112/84** is a derivate of the *in vitro* RT112 cell line, which was established from female patient diagnosed with G1-2 urothelial bladder carcinoma, in 1973(77). Cells show no density-dependent growth inhibition and are able to form tumors in nude mice, but did not grow in soft agar(78). RT112/84 cells were purchased from *European Collection of Authenticated Cell Cultures* (ECACC).

<b>Cell lines</b>	<b>Supplier</b>
UROtsa passage 60-66	RWTH Aachen University, Germany
RT4 passage 19-23	ECACC, Salisbury, England (91091914)
T24/83 passage 13-17	ECACC, Salisbury, England (85061107)
SCaBER passage 27-33	ATCC, Wesel, Germany (HTB-3)
RT112/84 passage 19-25	ECACC, Salisbury, England (85061106)
UMUC-3 passage 14-20	ECACC, Salisbury, England (96020936)
Primary normal bladder fibroblasts	ATCC, Wesel, Germany (PCS-420-013)
<b>Media and supplements</b>	<b>Supplier</b>
RPMI, 2 mM glutamine	GIBCO, Waltham, MA, USA
DMEM, 2 mM glutamine	GIBCO, Waltham, MA, USA
Mc Coy's, 2 mM glutamine	GIBCO, Waltham, MA, USA
Fetal bovine serum (FBS)	Sigma-Aldrich, Steinheim, Germany
Fibroblast Basal Medium	ATCC, Wesel, Germany
Fibroblast Growth Kit-Low serum	ATCC, Wesel, Germany
<b>Chemicals and reagents</b>	<b>Supplier</b>
Trypsin neutralizing solution	Promocell,, Heidelberg, Germany
1x PBS (-Ca <sup>2+</sup> , -Mg <sup>2+</sup> ) pH 7.0-7.3	GIBCO, Waltham, MA, USA
1x PBS (+Ca <sup>2+</sup> [0.90mM], +Mg <sup>2+</sup> [0.49mM]) pH 7.0-7.2	GIBCO, Waltham, MA, USA
RNAse free water	BRAUN, Melsungen, Germany
96-100 % Ethanol	Carl Roth, Karlsruhe, Germany
0.4% Trypan blue	Logos Biosystems, Villeneuve d'Ascq, France
Paraformaldehyde (PFA)	Carl Roth, Karlsruhe, Germany
4',6-diamidino-2-phenylindole (DAPI)	Sigma-Aldrich, Steinheim, Germany
Triton X-100	Carl Roth, Karlsruhe, Germany
Glycine	Carl Roth, Karlsruhe, Germany
Glycerol	Carl Roth, Karlsruhe, Germany

Bovine serum albumin (BSA)	Carl Roth, Karlsruhe, Germany
Tween20	Sigma-Aldrich, Steinheim, Germany
Heparin	Sigma-Aldrich, Steinheim, Germany
Dimethyl sulfoxide (DMSO)	Carl Roth, Karlsruhe, Germany
Protease inhibitor cocktail	Sigma-Aldrich, Steinheim, Germany (5056489001)
Ammonium Bicarbonate (ABC)	Fluka Analytical, Munich, Germany (40867; Lot: I1620)
Sodium-dodecylsulfate (SDS)	Applichem, Darmstadt, Germany (A0675)
Tris(2-carboxyethyl)phosphine (TCEP)	Sigma-Aldrich, Steinheim, Germany (C4706)
Chloroacetamide (CAA)	Sigma-Aldrich, Steinheim, Germany (22790; Lot: BCBN8771V)
Acetonitrile (ACN)	Biosolve Chemicals, Dieuze, France (0001204101BS; Lot: 1274241)
Ethanol (EtOH)	Merck, Darmstadt, Germany (34852)
Trifluoroacetic acid (TFA)	Biosolve Chemicals, Dieuze, France (0020234131BS; Lot: 1273961)
Formic acid (FA)	Biosolve Chemicals, Dieuze, France (0006914143BS; Lot: 1297891)
Beads (Magnetic Carboxylate Modified): Sera-Mag Speed Beads A, slurry at 50 µg/µl Sera-Mag Speed Beads B, slurry at 50 µg/µl	Thermo Fisher Scientific, Waltham, MA, USA (24152105050250) (44152105050250)
<b>Enzymes &amp; antibodies</b>	<b>Supplier</b>
0.25 % Trypsin-EDTA (1x)	GIBCO, Waltham, MA, USA
0.04% Trypsin-0.03% EDTA	Promocell, Heidelberg, Germany
Sequencing Grade Modified Trypsin	Promega, Walldorf, Germany (V5111)
DNase I Ambion™	Thermo Fisher Scientific, Waltham, MA, USA
Anti-KI67 rabbit, polyclonal antibody	Merck, Darmstadt, Germany (SAB4501880)
Anti-Cas3 rabbit, polyclonal antibody	Cell Signaling Technology, Danvers, MA, USA (9661)
Goat anti-rabbit polyclonal Alexa Fluor 647	Thermo Fisher Scientific, Waltham, MA, USA (A21246)
<b>Kits</b>	<b>Supplier</b>
Bicinchoninic acid assay (BCA)	Thermo Fisher Scientific, Waltham, MA, USA (23225; Lot: SL258365)
RNeasy mini kit	Qiagen, Hilden, Germany
GeneChip® WT Plus Reagent Kit	Thermo Fisher Scientific, Waltham, MA, USA
GeneChip® Hybridization, Wash and Stain Kit	Thermo Fisher Scientific, Waltham, MA, USA
<b>Instruments</b>	<b>Supplier</b>
Incubator	Thermo Fisher Scientific, Waltham, MA, USA
Water bath	GFL, Burgwedel, Germany
Centrifuge (50 ml, 15 ml tubes)	Eppendorf, Hamburg, Germany
Table centrifuge (0.2 ml-2 ml tubes)	Eppendorf, Hamburg, Germany
Thermomixer	HTA-BioTec, Bovenden, Germany
Nanodrop 1000	VWR, Darmstadt, Germany
Vortex (MS1 Minishaker)	IKA-Werke, Staufen, Germany
Centrifuge (96 well plates)	Hettich Lab Technology, Tuttlingen, Germany
LUNA-FL dual fluorescence cell counter	Logos Biosystems, Villeneuve d'Ascq, France
Axio Vert. A1 microscope	Zeiss, Oberkochen, Germany
SDR SensorDish® reader	PreSens Precision Sensing, Regensburg, Germany
SP8 confocal microscope	Leica Geosystems, Munich, Germany
S-250D Model Sonifier	Branson Ultrasonic Corporation, Danbury, CT, USA
In-house built magnet for PCR tubes	DKFZ, Heidelberg, Germany

Easy NanoLC 1200	Thermo Fisher Scientific, Waltham, MA, USA
Acclaim PepMap C18, 5 $\mu\text{m}$ , 100 $\text{\AA}$ , 100 $\mu\text{m}$ x 2cm	Thermo Fisher Scientific, Waltham, MA, USA
nanoEase MZ Peptide BEH C18 130 $\text{\AA}$ , 1.7 $\mu\text{m}$ , 75 $\mu\text{m}$ x 250 mm	Thermo Fisher Scientific, Waltham, MA, USA
Q-Exactive HF Orbitrap mass spectrometer	Thermo Fisher Scientific, Waltham, MA, USA
Pico-Tip Emitter 360 $\mu\text{m}$ OD x 20 $\mu\text{m}$ ID; 10 $\mu\text{m}$ tip	New Objective, Littleton, MA, USA
Agilent 2100 bioanalyzer	Agilent, Santa Clara, CA, USA
GeneChip Hybridization oven 640	Affymetrix, High Wycombe, UK
GeneChip Fluidics Station 450	Affymetrix, High Wycombe, UK
GeneChip Scanner 3000	Affymetrix, High Wycombe, UK
<b>Web source and Software</b>	<b>Web presence</b>
MATLAB vR2020b	<a href="https://www.mathworks.com/products/matlab.html">https://www.mathworks.com/products/matlab.html</a>
Python v3.8.1	<a href="http://www.python.org">www.python.org</a>
RStudio v1.1.456	<a href="https://rstudio.com/">https://rstudio.com/</a>
R v3.4.0	<a href="https://cran.r-project.org/">https://cran.r-project.org/</a>
Custom CDF Version 22	<a href="http://brainarray.mbni.med.umich.edu/Brainarray/Database">http://brainarray.mbni.med.umich.edu/Brainarray/Database</a>
Leica Application Suite X	<a href="https://leica-geosystems.com">https://leica-geosystems.com</a>
ImageJ	<a href="https://imagej.nih.gov/ij/">https://imagej.nih.gov/ij/</a>
cBioPortal	<a href="http://www.cbioportal.org">www.cbioportal.org</a>
SAS JMP v13	<a href="http://www.jmp.com">www.jmp.com</a>
SAS JMP10 Genomics v15	<a href="http://www.jmp.com">www.jmp.com</a>
Kaplan-Meier Plotter	<a href="https://kmplot.com/analysis/">https://kmplot.com/analysis/</a>
MaxQuant v1.5.1.2	<a href="https://www.maxquant.org/">https://www.maxquant.org/</a>
Uniprot	<a href="http://www.uniprot.com">www.uniprot.com</a>
MSigDB	<a href="https://www.gsea-msigdb.org/gsea/msigdb/">https://www.gsea-msigdb.org/gsea/msigdb/</a>
GraphPad Prism v5	<a href="http://www.graphpad.com">www.graphpad.com</a>
Microsoft Excel 2013	<a href="http://www.Microsoft.com">www.Microsoft.com</a>
<b>Consumables</b>	<b>Supplier</b>
Sterile 0.2ml, 0.5ml, 1.5ml, 2ml RNase free tubes	Biozym Hessisch, Oldendorf, Germany
Sterile conical centrifuge tubes (15ml, 50ml)	Greiner Bio-One, Frickenhausen, Germany
Microliter-pipettes	Gilson, Middleton, WI, USA
Sterile filter tips (1 $\mu\text{l}$ -1000 $\mu\text{l}$ )	Starlab, Hamburg, Germany
Sterile one-way plastic pipettes (2ml, 5ml, 10ml, 25ml)	Greiner Bio-One, Frickenhausen, Germany
Cell culture flasks (25cm <sup>3</sup> , 75cm <sup>3</sup> , 175cm <sup>3</sup> )	Greiner Bio-One, Frickenhausen, Germany
syringe (1ml, 20ml)	Braun, Melsungen, Germany
20 G needle	Braun, Melsungen, Germany
6-well OHD6 SDR plates	PreSens Precision Sensing, Regensburg, Germany
96-well ULA plates	Greiner Bio-One, Frickenhausen, Germany
18-well $\mu$ -slides	IBIDI, Planegg, Germany
Affymetrix HuGene-2_0-st-type	Thermo Fisher Scientific, Waltham, MA, USA

## 3.2 Methods

### 3.2.1 2D cell culture of BC cell lines

The BC cell lines UROtsa, RT4, T24/83, UMUC-3, RT112/84 and SCaBER were thawed and cultured in their respective medium until they recovered from freezing procedure (Table 1), at 5 % CO<sub>2</sub> and 37°C. The medium was changed every second day and cells were passaged at 80 % to 90 % confluence. Since different medium conditions were used, each cell line was adapted to new conditions by at least three passages until experiments were carried out. All cell lines were positively authenticated and negatively tested on mycoplasma by Multiplexion (Heidelberg, Germany).

### 3.2.2 pH and oxygen monitoring of BC cell lines in 2D *in vitro* model

BC cell lines (UROtsa, RT4, UMUC-3, RT112/84, T24/83) were adapted to different media conditions (RPMI + 5 % FBS, Mc Coy's + 10 % FBS, DMEM + 10 % FBS), and 3 ml of 1.5x10<sup>4</sup> cells/ml were seeded in 2 replicates onto 6 well OxoHydroDish (OHD)6 plates (PreSens). Cells were placed onto the Sensor Dish Reader (PreSens) within the incubator, at 5 % CO<sub>2</sub> and 37°C, and pH was monitored online every five minutes for four days. Medium was changed once, two days after seeding.

Raw data were transferred to the data analysis excel sheet, provided by the manufacture, and for every time point O<sub>2</sub> concentrations were calculated from the simultaneously monitored pH and temperature values. The pH and oxygen variation was statistically evaluated by two-way ANOVA (Bonferroni posttests) compared to medium controls. Graphs were designed and statistics were calculated using GrapPad Prism version 5.

### 3.2.3 Primary normal bladder fibroblast-derived conditioned medium

Primary normal bladder fibroblasts (pnBF) were thawed and cultured in unconditioned fibroblast basal medium (UCM) from passage 9-11, supplemented with Fibroblast Growth Kit-Low Serum, at 5 % CO<sub>2</sub> and 37°C. Medium was exchanged every two days until 80 % to 90 % confluence. pnBF were expanded to T175 cm<sup>3</sup> cell culture flasks at a ratio of 1:6 and provided with 20 ml of growth medium per flask. After 48 h of growth, conditioned culture medium was removed, collected into 50 ml conical centrifuge tubes and centrifuged at 300 g for 5 min. Supernatant was tipped off into fresh 50 ml conical centrifuge tubes and was used in a timely manner. Conditioned medium from pnBF (CM) was consumed within one week, and stored at 4°C in the meantime.

### 3.3 Establishment of BC cell lines in 3D *in vitro* model

The cell lines UROtsa, RT4, T24 and SCaBER were adapted to different standard media (McCoy's + 10 % FBS, DMEM + 10 % FBS) or further compositions (Table 1) in 2D culture, and 100  $\mu$ l cell suspension per well were seeded onto 96-well ULA plates. Each well was filled up by 100  $\mu$ l medium, dependent on used condition. The applied cell counts for each cell line are depicted in Table 8 and ranged from  $10^3$ - $4 \times 10^5$  cells/ml. 3D cultures were maintained for 4-16 days at 5 %CO<sub>2</sub> and 37°C. 100  $\mu$ l medium was changed every second day. Spheroids were imaged microscopically every day to observe spheroid integrity. Spheroid growth rates were analyzed by daily taken images using the MATLAB extension Spheroid Sizer(79). Graphs were prepared with GraphPad Prism version 5.

**Table 1: Supplier recommended and additionally used medium conditions for BC cell lines.**

BC cell line	Standard medium	Further conditions used
SCaBER	MEM + 10 % FBS	50 % CM + 50 % (Mc Coy's + 10 % FBS)
RT4	Mc Coy's + 10 % FBS	50 % UCM + 50 % (Mc Coy's + 10 % FBS) 50 % CM + 50 % (DMEM + 10 % FBS)
T24/83	Mc Coy's + 10 % FBS	50 % UCM + 50 % (DMEM + 10 % FBS) 50 % CM + 50 % (Mc Coy's + 10 % FBS)
UROtsa	RPMI + 5 % FBS	+ DNase treatment*
UMUC-3	DMEM + 10 % FBS	No further conditons
RT112/84		

\*In 2D culture, cells were adapted to 50 % CM + 50 % (Mc Coy's + 10 % FBS) growth condition, treated with 0.1 mg/ml DNase, and incubated 30 min at RT prior to seeding into 3D culture.

### 3.4 Immunofluorescence imaging of BC spheroids by confocal microscopy

BC spheroids were stained, cleared and imaged according to *Nürnberg et al. (2020)*(80). The optical clearing procedure of the BC spheroids was carried out according to the Glycerol method. Immunofluorescence was performed using primary anti-KI67 (Merck, Darmstadt, Germany) and anti-Cas3 (Cell Signaling Technology, Danvers, MA, USA) antibodies, diluted 1:300 and 1:400, respectively. Fluorescence staining was performed using polyclonal goat anti-rabbit Alexa Fluor 647 (Thermo Fisher Scientific, Waltham, MA, USA) secondary antibody, 1:800 diluted, and nuclear staining was conducted with DAPI (Sigma Aldrich) 1:500 diluted. Antibodies were prepared in antibody solution (1 % BSA, 0.2 % Tween20 10 µg/mL Heparin, 5 % DMSO in PBS) for spheroid staining.

In brief, about 20-24 spheroids were collected in 1.5 ml reaction tubes and washed 3 x with PBS and fixed in 4 % paraformaldehyde (PFA) for 1 h at 37°C. Afterwards, spheroids were washed 3 x with PBS, transferred into 200 µl PCR tubes, and stored at 4°C in PBS until preparation for immunofluorescence was performed. After fixation, spheroids were incubated in PBS with 2 % Triton X-100 for 5 min at RT, and afterwards incubated for 30 min at 37°C in penetration buffer (0.2 % Triton X-100, 0.3 M Glycine, 20 % DMSO in PBS). Spheroids were blocked for 2 h at 37°C in blocking buffer (0.2 % Tween20, 10 µg/mL Heparin in PBS), and primary antibodies were incubated at 37°C ON. Spheroids were washed 5 x 15 min (0.2 % Tween20, 10 µg/mL Heparin in PBS), and secondary antibody was incubated ON at 37°C. Furthermore, spheroids were cleared in 88 % Glycerol ON at 37°C and mounted on 18-well µ-slides (IBIDI, Planegg, Germany). Five spheroids of each condition were imaged and analyzed

followed by sum projection of the z-stacks of 160  $\mu\text{m}$  size, and a z-step size of 1  $\mu\text{m}$ , while fluorescence signals were normalized to mean spheroid size for multiple comparisons. Differences were determined by two-way ANOVA and graphs were generated by GraphPad Prism version 5.

### 3.5 Multi-omics analysis of BC 2D and 3D *in vitro* model

#### 3.5.1 Protein mass spectrometry

BC cells from 2D culture (T75  $\text{cm}^2$  flasks) were detached with 3 ml 0.25 % Trypsin (Gibco) and reaction was stopped by the addition of 3 ml Mc Coys + 10 % FBS. Cell suspension were transferred into a 15 ml conical centrifuge tube and centrifuged for 5 min at 300 x g. Pellets were washed 3 x with PBS and split 50:50 into 1.5 ml reaction tubes. About 50-70 spheroids were collected into one 1.5 ml reaction tube, washed 3 x with PBS, and dry spheroids and pellets were stored at  $-80^\circ\text{C}$  until further procedure.

Samples were reconstituted in 100  $\mu\text{L}$  lysis buffer (4 % SDS, 100 mM ABC pH 8.5, and 1 x protease inhibitor cocktail (PIC)) and stored on ice during the subsequent homogenization steps. Each sample was probe-sonicated 2 x 15 s at 10 % frequency and 2 x 15 s at 10 % frequency with cooling on-ice between cycles. Samples were centrifuged at 15.000 x g, at  $4^\circ\text{C}$  for 30 min to pellet remaining cell- and tissue debris, followed by protein quantification using a Bicinchoninic acid assay (BCA) (Thermo Fisher Scientific). For each sample, 10  $\mu\text{g}$  of protein were processed in a total volume of 13.3  $\mu\text{L}$  of 1 % SDS, 100 mM ABC, 10 mM TCEP, and 40 mM Chloroacetamide. Samples were heated for 5 min at  $95^\circ\text{C}$  to denature proteins, and to reduce and alkylate cysteine residues. Cooled to room temperature, samples were further processed by Single-Pot Solid-Phase-enhanced Sample Preparation (SP3) sample clean-up procedure(81). In brief, 2  $\mu\text{L}$  of pre-washed beads (100  $\mu\text{g}/\mu\text{L}$  of Sera-Mag Speed Beads A and B, washed 1 x with 160  $\mu\text{L}$  and 2x with 200  $\mu\text{L}$  ddH<sub>2</sub>O) and 15.2  $\mu\text{L}$  100 % ACN were added to each sample to reach a final concentration of 50 % organic. Protein binding to the beads was allowed for 18 min off a magnetic rack, followed by 2 min incubation on a magnetic rack to immobilize beads. The supernatant was removed and beads were washed 2 x with 200  $\mu\text{L}$  of 100 % EtOH and 1 x with 180  $\mu\text{L}$  of 100 % ACN. Beads were re-suspended in 12  $\mu\text{L}$  100 mM ABC and sonicated for 5 min in a waterbath. Finally, sequencing-grade trypsin was added at an enzyme/protein ratio of 1:40 and beads were pushed from the tube walls into the solution to ensure efficient digestion. Upon overnight incubation at  $37^\circ\text{C}$  and 1000 rpm in a table-top thermomixer, samples were acidified to a final concentration of 0.5 % TFA and quickly vortexed. Peptides were recovered by immobilizing the beads on a magnetic rack and transferring the supernatant to new PCR tubes. MS injection-ready samples were stored at  $-20^\circ\text{C}$ .



Samples were diluted with Buffer A (0.1 % FA in ddH<sub>2</sub>O) to enable the injection of 1 µg peptide. Peptides were separated using the Easy NanoLC 1200 (Thermo Fisher Scientific) fitted with a trapping (Acclaim PepMap C18, 5 µm, 100 Å, 100 µm x 2 cm) and an analytical column (nanoEase MZ Peptide BEH C18 130 Å, 1.7 µm, 75 µm x 250 mm). The outlet of the analytical column was coupled directly to a Q-Exactive HF Orbitrap (Thermo Fisher Scientific) mass spectrometer. Solvent A was ddH<sub>2</sub>O, 0.1 % (v/v) FA and solvent B was 80 % ACN in ddH<sub>2</sub>O, 0.1 % (v/v) FA. The samples were loaded with a constant flow of solvent A at a maximum pressure of 800 bar, onto the trapping column. Peptides were eluted via the analytical column at a constant flow of 0.3 µl/min, at 55°C. During the elution, the percentage of solvent B was increased in a linear fashion from 3 to 8 % in 4 min, then from 8 % to 10 % in 2 min, then from 10 % to 32 % in a further 68 min, and then to 50 % B in 12 min. Finally, the gradient was finished with 8 min at 100 % solvent B, followed by 11 min 97 % solvent A. Peptides were introduced into the mass spectrometer via a Pico-Tip Emitter 360 µm OD x 20 µm ID; 10 µm tip (New Objective, Littleton, MA, USA) and a spray voltage of 2 kV. The capillary temperature was set at 275°C. Full scan MS spectra with mass range m/z 350 to 1500 were acquired in the Orbitrap with a resolution of 60.000 FWHM. The filling time was set to a maximum of 32 ms with an automatic gain control target of 3 x 10<sup>6</sup> ions. The top 20 most abundant ions per full scan were selected for an MS<sub>2</sub> acquisition. The dynamic exclusion list was with a maximum retention period of 40 s. Isotopes, unassigned charges, and charges of 1, 5 to 8, and >8 were excluded. For MS<sub>2</sub> scans the resolution was set to 15.000 FWHM with an automatic gain control of 1 x 10<sup>5</sup> ions and maximum fill time of 50 ms.

Raw files were processed using MaxQuant version 1.5.1.2(82). The search was performed against the human Uniprot database (20170801\_Uniprot\_homo-sapiens\_canonical\_reviewed; 20214 entries) using the Andromeda search engine with the following search criteria: enzyme was set to trypsin with up to 2 missed cleavages. Carbamidomethylation (C) was selected as a fixed modification; oxidation (M) and acetylation (protein N-term) were set as variable modification(82,83). First and second search peptide tolerance were set to 20 and 4.5 ppm, respectively. Matching of identifications between runs was performed with a match time window set to 0.3 min and a default alignment window of 20 min. Unidentified features were not matched. The protein quantification was performed using the label-free quantification (LFQ) algorithm of MaxQuant. LFQ intensities were calculated using a minimum ratio count of 2, and minimum and average number of neighbors of 3 and 6, respectively. No MS/MS were required for the LFQ comparison. Peptide and protein hits were filtered at a false discovery rate of 1 %, with a minimal peptide length of 7 amino acids. The reversed sequences of the target database were used as a decoy database. LFQ values were extracted from the protein Groups table and log<sub>2</sub> transformed for further analysis. All consecutive steps were performed in Microsoft Excel 2013, Perseus, and the statistical software environment R(84,85). Differential

expressed proteins (DEP) were relatively identified between each 3D condition compared to 2D standard condition, and determined by limma software package in R(86). P-values were adjusted according to Benjamini and Hochberg(87).

GSEA was used to analyze whether defined sets of genes exhibit a statistically significant bias in their distribution within a ranked gene list using the fgsea package(88). Reactome, KEGG, and MSigDB, as hallmark and oncogenic signatures, databases were used to annotate gene sets to pathways belonging to various cell functions. All statistical procedures were conducted with the R programming language running under the open-source computer software R v3.4.0(84) and RStudio v1.1.456(89). Results were visualized using GraphPad prism version 5, and Microsoft Excel 2013.

### 3.5.2 RNA microarray

2D cell culture (T75 cm<sup>2</sup> flasks) were washed once with 10 ml PBS, and cell lysis was performed with 700 µl lysis buffer (RNeasy Mini Kit, Qiagen) per flask directly. Lysate was split 50:50 into 1.5 ml reaction tubes. About 50-70 spheroids were collected into 1.5 ml reaction tubes, washed 3 x with PBS, and 350 µl lysis buffer was added. Lysates were stored at – 80°C until further procedure.

Total RNA of BC spheroids from 3D, and 2D culture was prepared using RNeasy Mini Kit (Qiagen, Hilden, Germany), according to the manufactures protocol. Afterwards, isolated RNA was treated with 1µl DNase I (Thermo Fisher Scientific) per 10µg RNA, and incubated for 30min at 37°C. RNA integrity was determined by capillary electrophoresis on an Agilent 2100 bioanalyzer (Agilent, Santa Clara, CA, USA) and high quality was confirmed.

Gene expression profiling was performed using arrays of human HuGene-2\_0-st-type from Affymetrix (Thermo Fisher Scientific). Biotinylated antisense cDNA was then prepared according to the standard labelling protocol with the GeneChip® WT Plus Reagent Kit and the GeneChip® Hybridization, Wash and Stain Kit (both from Thermo Fisher Scientific). Afterwards, the hybridization on the chip was performed on a GeneChip Hybridization oven 640, then dyed in the GeneChip Fluidics Station 450 and thereafter scanned with a GeneChip Scanner 3000. All of the equipment used was from the Affymetrix-Company (Affymetrix, High Wycombe, UK).

A Custom CDF Version 22 with ENTREZ based gene definitions was used to annotate the arrays(90). The raw fluorescence intensity values were normalized applying quantile normalization and RMA background correction. One-way ANOVA was performed to identify differential expressed genes (DEG) of each 3D condition in relation to 2D standard condition using a commercial software package SAS JMP10 Genomics, version 15, from SAS (SAS Institute, Cary, NC, USA). A false positive rate of  $\alpha=0.05$  with FDR correction was taken as the

level of significance. Results were visualized using GraphPad prism version 5, and Microsoft Excel 2013.

### 3.5.3 Python-based evaluation and *in silico* validation of multi-omics data

Significant results from the GSEA were filtered for ECM-related gene sets (n=6), and detected ECM-related proteins were extracted from the MS data (n=35), and matched against all significant GSEA-identified gene sets. The resulting gene sets (n=84) indicated the involvement of ECM-related proteins in their respective pathways relevant for ECM-related cancer characteristics. In addition, log<sub>2</sub> fold change and adjusted p-value from DEP and DEG data were supplemented to show correlations between MS and MA data.

Public available MIBC mRNA sequencing data from the Cancer Genome Atlas (TCGA, Cell 2017)(91) were used to validate the multi-omics *in vitro* data. All detected DEP, related to ECM, PTM, EMT, ESC, neuronal, and cancer-related pathways (n=1053) from GSEA were correlated to the *in silico* cohort (Table 2) in terms of age, gender, lymph node metastases (pN0-3), tumor- node- metastasis system (TNM staging), survival status (alive, deceased), and recurrence status (recurred, not recurred). Since only MIBC were analyzed, patients with a TNM stage <T2, TX or not examined were excluded. P-values were adjusted according to multiplicity adjusted p-values, derived from Benjamini and Hochberg(92). Significant correlating genes were re-matched to significant GSEA gene sets to display validated pathways related to ECM, PTM and cancer progression. Validated targets were further analyzed for prognostic overall (OS), and disease-free survival (DFS) identified by log rank statistics and Kaplan-Meier plots. In sum, only significant targets according to DEP, DEG, prognostic OS or DFS, and belonging to either EMT, ESC, PTM or neuronal pathways were further considered to perform uni- and multivariable Cox regression analysis. The underlying statistic was performed using SAS JMP version 13, KMplotter and graphs were designed by GraphPad Prism version 5.

Table 2: Clinical and pathological characteristics of MIBC TCGA cohort

<b>n=346</b>				<b>Median age</b>
				<b>69 years</b>
				<b>High grade tumors</b>
<i>Gender</i>	<b>m</b>	<b>f</b>		
	254	92		
<i>pT-stage</i>	<b>T2a/b</b>	<b>T3a/b</b>	<b>T4a/b</b>	
	105	186	55	
<i>pN-stage</i>	<b>pN0</b>	<b>pN1-3</b>		
	221	125		
<i>Disease-free status</i>	<b>No</b>	<b>Yes</b>	<b>N/A</b>	<b>Median disease-free month</b>
	156	115	75	15.9
<i>Overall survival status</i>	<b>Alive*</b>	<b>Deceased*</b>		<b>Median overall survival month</b>
	176	141		17.61

(n) number of subjects; (m) male; (f) female; (T2a/b) tumor invades (a) inner half or (b) outer half of muscularis propria bladder wall; (T3a/b) tumor invades perivesical tissue, (a) microscopically or (b) macroscopically; (T4a/b) tumor invades (a) prostate, uterus, vagina or (b) pelvic or abdominal wall; (pNX) regional lymph nodes cannot be evaluated histologically; (pN0) no regional lymph node metastasis; (pN1) metastases in a single lymph node, 2cm or less in greatest dimension; (pN2) Metastases in a single lymph node, more than 2 cm but not more than 5 cm in greatest dimension, or multiple lymph nodes, none more than 5 cm in greatest dimension; (pN3) Metastasis in a lymph node more than 5 cm in greatest dimension; (N/A) data not available.

\*Considering only patients with a follow-up of at least 3 month.

## 4 RESULTS

### 4.1 Identification of a uniform medium condition by pH and oxygen monitoring for BC cell lines

Based on *in vitro* systems, the choice of a suitable medium seems to be the most significant decision for proper cell growth. Besides nutrition's and growth factors, cell culture media needs to establish a continuous physiological pH environment, and environmental oxygen saturation for traditional *in vitro* systems. Therefore, three different cell culture media (RPMI + 5% FBS; Mc Coy's + 10% FBS; DMEM + 10% FBS) were uniformly investigated exemplified on five BC cell lines (UROtsa; RT4; UMUC-3; RT112/84; T24/83) in 2D culture. The consistency of physiological pH (7.4) and environmental oxygen (20%) were monitored over 4 days of culturing, and used as quality criteria to estimate a common medium for culturing BC cell lines under same conditions.

Initially, all media without cells show a different but consistent buffer capacity over 4 days as expected (RPMI + 5% FBS: pH=7.2; Mc Coy's + 10% FBS: pH=7.3, DMEM + 10% FBS: pH=7.6) (Figure 1; Figure 2). Overall, the pH is dropping over time considering the different cell lines under each condition (Figure 1; Figure 2). However, by comparing the pH consistency between the cell lines, variations under RPMI + 5% FBS condition are visibly the highest, ranging from pH=7.2-7.6 on day 0. Ranges from pH=7.2-7.4 and pH=7.4-7.6 are lower for Mc Coy's +10% FBS and DMEM + 10% FBS, respectively. Because of the higher pH inconsistency, the RPMI + 5% FBS condition was not further considered as uniform medium. The selection between the other two conditions was inconclusive. In case of Mc Coy's + 10% FBS, the pH range is closer to physiological conditions but the pH capacity is less stable over time. In contrast, DMEM + 10% FBS showed a more stable pH capacity over time but the pH is farer basic from the physiological condition. In terms of pH capacity, it can't be clearly distinguished between both remaining media. Also by considering the oxygen saturation, Mc Coy's + 10% FBS and DMEM + 10% FBS showed a stable concentration about 19-20% over time for every cell line, except for T24/83 (Figure 3). In case of T24/83, the oxygen level dropped after 2.5-3 days of growth. This effect was observed for all three conditions and seemed to be rather caused by a high cell count because T24/83 has the highest proliferation rate compared to the others (Fig1 (A, D, G)). Therefore, Mc Coy's + 10% FBS and DMEM + 10% FBS were selected to generate uniformly and comparable cell culture conditions for 3D establishment of BC cell lines.

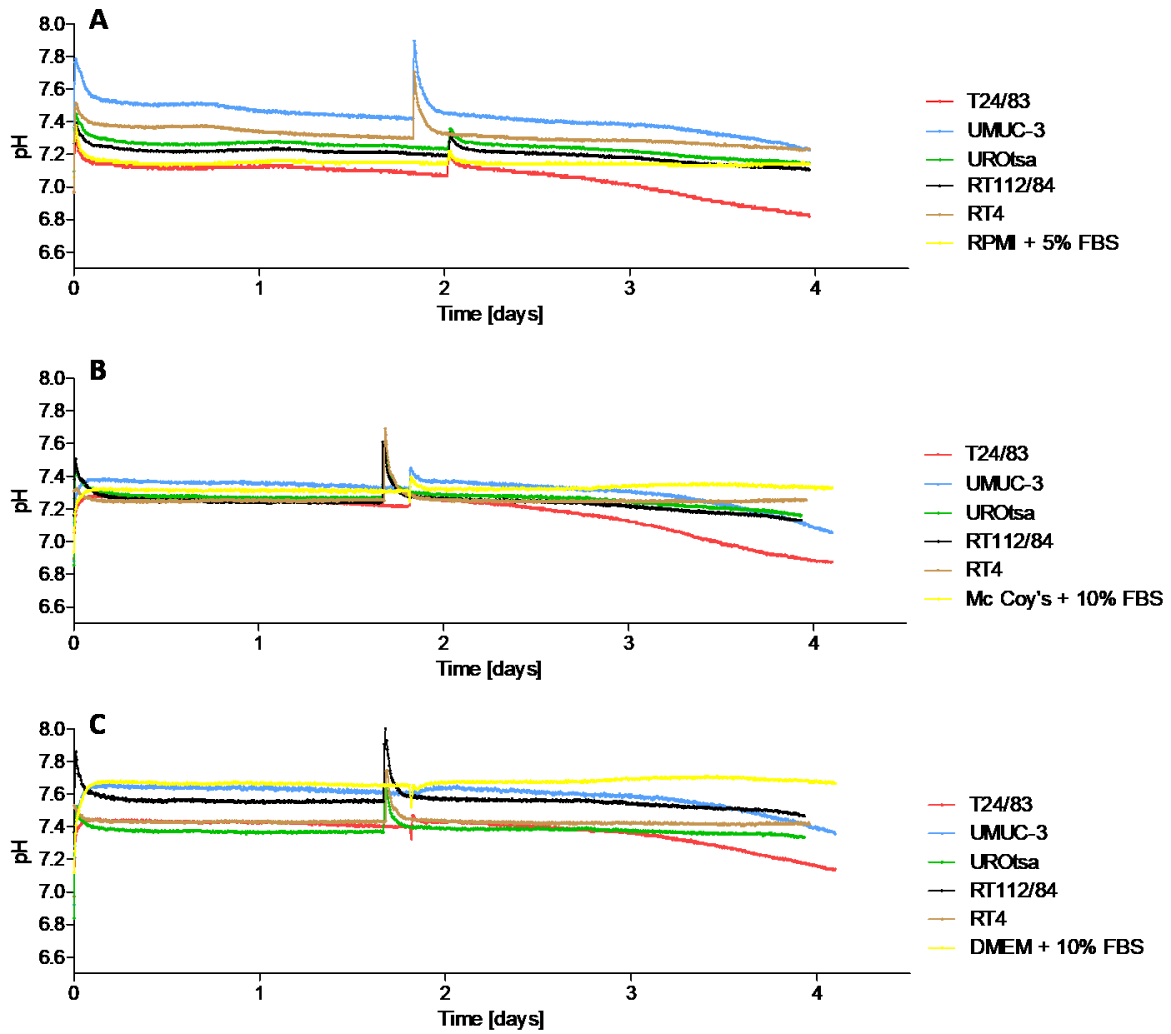


**Figure 1: pH online monitoring of 2D cultured BC cell lines**

The cell lines (UROtsa, RT4, T24/83, SCaBER) were cultured in 6-well OHD plates under RPMI, Mc Coy's or DMEM, and 10% FBS. The cultures were maintained for 4 days and medium was changed at 2<sup>nd</sup> day.

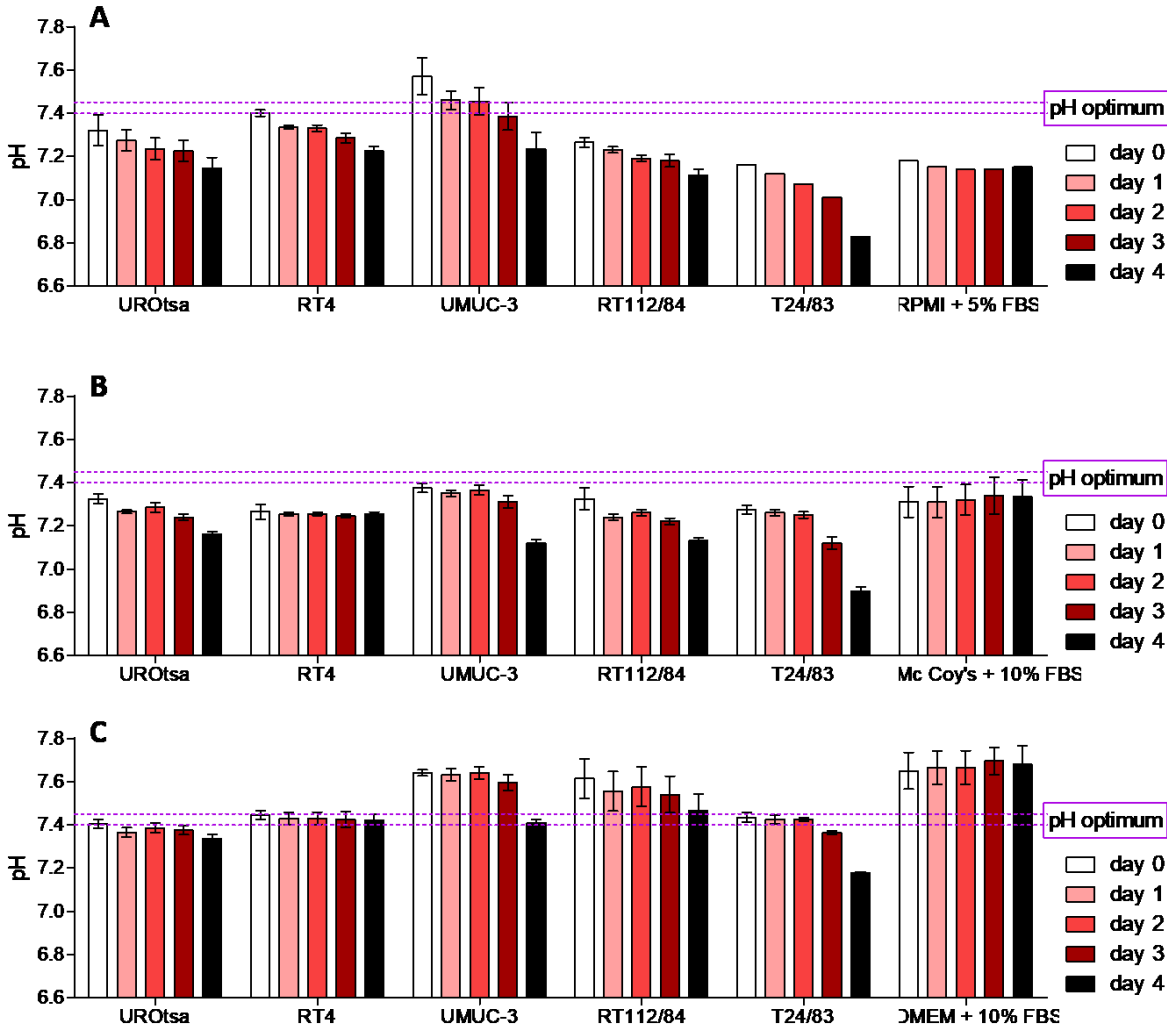


Figure 2: Bar chart of pH online monitoring of BC cell lines under consideration of pH optimum

The cell lines (UROtsa, RT4, T24/83, SCaBER) were cultured in 6-well OHD plates under RPMI, Mc Coy's or DMEM, and 10% FBS. The cultures were maintained for 4 days and medium was changed at 2<sup>nd</sup> day. The pH-change over time was evaluated taken into account physiological pH conditions that should be achieved.

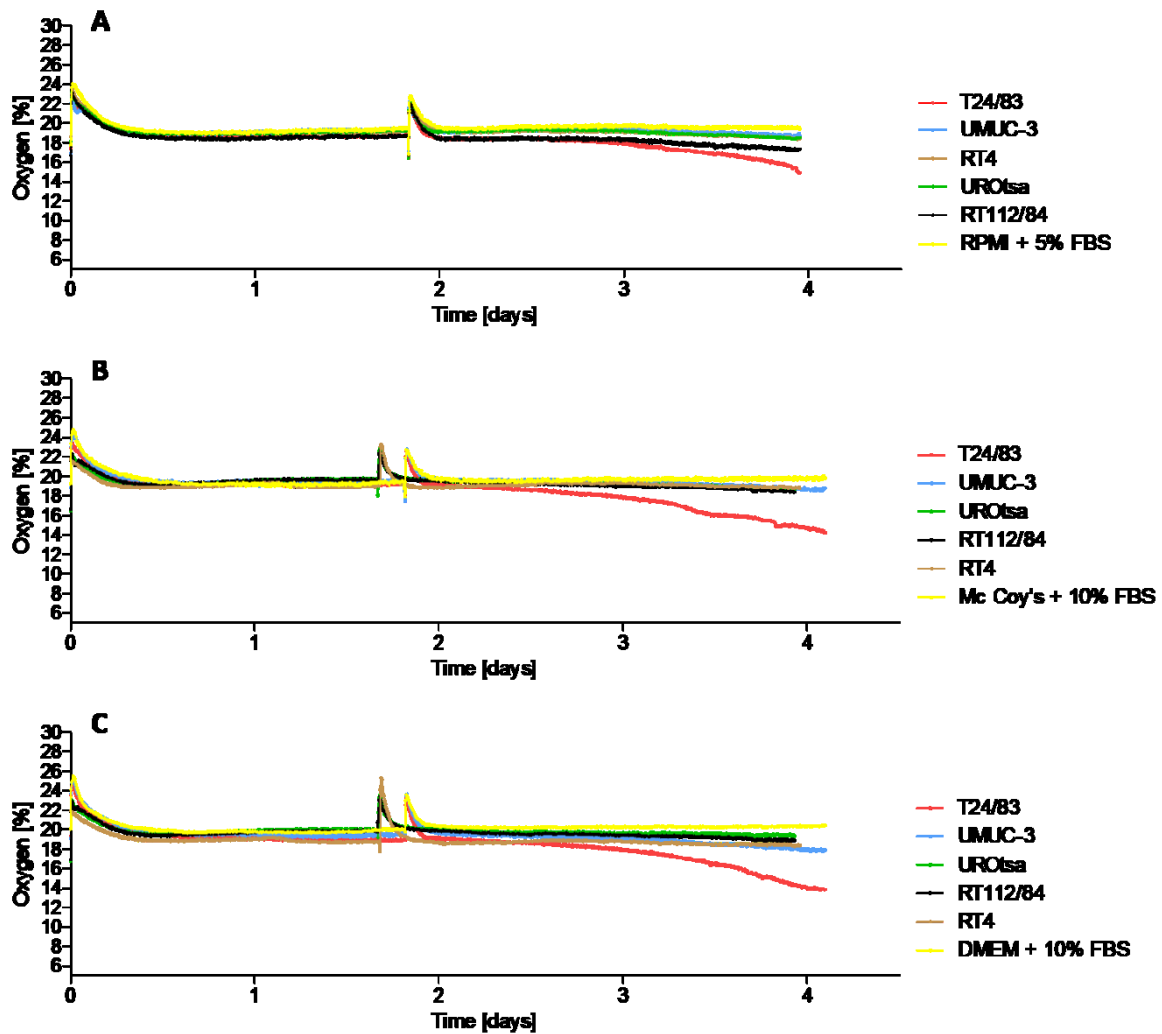


Figure 3: Oxygen concentration of 2D cultured BC cell lines

The cell lines (UROtsa, RT4, T24/83, SCaBER) were cultured in 6-well OHD plates under RPMI, Mc Coy's or DMEM, and 10% FBS. The cultures were maintained for 4 days and medium was changed at 2<sup>nd</sup> day. The oxygen concentration was calculated based on the pH online monitoring.

#### 4.2 BC cell line establishment of an 3D *in vitro* ultra-low-attachment system

Multiple different 3D orientated *in vitro* systems are applicable, but in terms of BC cell lines there is less use and establishment so far. By these reasons, it was aimed to develop intact growing spheroids by the ULA method with the BC cell lines UROtsa, RT4, T24/83 and SCaBER. For this approach, different cell counts were seeded, growth progress was daily observed by light microscopy and growth rates were calculated under different medium conditions. Finally, selected conditions and 3D-system validated cell lines integrity was examined by confocal microscopy.



#### 4.2.1 Evaluation of different medium conditions by spheroid growth rate

(Figure 4) For first, BC cell lines were cultured in 96-well ULA plates with the previous selected basal media DMEM + 10% FBS and Mc Coy's + 10% FBS. Under those conditions spheroids were not formed properly and degraded by time, except for RT4 (67). Hence, UROtsa, T24/83 and SCaBER showed a distinct negative growth rate.

To support the spheroidal cell arrangement, 50% of each basal media was substituted by CM derived from pnBF. In case of T24/83, supplementation with pnBF CM supported intact spheroid formation (Figure 18) and caused remarkable growth with 32.19  $\mu\text{m}/\text{day}$  and 25.79  $\mu\text{m}/\text{day}$  for Mc Coy's + 10% FBS and DMEM + 10% FBS, respectively. The CM addition to RT4 spheroids (Figure 17) resulted into growth rates of 18.00  $\mu\text{m}/\text{day}$  and 21.15  $\mu\text{m}/\text{day}$  for Mc Coy's + 10% FBS and DMEM + 10% FBS, respectively. For UROtsa and SCaBER the addition of CM displayed more stable spheroids over time (Figure 16; Figure 19), however without notable growth for supplemented DMEM + 10% FBS (UROtsa: 4.79  $\mu\text{m}/\text{day}$ ; SCaBER: 10.8  $\mu\text{m}/\text{day}$ ). For UROtsa, SCaBER and T24/83 the growth rates under supplemented Mc Coy's + 10% FBS were always higher compared to supplemented DMEM + 10% FBS, but for RT4 nearly the same. Finally, Mc Coy's + 10% FBS supplemented with CM was chosen for further experiments.

Spheroids were additionally cultured with Mc Coy's + 10% FBS supplemented with UCM in the same ratio as with CM. This condition was created to identify potential effects of the pnBF CM for further gene expression analysis. For T24/83 the UCM supplemented medium showed not remarkable difference in contrast to CM supplemented culture ( $\Delta=3.68 \mu\text{m}/\text{day}$ ). In case of RT4 the growth rate is noticeable increased for UCM supplemented medium (27.83  $\mu\text{m}/\text{day}$ ) compared to CM (18.00  $\mu\text{m}/\text{day}$ ). UROtsa (-0.51  $\mu\text{m}/\text{day}$ ) and ScaBER (5.51  $\mu\text{m}/\text{day}$ ) resulted into clearly reduced growth rates under UCM condition (Figure 4). In case of SCaBER cell line, it was observed that the spheroids were not floating within the well but were able to attach to the well bottom (Figure 19). By this effect, the spheroids could be hindered within their growth. Therefore, it was investigated whether free DNA fragments could be responsible for sticking the spheroids to the well bottom. For this experiment, the spheroids were cultured with CM supplemented medium and treated with DNase to counteract the potential effect of sticky DNA fragments. The results didn't show any detachment for SCaBER spheroids. In addition, the growth rate was also not increased compared to spheroids without DNase treatment. Even for UROtsa, RT4 and T24/83, DNase treatment didn't show higher growth rates (Figure 4).

Due to the low growth rates of UROtsa and SCaBER, cell lines were cultured in a hypoxic (3%) environment to examine whether the growth rates are changing to a higher direction when oxygen concentration is closer to physiological conditions. The data showed rather an opposite effect. Overall the growth rates were highly reduced under hypoxic conditions and even reached negative values in case of UROtsa and SCaBER for the UCM supplemented medium

(Figure 4). It is noticeable that SCaBER couldn't be analyzed under CM supplemented and hypoxic conditions thus the spheroids were losing their integrity and cells were able to attach to the bottom (Figure 19).

Concerning UROtsa and SCaBER, the growth rates were inconsistent and not remarkable over time. Even SCaBER is able to attach to the ULA wells. For these reasons, further experiments were conducted with RT4 and T24/83 only.

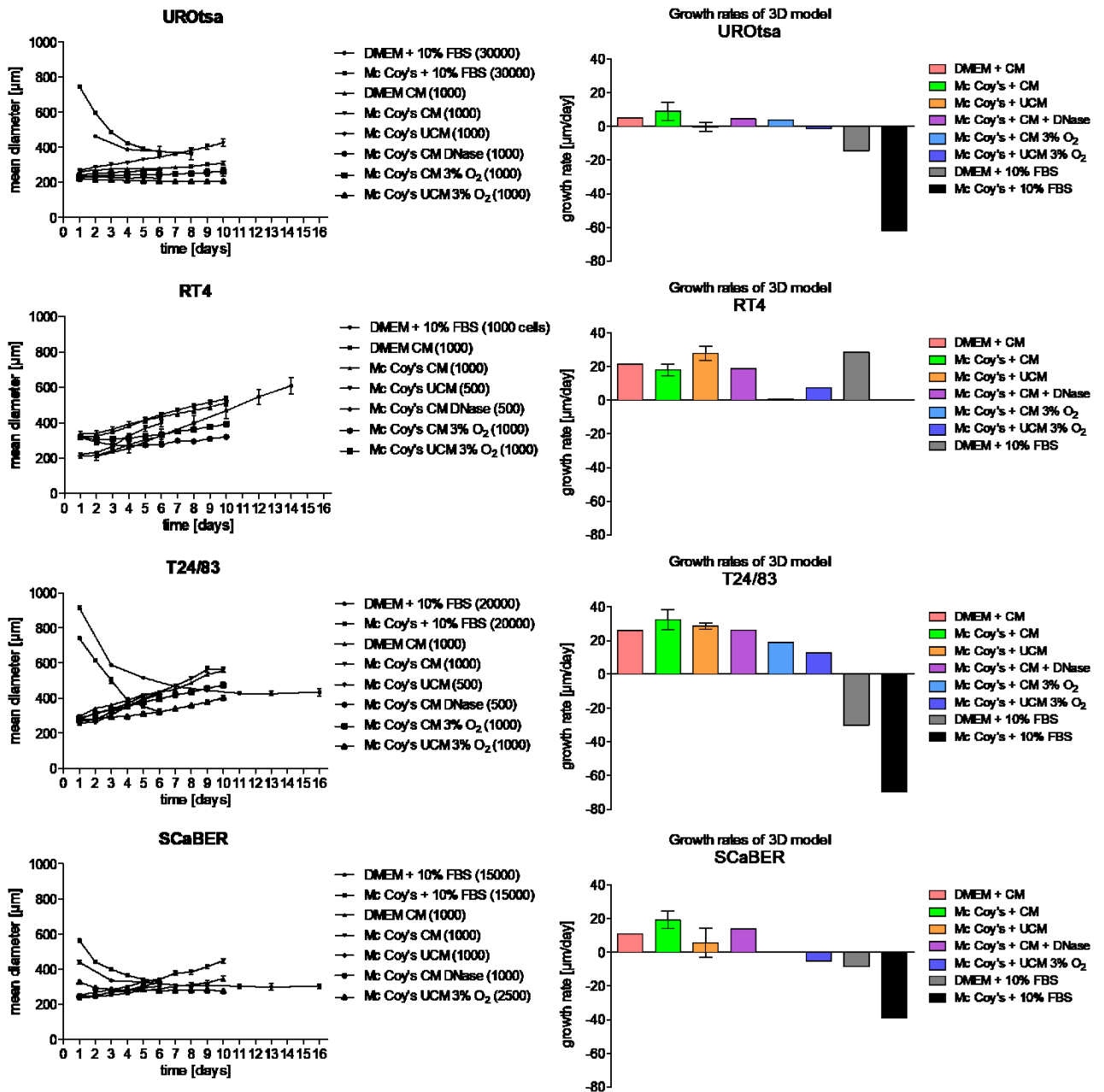


**Figure 4: Analysis of 3D cultured BC cell lines growth under different medium conditions**

The BC cell lines (UROtsa, RT4, T24/83, SCaBER) were seeded onto 96-well ULA plates under different medium conditions. Half of the medium was changed every 2<sup>nd</sup> day and light microscopic images were taken daily. From daily images, the spheroid diameter was analyzed by SpheroidSizer, a MATLAB plugin, and the mean diameter for each day was calculated from replicates. Growth rates were determined by µm growth per day.

#### 4.2.2 Identification of spheroid integrity by confocal imaging

RT4 and T24/83 under UCM and CM condition were further prepared by tissue clearing(80) and analyzed by confocal imaging to investigate spheroid integrity. Since light microscopy observation doesn't show cell arrangements insight of the spheroids, DAPI staining was performed. In addition, the distribution of proliferating and apoptotic cells were examined by Immunofluorescence using Ki67 and Cas3, respectively.

For both cell lines and conditions, DAPI staining represented the inner lying cells of the spheroids, while under CM conditions both cell lines appeared in a more compact arrangement, compared to UCM. Additionally, T24/83 under CM condition showed a round and smooth shape, while in UCM a grape-like structure was observed. Due to the looser arrangement of RT4 cells within UCM, the spheroids were represented a larger spheroid volume. The signals for Ki67 and Cas3 were normalized to the DAPI staining for each cell line and condition (Figure 5).

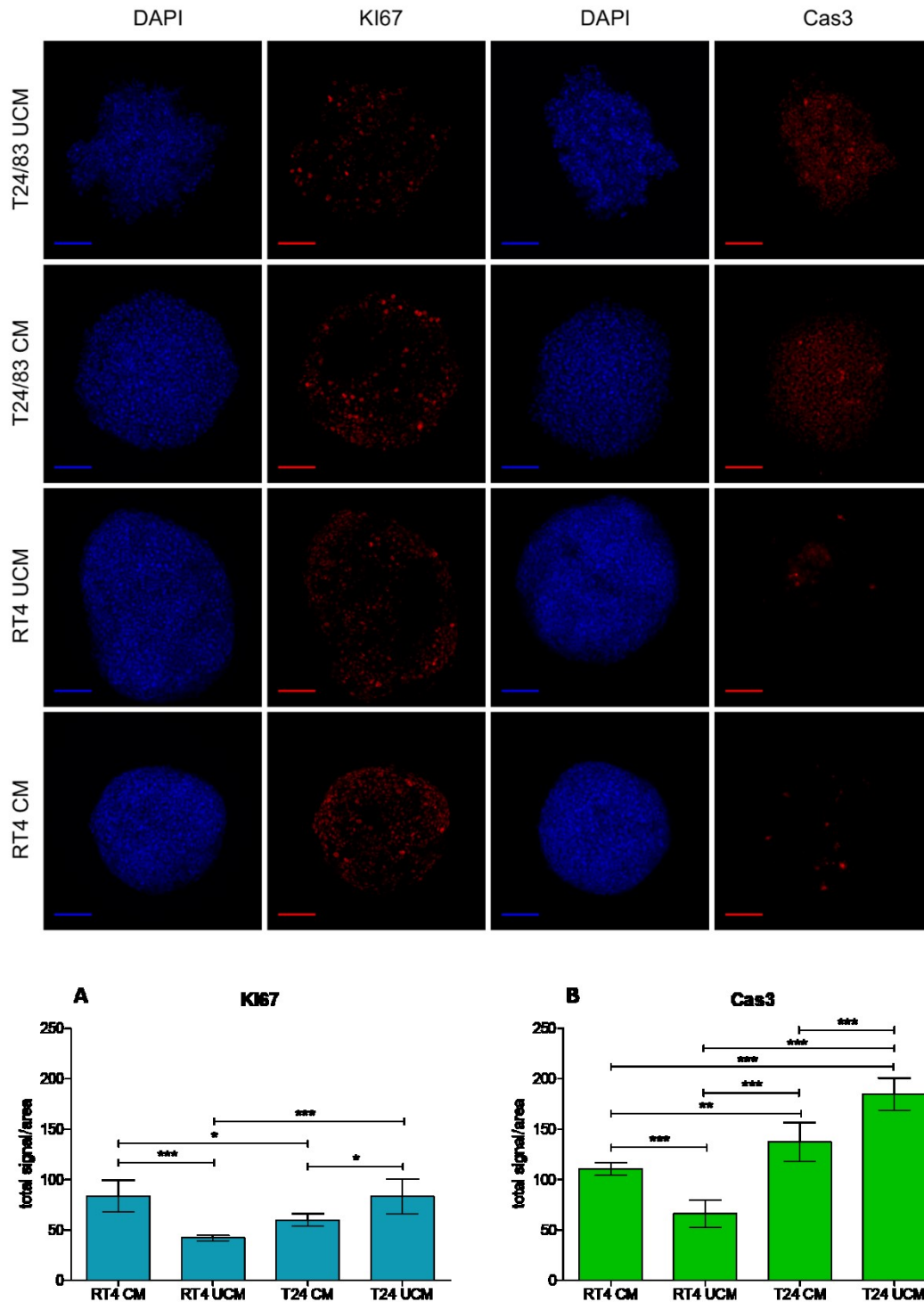


**Figure 5: Spheroid integrity of T24/83 and RT4 spheroids by confocal fluorescence imaging**

The ULA cultured T24/83 and RT4 spheroids were maintained in culture for 4 days under UCM (50% fibroblast basal medium+50% (Mc Coy's+10% FBS)) and CM (50% primary normal bladder fibroblast conditioned medium+50% (Mc Coy's+10% FBS)) condition. Further, they were treated by the Glycerol method for tissue clearing, and immune-stained with anti-Ki67 (A), anti-Cas3 (B), as well as with DAPI. Imaging was performed by SP8 confocal microscopy of 5 replicates to evaluate spheroid integrity by proliferation and apoptosis marker, as well as morphologically. Images were analyzed by sum projection of z-stacks of 160 $\mu$ m size, and a z-step size of 1 $\mu$ m. Fluorescence signals were normalized to the mean spheroid size of replicates and two-way ANOVA statistic was performed. Scale bar = 100 $\mu$ m.

T24/83 UCM showed a higher proliferation signal compared to the CM condition, which also holds for the apoptotic signal. This distribution was vice versa for RT4 UCM compared to CM condition, so that RT4 UCM proliferation and apoptotic signals were lower compared with the CM condition. In contrast to RT4 UCM, T24/83 UCM proliferation was significantly higher, while T24/83 CM is significantly lower compared to RT4 CM. Considering the general signal intensities, Cas3 demonstrated increased signals compared to Ki67. Comparing both cell lines, T24/83 UCM and CM conditions presented a higher amount of Cas3 presence in contrast to RT4 UCM and CM. The general amount of Ki67 signals were not significantly different within the different cell lines. This observation is seen by comparison of T24/83 CM with RT4 UCM, and T24/83 UCM with RT4 CM (Figure 5 A, B).

#### 4.2.3 Established 3D model and its final sample production

Out of four BC cell lines, T24/83 and RT4 have proven to be successful by culturing within the ULA 3D model under UCM and CM conditions. This composition of cell lines, media conditions and *in vitro* model was further used to generate samples for proteomics and transcriptomics application. As depicted in Figure 6, the spheroids were cultured for eight days and represented consistency in growth and shape as during establishment.

Further samples of 2D cultured T24/83 and RT4 cells were cultured under Mc Coy's + 10% FBS, UCM and CM condition (Figure 7). Under standard medium conditions the RT4 cells grow in characteristic multi-layered colonies, while T24/83 cells showed a classic monolayer growth pattern in 2D. The use of the UCM or CM medium conditions changed the morphology of RT4 noticeable. In comparison to Mc Coy's + 10% FBS, the RT4 cells still grow in a tight arrangement but not in colonies, thus they are more distributed over the growth area in a planar manner. For T24/83, no morphological change was observed under the different medium conditions in 2D culture.

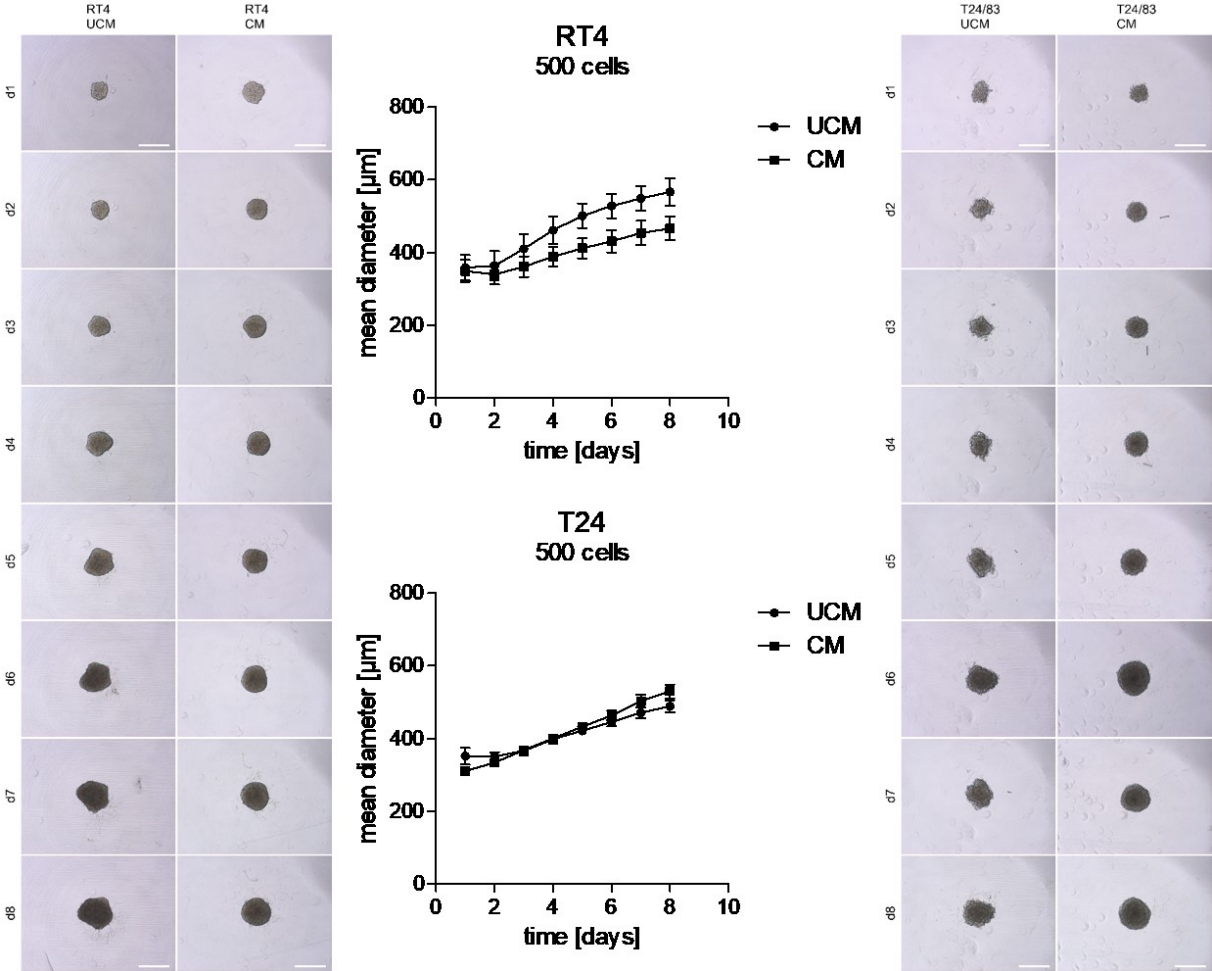


**Figure 6: Growth and formation of T24/83 and RT4 cultured spheroids for omics analysis**

Each 500 cells of T24/83 and RT4 BC cell lines were seeded into 3D ULA format, and cultured for 8 days under UCM (50% fibroblast basal medium+50% (Mc Coy's+10% FBS)) and CM (50% primary normal bladder fibroblast conditioned medium+50% (Mc Coy's+10% FBS)) condition for their use in further gene expression omics applications. Half of the Medium was changed every 2<sup>nd</sup> day, and the spheroid growth was analyzed by light microscopy imaging and MATLAB (SpheroidSizer) analysis. Daily imaging of 46 different spheroids and for 3 different passages was conducted. Scale bar = 500 $\mu\text{m}$ , magnification = 5x.

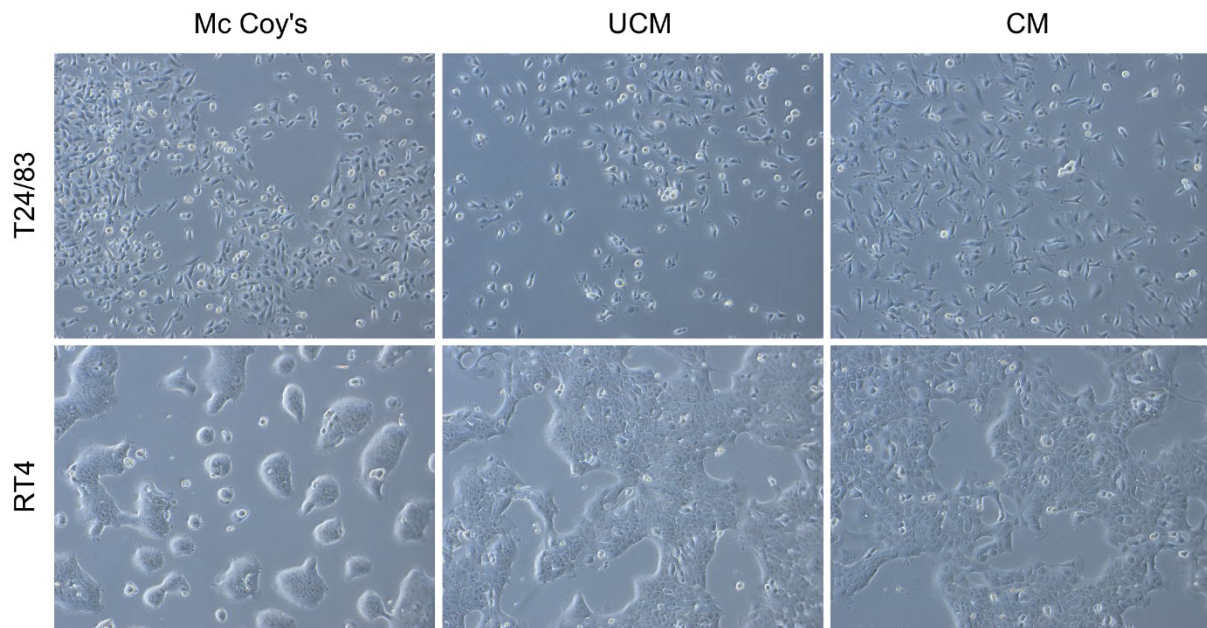


**Figure 7: Growth and formation of T24/83 and RT4 2D culture for omics analysis**

T24/83 and RT4 BC cell lines were maintained in 2D culture for 3 days under standard (Mc Coy's+10% FBS), UCM (50% fibroblast basal medium+50% (Mc Coy's+10% FBS)) and CM (50% primary normal bladder fibroblast conditioned medium+50% (Mc Coy's+10% FBS)) condition for their use in further gene expression omics applications. Medium was changed every 2<sup>nd</sup> day, light microscopically images were taken daily for 3 different passages totally. Magnification = 10x.

### 4.3 Multi-omics analysis of BC cell line spheroids

#### 4.3.1 Global perspective of differential expressed proteins and genes

The molecular analysis of the established RT4 and T24/83 spheroids, and the respective 2D samples, was primarily conducted by LC-MS application. The data evaluation was performed based on the functional protein level, and validated by RNA microarray as well as by mRNA expression of *in silico* clinical data of MIBC patients.

For RT4 and T24/83, the 2D model was cultured under standard condition (Mc Coy's + 10% FBS), UCM and CM, and the 3D model under UCM and CM. The average amount of proteins per sample/replicate was in between 4000-5000 proteins, with 5483 different proteins detected in the entire measured samples (Figure 8, A). Further proteomic characterization was achieved by two-dimensional t-SNE (t-distributed stochastic neighbor embedding) plots. This visualization outlines similarities and differences of expressed proteins between the samples, depending on proximity. Each point represents one replicate of one cell line under one condition. By consideration of the factors cell line, *in vitro* model and medium condition, a distinct separation between RT4 and T24/83, as well as between the 2D and 3D model was identified (Figure 8, B, C). However, the different medium conditions appeared in much closer



proximity to each other, and were less distinguishable from each other within a certain cell line and *in vitro* model (Figure 8, D).

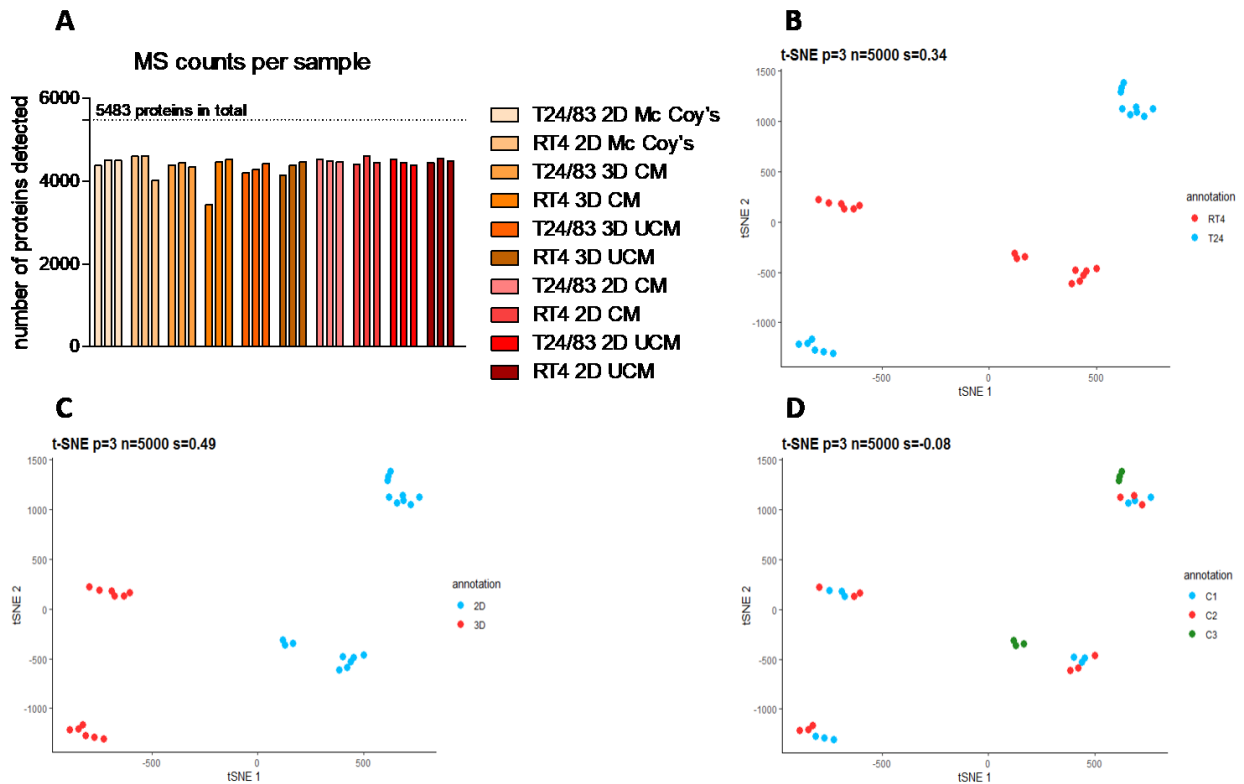


**Figure 8: Proteomics outcome and annotation to, cell line, *in vitro* model and medium condition**

2D and 3D cultured T24/83 and RT4 under different medium conditions were analyzed by LC-MS. In total, 5483 different proteins were detected along all samples after median normalization and filtered for a false discovery rate of 1% (A). The proteins were further annotated and displayed by t-SNE plots to outline similarities and differences of expressed proteins between the samples, depending on proximity. T24/83 and RT4 (B); 2D and 3D model (C); medium conditions (D). C1 (UCM); C2 (CM); C3 (Mc Coy's+10% FBS).

In order to specify the observed discrepancies, DEP were analyzed for each kind of sample and cell line, in comparison to the respective 2D standard condition (Figure 9).

In case of T24/83, it is clearly displayed that the count of significantly DEP was higher in the 3D UCM and CM condition compared to the standard ones, with 494 and 461, respectively. In contrast, the count of significantly DEP within the different media conditions was clearly lower with 20 DEP for 2D UCM and 8 DEP for 2D CM, compared to 2D standard condition (Figure 10, A). By highlighting the relation between up- and downregulated DEP, the 3D model showed about 50% proportion of up- and downregulated significantly DEP (Figure 10, a). A similar trend is represented by the RNA microarray data, indicated by significant DEG. Hence, the 3D model presented under UCM and CM condition 2978 and 3219 significantly DEG, respectively. As on protein level, the media comparisons showed a less count of significantly DEG with 980 for 2D UCM 825 for CM, compared to 2D standard condition (Figure 10, B). However, the proportion of up- and downregulated DEG is not as distinct separable as on protein level. In



this case the proportions were distributed over 50%-60% of significantly up- or downregulated DEG (Figure 10, b).

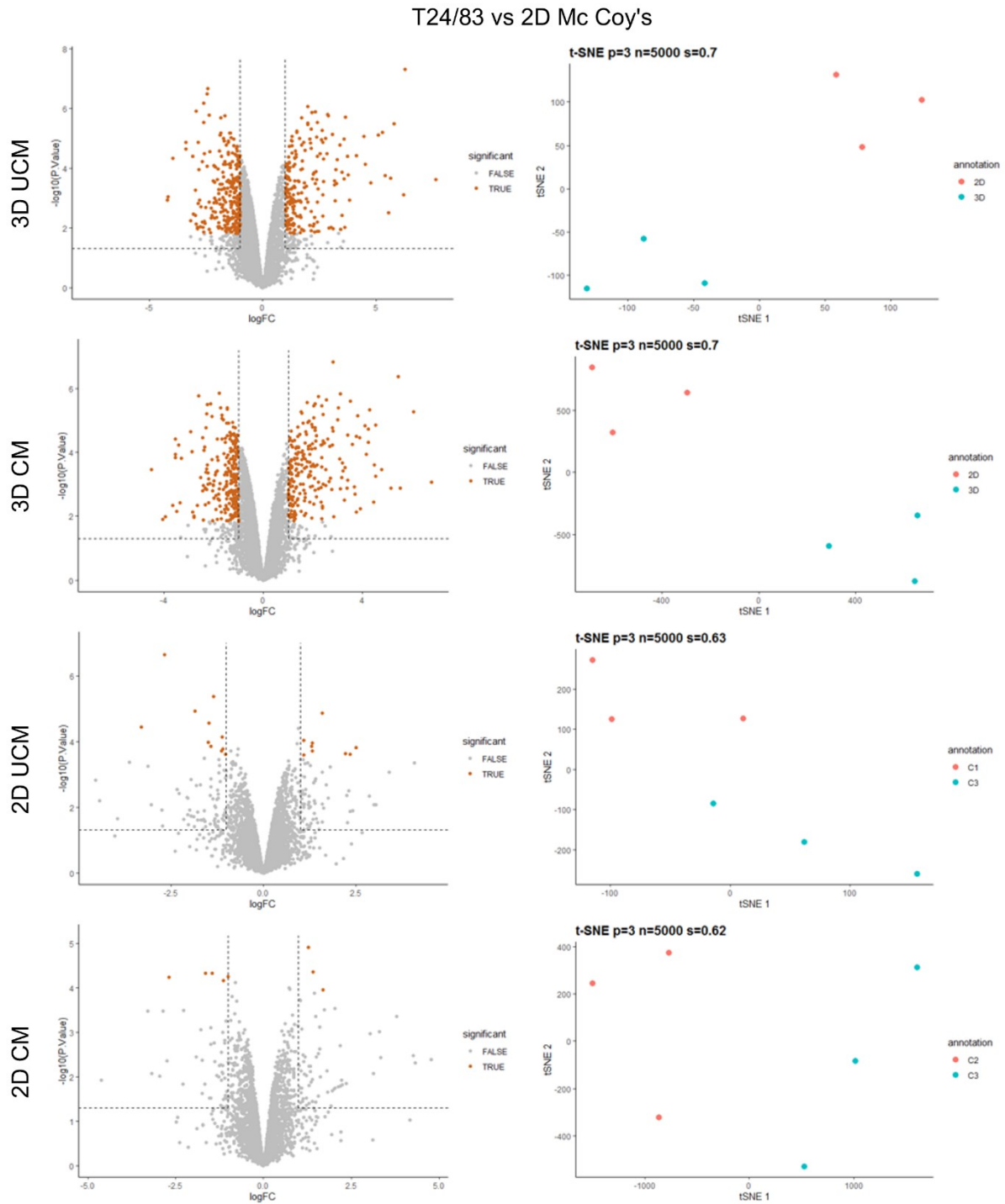


**Figure 9: Volcano plot and related t-SNE annotation of DEP for T24/83**

DEP for T24/83 were analyzed by limma statistics and displayed by volcano and t-SNE plot. The comparison of the 3D model (UCM and CM), and 2D model (UCM and CM), in contrast to the 2D standard condition (Mc Coy's+10% FBS) was conducted. A brown data point of the volcano plot represents one significantly DEP within the particular comparison. C1 (2D UCM); C2 (2D CM); C3 (2D Mc Coy's+10% FBS); 2D (2D Mc Coy's+10% FBS).

With respect to RT4, significantly DEP can also be grouped into a higher count and lower count category, as for T24/83 (Figure 20, Figure 21, A;). The conditions 3D UCM with 149 and 2D

CM with 128 significantly DEP represented the higher count conditions. While, 3D CM and 2D UCM with 26 and 72, respectively, the lower count conditions of significantly DEP. The proportion of significantly downregulated DEP was similar for almost all conditions with around 60%. However, only about 25% of significantly DEP were downregulated for 2D UCM (Figure 21, a). On the contrary, the significantly DEG showed a completely different distribution, and no similarities to the distribution of the significantly DEP (Figure 21, B). In this case, a higher count for 3D UCM with 3262 and 3D CM with 3322 was observed. For the 2D UCM and 2D CM condition, 2697 and 2625 were demonstrated, respectively. The proportion of significantly up- or downregulated DEG is around 50% for each condition (Figure 21, b).

Independent of the conditions, the total count of significantly DEP was 983 for T24/83 and 375 for RT4. By this finding, the total count of the resulting significant GSEA gene sets was higher for T24/83 with 180, and lower for RT4 with 98. In contrast, the total count for significantly DEG was 8002 for T24/83 and 11906 for RT4, in comparison to the 2D standard conditions.

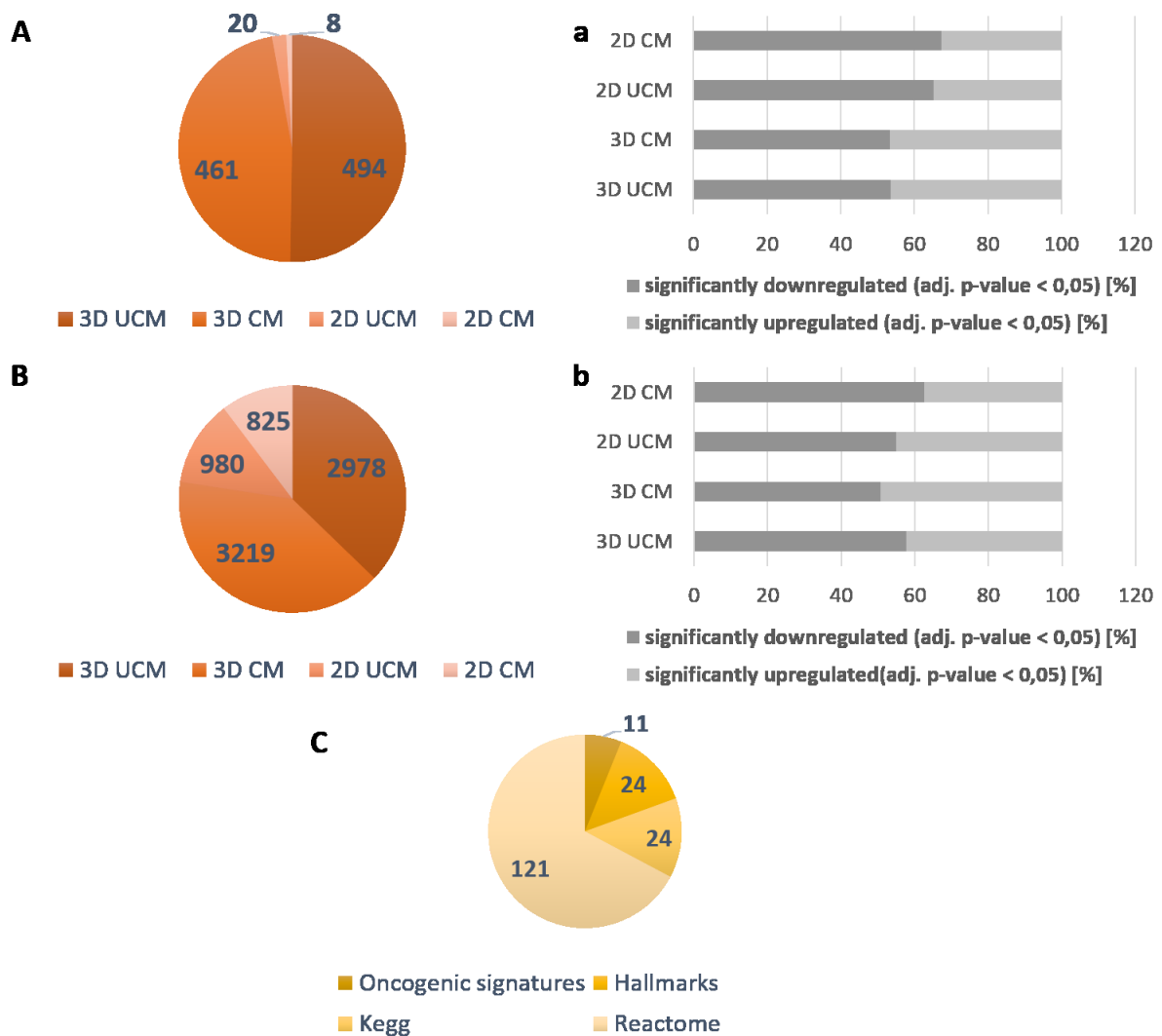


**Figure 10: Counts of significantly DEP and DEG in T24/83 in relation to the 2D standard condition**

Significantly DEP (A) and DEG (B) for T24/83 were analyzed by limma statistics and one-way ANOVA, respectively. The comparison of the 3D model (UCM and CM), and 2D model (UCM and CM), in contrast to the 2D standard condition (Mc Coy's+10% FBS) was conducted. Further, the proportion of up- and downregulated, significantly DEP (a) and DEG (b) is shown. The GSEA analysis was performed by the use of Kegg, Reactome, Hallmark, and oncogenic signatures gene sets, and the amount of significantly differential regulated pathways is given for each gene set database, detected for T24/83 (C).

#### 4.3.2 Evaluation of proteomic-based gene set enrichment analysis

Additionally, to point out biological features, a GSEA with the examined DEP was conducted for each cell line of different *in vitro* models and media conditions. At first, typical characteristics for 3D cell models, compared to 2D standard condition were determined, by considering significantly altered expressed gene sets. Factors like, posttranslational protein modifications, hypoxia, ECM, cell cycle and DNA replication, as well as apoptosis were previously described, and can be remarkably altered in context of 3D *in vitro* models, compared to 2D models(63).

For the T24/83 3D model, the percentage of posttranslational protein modifications, hypoxia and ECM significantly altered gene sets were up-regulated compared to the standard 2D condition, with around 80%-90%. In contrast, almost 100% of the gene sets related to cell cycle and DNA replication were downregulated. In case of apoptotic gene sets, about 70% showed an up-regulation for the 3D CM model, while 30% of these gene sets were up- and downregulated in the 3D UCM model. With respect to the 2D CM condition, about 20% of the ECM gene sets displayed up- and 10% of the cell cycle and DNA replication gene sets were downregulated. The 2D UCM model showed that 20% of the significantly gene sets for posttranslational protein modification and ECM were downregulated. No altered gene sets for hypoxia or apoptosis were determined for 2D CM and UCM condition (Figure 11).

In case of RT4, the 3D UCM and CM conditions represented an upregulation for 100% of the significant gene sets for hypoxia, and 60%-70% for cell cycle and DNA replication, compared to the 2D standard condition. Additionally, 3D UCM presented about 40% upregulated posttranslational protein modification- related gene sets, and 20% of ECM-related ones. On consideration of the 2D CM condition, a downregulation of significantly differential expressed gene sets was observed for about 20% of posttranslational protein modification, 100% of hypoxia, 15% of cell cycle and DNA replication, and 30% of apoptosis-related gene sets. At the same time, about 40% of the significantly differential expressed gene sets for cell cycle and DNA replication were upregulated. Furthermore, the 2D UCM condition showed about 10% of significantly expressed gene sets for cell cycle and DNA replication, and 35% for apoptosis were downregulated. No change of significantly differential expressed gene sets was observed for 3D CM, concerning posttranslational protein modification, ECM and apoptosis, as well as for 3D UCM with respect to apoptosis, 2D UCM with regard to posttranslational protein modification, hypoxia and ECM, and finally for 2D CM in relation to ECM (Figure 22).

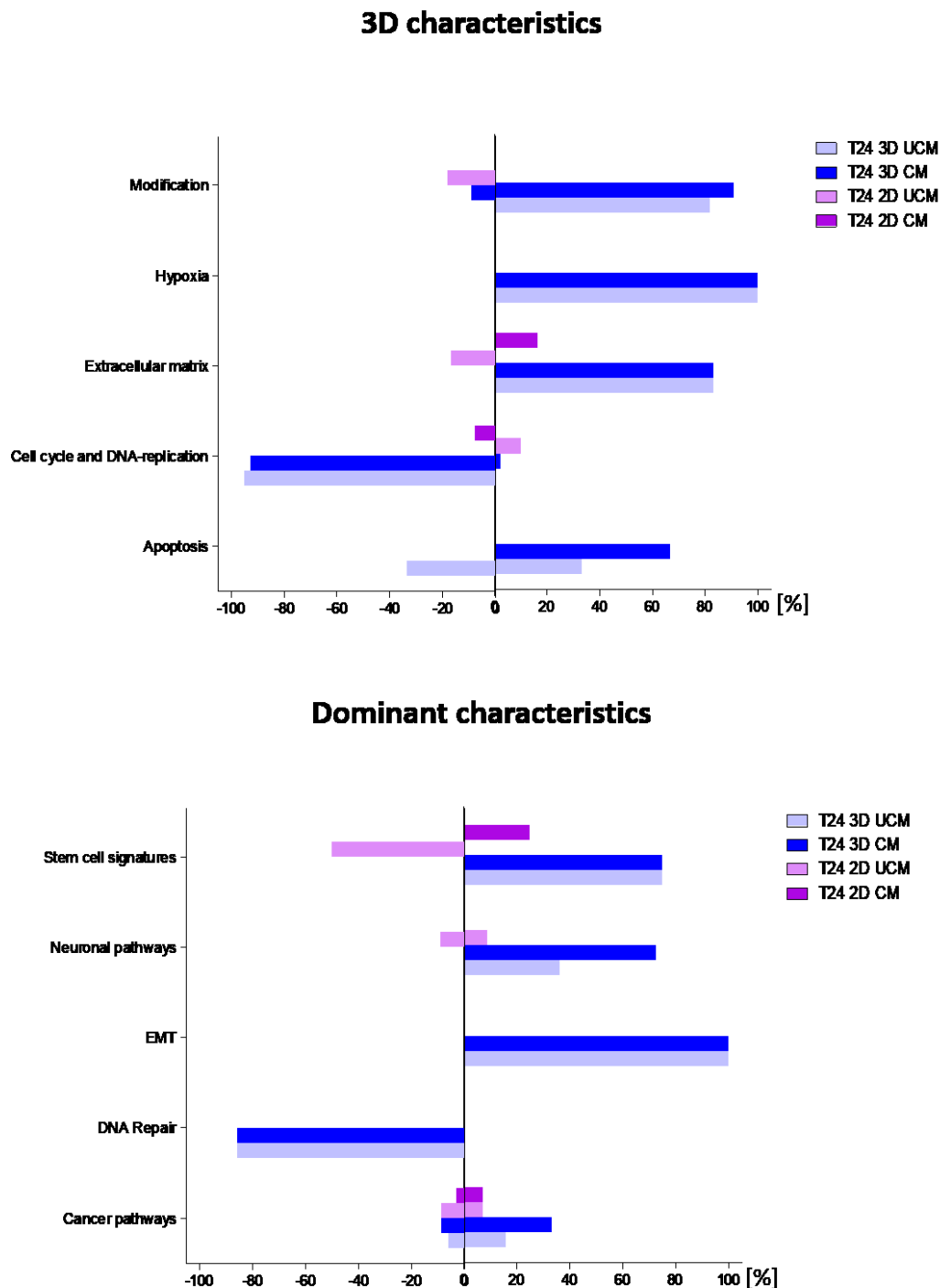


**Figure 11: GSEA outcome of biological functions for T24/83 in relation to 2D standard condition**

Significantly, differential expressed gene sets have been grouped according to their biological function. Typical 3D characteristics (upper chart) and further dominant characteristics (lower chart) revealed for T24/83. Each biological function plotted on the y-axis consists of functional related gene sets, which are shown as percentage depending if the gene set is significantly over- or under-representation.

Based on the invasive cell line T24/83, conspicuous characteristics, resulted by the GSEA, are showed in Figure 11. Gene sets from biological features as stem cell signature, neuronal pathways, EMT, DNA repair and cancer pathways represented noticeable alterations for T24/83, compared to 2D standard condition. The 3D UCM and CM condition pointed equally

elevated expression of significant gene sets for stem cell signature and EMT with 80% and 100%, respectively. In terms of neuronal pathways, also upregulated were observed with more gene sets being upregulated for 3D CM (70%) as for 3D UCM (40%). Furthermore, significant altered gene sets for DNA repair were downregulated by 80% for 3D UCM and CM condition. Most of the significant differential expressed cancer pathways were upregulated in the 3D model, with around 40% for 3D CM, and 20% for 3D UCM, while about 10% for CM and 5% for UCM were downregulated. Concerning the different media conditions within the 2D models, significant altered gene sets, representing stem cell signatures, were upregulated about 20% for 2D CM, and 50% downregulated for 2D UCM, compared to 2D standard condition. Further, 10% of neuronal pathway gene sets are up- and downregulated for 2D UCM, but no alteration was observed for 2D CM. For 2D UCM, about 5% of cancer pathway gene sets were up- and downregulated compared to 2D standard condition, while 2D CM showed around 5% up- and 2.5% downregulated significant differential expressed gene sets. In case of EMT and DNA repair, no alterations were detected for the 2D CM or UCM model (Figure 11).

In contrast to the non-invasive cell line RT4, both 3D conditions demonstrated equally up-regulated significantly differential expressed gene sets for EMT, like T24/83, as well as for DNA repair with 100% downregulated gene sets for 3D UCM and 90% for 3D CM. Cancer pathways represented an 10% up-regulation for 3D CM and 3D UCM of the significantly expressed gene sets, while about 5% were downregulated in both conditions. In addition, about 10% of significantly differential expressed neuronal pathways were observed to be downregulated for the 3D CM condition, compared to the 2D standard model. In terms of the different media conditions, 2D CM and 2D UCM showed contrary regulations generally. In relation to differential expressed gene sets from neuronal pathways, EMT and cancer pathways, 2D CM demonstrated a downregulation with about 20%, 100% and 20%, respectively, while 2D UCM showed an up-regulation with approximately 30%, 100% and 30%, respectively. In case of differential expressed gene sets for DNA repair, 100% were up-regulated for 2D CM, and for 2D UCM around 30% downregulated. Overall, no alteration of aberrantly regulated significant gene sets were observed for stem cell signatures, and additionally for 3D UCM regarding neuronal pathways (Figure 22).

#### 4.3.3 ECM-based targets selection and *in silico* validation in clinical samples

The identification of ECM targets and related mechanisms was further conducted by the selection of significantly differential expressed ECM-related gene sets, in contrast to 2D standard condition, from proteomics-based GSEA. Overall measured samples, six different ECM gene sets were detected as significant (Table 3). 5(6) ECM-related gene sets, as ECM-receptor interaction, collagen formation, ECM organization, focal adhesion, and integrin cell surface interactions, were determined as upregulated for T24/83 UCM and CM condition,

according to the normalized enrichment score. In comparison, T24/83 2D UCM and CM only showed a significant relation to ECM-receptor interaction, while upregulated for 2D CM, and downregulated for 2D UCM.

For RT4 3D UCM, the ECM-related gene set, cell adhesion molecules-CAMs, represented a significantly upregulated one, while for RT4 3D CM, 2D UCM, and 2D CM, no ECM-related gene set was detected as significantly altered compared to the 2D standard condition (Table 3).

**Table 3: ECM-related significantly differential expressed gene sets after GSEA**

Condition	ECM gene sets (n=6)	NES
<b>T24/83 2D UCM</b>	ECM-RECEPTOR-INTERACTION	-1,874159108
<b>T24/83 2D CM</b>	ECM-RECEPTOR-INTERACTION	1,872160204
<b>T24/83 3D UCM</b>	COLLAGEN-FORMATION	2,568001931
	ECM-RECEPTOR-INTERACTION	2,591280627
	EXTRACELLULAR-MATRIX-ORGANIZATION	2,614846747
	FOCAL-ADHESION	1,718918532
	INTEGRIN-CELL-SURFACE-INTERACTIONS	2,237117686
	COLLAGEN-FORMATION	2,504477256
<b>T24/83 3D CM</b>	ECM-RECEPTOR-INTERACTION	2,580873277
	EXTRACELLULAR-MATRIX-ORGANIZATION	2,56534045
	FOCAL-ADHESION	1,909341182
	INTEGRIN-CELL-SURFACE-INTERACTIONS	2,454926531
<b>RT4 3D UCM</b>	CELL-ADHESION-MOLECULES-CAMS	1,848079099

NES = normalized enrichment score, if (+) = gene set is higher expressed, if (-) = gene set is lower expressed compared to the 2D standard condition.

Further on, all detected ECM-related proteins (n=35) were extracted from the DEP data, and matched against the significantly differential expressed gene sets, identified by GSEA. Besides the six ECM-related gene sets, eighty-four (n=84) further gene sets appeared, and indicate the involvement of the thirty-five detected ECM proteins. Under consideration of detected proteins, derived from ECM, EMT, ESC, neuronal pathways, cancer pathways, and PTM gene sets, n= 1053 potential protein targets resulted, and were used for *in silico* validation in MIBC patients mRNA expression derived from the TCGA cohort (Figure 12, A). Although the PTM significantly

differential expressed gene sets did not appear within the 84 gene sets, glycosylations are important and highly common structures of the ECM, so they were considered as well. In case of the cancer pathways, all significant differential expressed gene sets were used, independent whether they appeared after matching or not, and if applicable assigned to related cancer pathways.

All selected targets were correlated to clinicopathological parameters, in terms of age, gender, lymph node metastases (pN0-3), TNM staging (T2-T4), survival status (alive, deceased), and recurrence status (recurred, not recurred). As a result, n=304 different targets showed significant correlations to clinicopathological parameters, after adjustment of p-values. Out of those 304 targets, 42 demonstrated a significant relation to OS, and 24 to DFS (Figure 12, B).

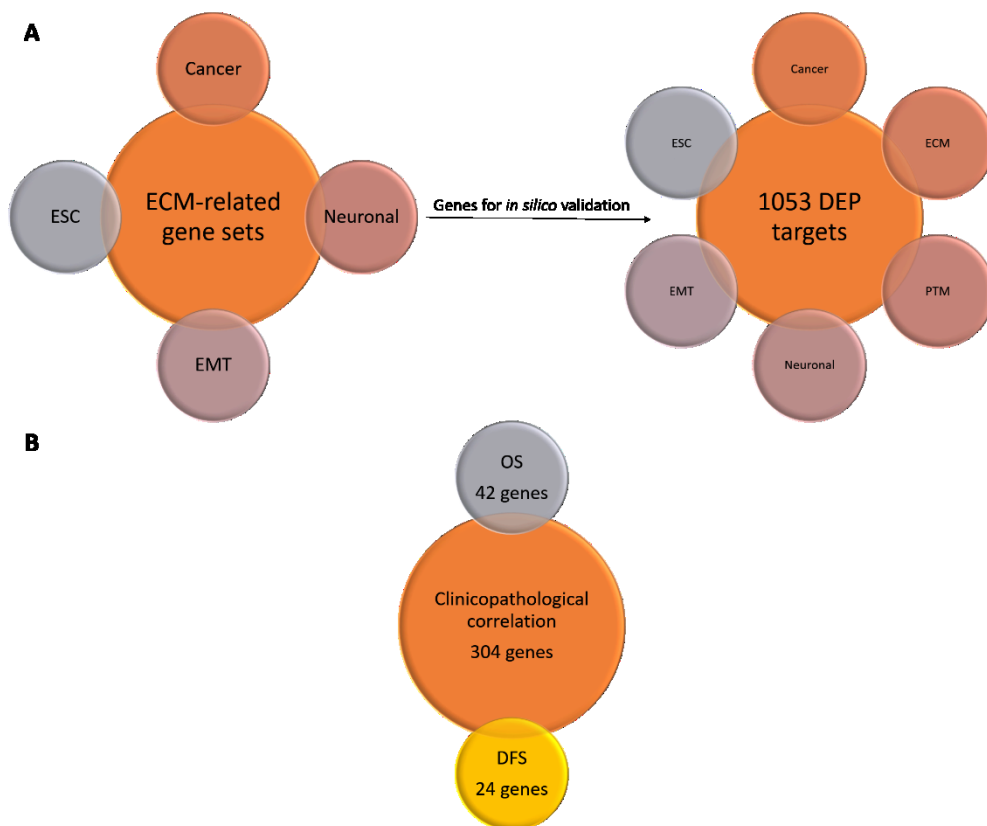


**Figure 12: Process of protein target selection by *in silico* validation of MIBC patient mRNA data**

DEP detected within ECM-based and –related gene sets (1053 proteins) were *in silico* validated by correlation analysis to clinicopathological parameters (age, gender, lymph node metastases (pN0-3), TNM staging (T2-T4), survival status (alive, deceased), and recurrence status (recurred, not recurred)) in MIBC patients. Furthermore, p-value adjustment resulted into 304 significantly correlating targets. These were further analyzed by KM-plotter online tool for their prognostic significance with regard to OS and DFS. 42 and 24 targets showed a significant relation to increased mRNA expression with OS and DFS, respectively.

As criteria for further target consideration, they needed to be significantly correlated to at least one clinicopathological parameter after p-value adjustment, at least significantly related to OS or DFS, and significantly differential expressed for the *in vitro* applications on protein and mRNA level. Finally, 12(1053) were determined by this approach (Table 4).



Overall, the targets were either validated in the 3D CM or 3D UCM condition of T24/83, while for RT4 no ECM-related target was valid. All of them showed increased levels for protein and mRNA *in vitro*, compared to the 2D standard condition. Most of the targets were defined as valid for the 3D CM condition, with 8(12) (CALU, CD109, EGFR, FBN1, HTRA1, ITGB3, LAMC1, LRP1), while only 2(12) targets belonged to the 3D UCM condition (DPYSL3 and SUMF2). Equally, 2(12) targets were valid for both conditions (P4HA2 and PLOD1). In addition, levels of the TCGA mRNA expression data were always elevated in correlation with advanced cancer features and poor prognosis for OS and/or DFS (Figure 13, Figure 14). For the targets CALU, DPYSL3, FBN1, HTRA1, and LRP1, higher mRNA levels were significantly determined for patients with MIBC, diagnosed with lymph node metastasis, higher T-stage (T3/T4), as well as those who recurred from the disease or died. The other 7(12) targets (CD109, EGFR, ITGB3, LAMC1, P4HA2, PLOD1, SUMF2) showed either increased levels in correlation to higher T-stage (T3/T4), to patients recurred from the disease, died, or a combination of those factors, however they did not correlate with the presence of lymph node metastasis.

Table 4: Significantly DEP and DEG correlations to TCGA MIBC mRNA expression

Gene/protein	MS*	MA*	<i>In vitro</i> condition	GSEA gene sets	Clinicopathological correlation	p-values	OS*	DFS*
CALU	2.59E-02	6.35E-03	3DCM T24/83 ▲▲	EMT	pN+ ▲ T3/T4 vs T2 ▲ Died ▲ Recurred ▲	<u>1.20E-03</u> <u>2.14E-03</u> <u>5.63E-05</u> <u>3.12E-03</u>	1.30E-04	nv
CD109	1.21E-03	6.09E-07	3DCM T24/83 ▲▲	N	T3/T4 vs T2 ▲ Died ▲ Recurred ▲	<u>9.39E-03</u> <u>3.86E-03</u> <u>9.14E-03</u>	2.60E-04	nv
DPYSL3	5.97E-03	1.86E-03	3DUCM T24/83 ▲▲	EMT, N	pN+ ▲ T3/T4 vs T2 ▲ Died ▲ Recurred ▲	<u>1.23E-02</u> <u>2.01E-04</u> <u>2.00E-03</u> <u>5.81E-03</u>	nv	3.60E-04
EGFR	3.36E-02	2.99E-04	3DCM T24/83 ▲▲	N, C	Died ▲ Recurred ▲	<u>6.90E-03</u> <u>1.76E-02</u>	3.30E-05	2.20E-04
FBN1	1.14E-02	3.64E-10	3DCM T24/83 ▲▲	EMT	pN+ ▲ T3/T4 vs T2 ▲ Died ▲ Recurred ▲	<u>7.79E-03</u> <u>4.66E-06</u> <u>9.00E-04</u> <u>8.47E-03</u>	3.10E-05	nv
HTRA1	2.07E-02	2.42E-13	3DCM T24/83 ▲▲	EMT, ESC	pN+ ▲ T3/T4 vs T2 ▲ Died ▲ Recurred ▲	<u>4.06E-02</u> <u>2.90E-03</u> <u>1.73E-03</u> <u>4.79E-02</u>	8.80E-08	nv
ITGB3	1.15E-03	1.20E-07	3DCM T24/83 ▲▲	EMT, N	T3/T4 vs T2 ▲ Died ▲ Recurred ▲	<u>8.04E-03</u> <u>1.64E-02</u> <u>1.92E-02</u>	nv	8.40E-05
LAMC1	2.34E-03	5.48E-03	3DCM T24/83 ▲▲	EMT, N, C	Died ▲ Recurred ▲	<u>1.41E-02</u> <u>2.18E-02</u>	1.90E-05	8.50E-07
LRP1	1.24E-03	5.52E-05	3DCM T24/83 ▲▲	EMT	pN+ ▲ T3/T4 vs T2 ▲ Died ▲ Recurred ▲	<u>1.78E-02</u> <u>1.11E-04</u> <u>9.19E-04</u> <u>9.57E-03</u>	3.50E-05	1.10E-04
P4HA2	<u>9.63E-03</u> 2.34E-02	<u>7.49E-05</u> 1.73E-03	<u>3DCM T24/83 ▲▲</u> 3DUCM T24/83 ▲▲	<u>ESC, C</u> ESC	Died ▲ Recurred ▲	<u>3.66E-02</u> <u>2.93E-02</u>	nv	2.90E-04
PLOD1	<u>2.78E-03</u> 8.49E-03	<u>2.26E-04</u> 1.94E-03	<u>3DCM T24/83 ▲▲</u> 3DUCM T24/83 ▲▲	EMT	Died ▲	<u>1.0E-02</u>	3.70E-05	1.90E-04
SUMF2	3.07E-02	1.62E-02	3DUCM T24/83 ▲▲	PTM	T3 vs T2 ▲ Died ▲	<u>4.73E-02</u> <u>2.87E-02</u>	2.10E-04	nv

MS = mass spectrometry; MA = microarray; N = neuronal pathways, C = cancer pathways,

▲ = increased protein expression *in vitro*; ▲ = increased mRNA expression *in vitro*;

\* = adjusted p-values; nv = not valid

In consideration to the OS probability of the MIBC patients, 5(12) targets (CALU, CD109, FBN1, HTRA1, SUMF2) were identified as increased expressed in patients with a decreased 5-year survival probability, ranged from about 20%-30%, in contrast to patients with lower gene expression (~50%-60% 5- year survival rate). On the other hand, DPYSL3, ITGB3 and P4HA2 were significantly higher expressed in patients with MIBC and thereby showed a decreased 5-year recurrence probability of about 30%, compared to those with a lower gene expression (~55% 5-year recurrence rate). The targets EGFR, LAMC1, LRP1, and PLOD1 represented a lower 5-year probability for OS (~20%-30%) and DFS (~20%-30) within patients with higher gene expression detected, while patients with a lower gene expression presented 5-year probability rates of about 50% -55% for both. In case of EGFR and ITGB3, they were not further considered for uni- and multivariable analysis, because their bee swarm plots indicated a very low gene expression within the *in silico* cohort, so they were defined as invalid for further investigations (Figure 13, Figure 14).

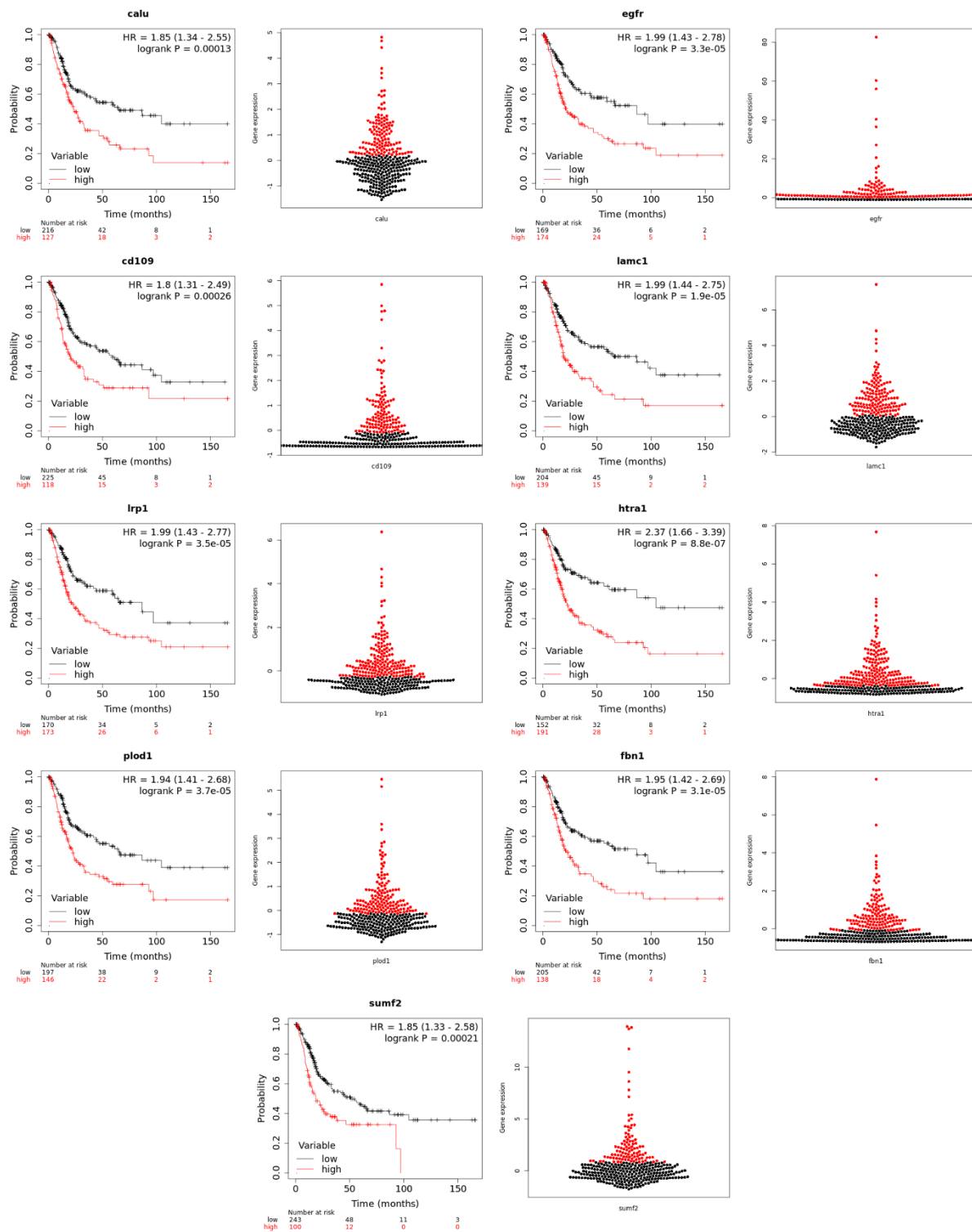


**Figure 13: Significant OS prediction in relation to target expression in MIBC patients**

mRNA gene expression of the 12 selected targets was correlated to OS in the MIBC TCGA cohort, thus indicate an overall shortened survival for patients with high target expression. Cutoff values were generated by the KMplotter online tool through the ‘automatic best select cutoff’ function, and log-rank statistic was applied. Only significant results with a false discovery rate lower or equal to 0.05, and a p-value<0.05 were considered. OS prediction is presented as Kaplan-Meier plot and group distribution as bee swarm plot.

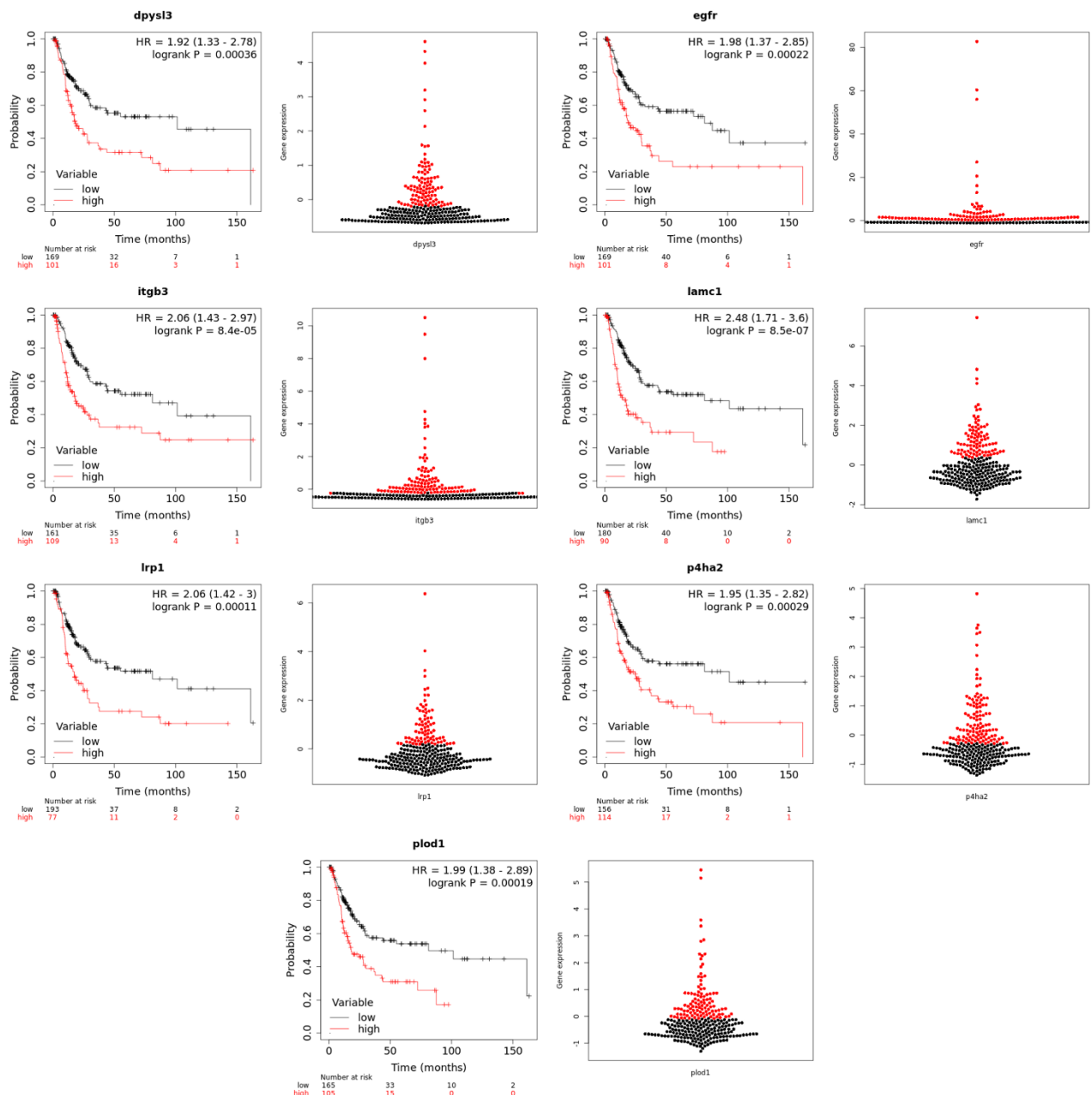


**Figure 14: Significant DFS prediction in relation to target expression in MIBC patients**

mRNA gene expression of the 12 selected targets was correlated to DFS in the MIBC TCGA cohort, thus indicate an increased probability of disease recurrence for patients with high target expression. Cutoff values were generated by the KMplotter online tool through the ‘automatic best select cutoff’ function, and log-rank statistic was applied. Only significant results with a false discovery rate lower or equal to 0.05, and a p-value<0.05 were considered. OS prediction is presented as Kaplan-Meier plot and group distribution as beeswarm plot.

Finally, the remaining 10 targets, and the clinicopathological parameter, such as age, gender, T-stage, and pN-stage, where further analyzed by uni- and multivariable stepwise Cox regression, according to OS and DFS. As expected, higher pT-stage (T3/4) and positive pN-stage (pN+) turned out as significant risk factors for patients with MIBC, regarding OS and DFS

probability. In detail, patients with a T-stage T3 or T4 have a 1.9- or 2.6-fold higher risk to die, and a 2.6- or 3.8-fold higher risk for disease recurrence, respectively, compared to those with T2. Patients diagnosed with lymph node metastasis own a 2.2- and 2.5-fold higher risk to die or recurred from disease, respectively. Other factors as age or gender did not showed significantly increased risks for dying or recurrence from disease. In case of the validated 10 targets, an increased gene expression is associated significantly with a higher risk for patients to die or recurred from disease. For OS, the Hazard ratios range from 1.6 to 2.3, and for DFS from 1.8-2.4 (Table 5).

**Table 5: Univariable proportional Hazard analysis of validated targets in MIBC patients**

	variables		OS		DFS	
			HR	p-value	HR	p-value
<b>target</b>	CALU +	CALU -	1.8116	<b>0.0005</b>	1.8657	<b>0.0019</b>
	CD109 +	CD109 -	1.7906	<b>0.0008</b>	1.8336	<b>0.0030</b>
	DPYSL3 +	DPYSL3 -	1.6912	<b>0.0019</b>	1.8932	<b>0.0007</b>
	FBN1 +	FBN1 -	1.9418	<b>&lt;0.0001</b>	1.7553	<b>0.0029</b>
	HTRA1 +	HTRA1 -	2.3060	<b>&lt;0.0001</b>	1.8442	<b>0.0013</b>
	LAMC1 +	LAMC1 -	2.2176	<b>&lt;0.0001</b>	2.3999	<b>&lt;0.0001</b>
	LRP1 +	LRP1 -	1.9372	<b>0.0001</b>	2.0201	<b>0.0004</b>
	P4HA2 +	P4HA2 -	1.5880	<b>0.0066</b>	1.8949	<b>0.0007</b>
	PLOD1 +	PLOD1 -	1.8260	<b>0.0004</b>	1.9054	<b>0.0007</b>
	SUMF2 +	SUMF2 -	1.7968	<b>0.0013</b>	2.0244	<b>0.0022</b>
<b>age</b>	continuous range			<i>0.1262</i>		0.9193
<b>gender</b>	female	male	1.1619	0.4205	1.1342	0.5467
<b>pT-stage*</b>	T3a/b	T2a/b	1.9467	<b>0.0025</b>	2.5510	<b>0.0002</b>
	T4a/b	T2a/b	2.6038	<b>0.0005</b>	3.8172	<b>&lt;0.0001</b>
	T4a/b	T3a/b	1.3375	<i>0.1880</i>	1.4964	<i>0.0950</i>
<b>pN-stage</b>	pN +	pN -	2.1978	<b>&lt;0.0001</b>	2.5000	<b>&lt;0.0001</b>

OS = overall survival; DFS = disease-free survival; HR = Hazard ratio; p-value in **bold** <0.05; *italic* = not significant but considered for step wise multivariable Cox regression; not highlighted p-values = not significant.

For the stepwise Cox regression, variables with a p-value ≤ 0.2 from the univariable analysis were considered for the multivariable model, which was performed for each target in dependency on OS and DFS. Thus, T4 vs T3 for OS and DFS, as well as age for OS was further included. It turned out that T-stage (T4 vs T3) and age failed the model dependent on OS and DFS, being not significant.

Except for DPYSL3, all other targets are significantly independent predictors for OS, while patients with increased expression levels own an about 2-fold higher risk to die, within a Hazard ratio range of 1.6-2.2. Equally, T3 or T4 vs T2, as well as positive lymph node metastasis showed up as independent factors for OS, together with each target tested. For both characteristics, patients with a T-stage T3, T4 or lymph node metastasis have an about 2-fold higher risk to die, in contrast to those with T2 or no lymph node metastasis, respectively. For

higher-staged tumors, Hazard ratios ranged from 1.7-2.4, and 1.9-2.2 for patients which are positive for lymph node metastasis (Table 6).

In consideration to DFS, all 10 investigated targets turned out as significantly independent predictors for DFS, while patients with increased gene expression showed an about 2-fold higher risk for disease recurrence. The Hazard ratios ranged from 1.5-2.6. Similar to OS, higher-staged tumors and lymph node metastasis represented significantly independent prognostic factors together with each gene target tested. Patients with a higher-staged tumor (T3 or T4) own an approximately 2.5-fold higher risk for disease recurrence, compared to T2-staged ones, with Hazard ratios ranged from 2-3. Indeed, T4 vs T2 showed up a higher risk compared to T3 vs T2. Patients diagnosed with lymph node metastasis demonstrated an average 2-fold higher risk for disease recurrence. (Table 7).

## Results

**Table 6: Step wise multivariable Cox regression in relation to OS**

OS			CALU**		CD109**		DPYSL3**		FBN1**		HTRA1**		LAMC1**		LRP1**		P4HA2**		PLOD1**		SUMF2**	
	variables		HR	p-value	HR	p-value	HR	p-value	HR	p-value	HR	p-value	HR	p-value	HR	p-value	HR	p-value	HR	p-value	HR	p-value
target	CALU +	CALU -	1.6465	<b>0.0096</b>																		
	CD109 +	CD109 -			2.1916	<b>0.0001</b>																
	DPYSL3 +	DPYSL3 -					1.3930	0.0952														
	FBN1 +	FBN1 -							1.5656	<b>0.0228</b>												
	HTRA1 +	HTRA1 -									2.0590	<b>0.0006</b>										
	LAMC1 +	LAMC1 -											2.2452	<b>&lt;0.0001</b>								
	LRP1 +	LRP1 -													1.7376	<b>0.0066</b>						
	P4HA2 +	P4HA2 -															1.5764	<b>0.0196</b>				
	PLOD1 +	PLOD1 -																	1.8088	<b>0.0022</b>		
	SUMF2 +	SUMF2 -																			1.7411	<b>0.0071</b>
age	continuous range			0.3724		0.2845		0.3894		0.5099		0.4583		0.3543		0.4411		0.3712		0.4285		0.5427
pT-stage	T3a/b	T2a/b	1.8482	<b>0.0155</b>	1.9189	<b>0.0103</b>	1.9530	<b>0.0074</b>	1.8455	<b>0.0156</b>	1.8096	<b>0.0195</b>	1.7727	<b>0.0239</b>	1.7310	<b>0.0321</b>	1.9415	<b>0.0082</b>	2.0211	<b>0.0050</b>	1.9500	<b>0.0074</b>
	T4a/b	T2a/b	2.3683	<b>0.0094</b>	2.0823	<b>0.0307</b>	2.3523	<b>0.0090</b>	2.2114	<b>0.0157</b>	2.2626	<b>0.0140</b>	2.2064	<b>0.0173</b>	2.1567	<b>0.0196</b>	2.2638	<b>0.0142</b>	2.4458	<b>0.0065</b>	2.4124	<b>0.0076</b>
	T4a/b	T3a/b	1.2814	0.3714	1.0852	0.7698	1.2044	0.4946	1.1982	0.5059	1.2503	0.4135	1.2446	0.4232	1.2460	0.4201	1.1660	0.5769	1.2101	0.4841	1.2371	0.4350
pN-stage	pN +	pN -	1.9918	<b>0.0007</b>	2.2020	<b>&lt;0.0001</b>	1.9424	<b>0.0011</b>	2.0199	<b>0.0004</b>	2.0575	<b>0.0004</b>	1.9199	<b>0.0010</b>	2.0085	<b>0.0005</b>	2.0788	<b>0.0002</b>	2.0736	<b>0.0003</b>	2.0373	<b>0.0004</b>

\* p<0.05 for univariable proportional Hazard analysis; \*\*p<0.05 for multivariable Cox regression; high gene expression is indicated by (+) and low gene expression by (-); pT = tumor stage; pN+ = lymph node metastasis present; pN- = lymph node metastasis absents.



## Results

**Table 7: Step wise multivariable Cox regression in relation to DFS**

	<b>DFS</b>		<b>CALU**</b>		<b>CD109**</b>		<b>DPYSL3**</b>		<b>FBN1**</b>		<b>HTRA1**</b>		<b>LAMC1**</b>		<b>LRP1**</b>		<b>P4HA2**</b>		<b>PLOD1**</b>		<b>SUMF2**</b>	
	<b>variables</b>		HR	p-value	HR	p-value	HR	p-value	HR	p-value	HR	p-value	HR	p-value	HR	p-value	HR	p-value	HR	p-value	HR	p-value
<b>target</b>	CALU +	CALU -	1.6183	<b>0.0165</b>																		
	CD109 +	CD109 -			1.6254	<b>0.0142</b>																
	DPYSL3 +	DPYSL3 -					1.7074	<b>0.0058</b>														
	FBN1 +	FBN1 -							1.4864	<b>0.0398</b>												
	HTRA1 +	HTRA1 -									1.6177	<b>0.0152</b>										
	LAMC1 +	LAMC1 -											2.5700	<b>&lt;0.0001</b>								
	LRP1 +	LRP1 -												1.7482	<b>0.0047</b>							
	P4HA2 +	P4HA2 -														1.7041	<b>0.0050</b>					
	PLOD1 +	PLOD1 -																1.5727	<b>0.0229</b>			
	SUMF2 +	SUMF2 -																			1.9782	<b>0.0061</b>
<b>age</b>	continuous range																					
<b>pT-stage</b>	T3a/b	T2a/b	2.1497	<b>0.0029</b>	2.1616	<b>0.0027</b>	2.1277	<b>0.0033</b>	2.0159	<b>0.0074</b>	2.0786	<b>0.0046</b>	2.1797	<b>0.0022</b>	1.9919	<b>0.0081</b>	2.0962	<b>0.0040</b>	2.1499	<b>0.0029</b>	2.1346	<b>0.0030</b>
	T4a/b	T2a/b	2.9284	<b>0.0008</b>	2.6630	<b>0.0024</b>	3.0256	<b>0.0006</b>	2.6405	<b>0.0024</b>	2.7709	<b>0.0015</b>	2.9629	<b>0.0007</b>	2.7140	<b>0.0019</b>	2.6894	<b>0.0022</b>	2.9511	<b>0.0008</b>	2.8013	<b>0.0013</b>
	T4a/b	T3a/b	1.3623	0.2196	1.2319	0.4022	1.4220	0.1624	1.3099	0.2765	1.3331	0.2498	1.3593	0.2196	1.3625	0.2185	1.2830	0.3199	1.3727	0.2089	1.3123	0.2744
<b>pN-stage</b>	pN +	pN -	1.9227	<b>0.0010</b>	2.0256	<b>0.0003</b>	1.9039	<b>0.0011</b>	2.0476	<b>0.0002</b>	1.9739	<b>0.0006</b>	2.2344	<b>&lt;0.0001</b>	2.0157	<b>0.0004</b>	2.0136	<b>0.0004</b>	1.8410	<b>0.0026</b>	2.1015	<b>0.0001</b>

\* p<0.05 for univariable proportional Hazard analysis; \*\*p<0.05 for multivariable Cox regression; high gene expression is indicated by (+) and low gene expression by (-); pT = tumor stage; pN+ = lymph node metastasis present; pN- = lymph node metastasis absents.

#### 4.3.4 ECM-based biological mechanisms of *in silico* validated targets

Besides the significant determination and validation of the 10 identified targets, their biological background was further characterized to investigate their origin and participation within biological processes (Figure 15). Directly related to the ECM are LAMC1, FBN1, and PLOD1. All the ECM-based targets are significant for increased EMT, while LAMC1 additionally occurs also for increased neuronal activity, and can be related to upregulated RAF1/MAP2K1/ERK pathway.

The remaining 7 targets are ECM-interacting ones, because they are not a direct component of the ECM. As also identified for the ECM-based targets, higher neuronal activity (CD109, DPYSL3) and EMT process (CALU, DPYSL3, HTRA1, LRP1) was significantly detected. Further, increased ESC (HTRA1, P4HA2) and PTM (SUMF2) was observed, and a raised P4HA2 expression linked to erb-b2 receptor tyrosine kinase 2 pathway upregulation.

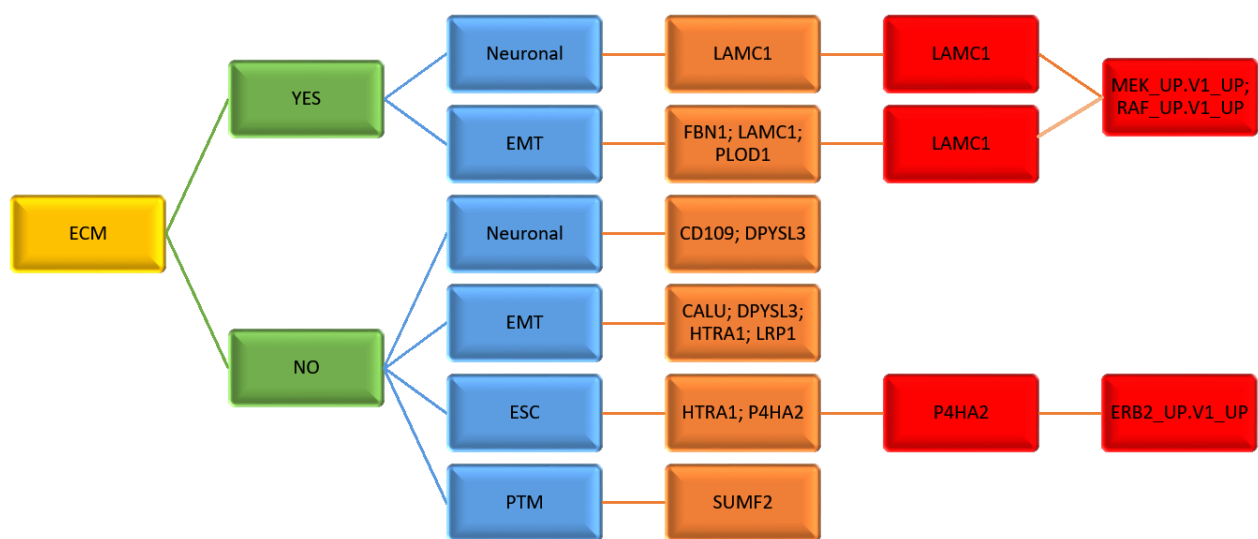


**Figure 15: Scheme of target origin and pathway involvement**

Graphical summary of validated targets dependent on their affiliation to the ECM compartment and their participation within significantly expressed gene sets, as well as cancer pathways.

## 5 DISCUSSION

### 5.1 3D BC cell line *in vitro* model

#### 5.1.1 Environmental setting for 3D *in vitro* system

Successful culturing of cell lines is dependent on multiple factors. Usually, for each cell line there is a certain medium available recommended by the supplier, and selected due to proper cell growth and morphology. From the physiological point of view, culturing different cell lines from the same entity in different media each, no consistent environment is given although the cell lines originate from the same organ. By this reason, uniform medium conditions were investigated for the *in vitro* cultivation of BC cell lines. The conditions under Mc Coy's + 10% FBS and DMEM + 10% FBS in 2D culture turned out to be more stable in terms of pH and oxygen over culturing time, according to common achievable pH (~7.4) and oxygen (~21 %) values for 2D *in vitro* systems.

Indeed, depending on different medium ingredients and compositions, media conditions can change the phenotype of several cell lines. For instance, culturing melanoma cell lines in stem cell medium lead to an expression of neuronal profile(93). In breast cancer cell lines, different compositions of DMEM and RPMI medium had an impact on subtype characteristics(94), and for pancreatic and gastric cancer cell lines, DMEM and RPMI cultures showed different metabolic profiling (95,96). But not only the use of different basal media is responsible for phenotype change, also the addition of antibiotics can influence important cellular features. The use of gentamicin for culturing epithelial and breast cancer cells is associated to increased HIF1a, aerobic glycolysis and oxidative DNA damage(97). Since the choice of culture medium is in fact a point with highly variable effects for *in vitro* studies, it is becoming more questionable how to interpret and compare existing results. Under consideration that the use of different basal media can change the phenotype, or the addition of antibiotics can cause DNA damage, previous comprehensive studies of cancer cell lines may become inaccurate as translational clinical finding. Hence it can be assumed that widely used public genomic, transcriptomic and proteomic cell line databases(98,99) are influenced by the use of different media conditions. So far, there are no studies describing the impact of culture conditions on BC cell lines phenotype or genotype. However according to the previous findings in other entities, similar effects cannot be excluded or ignored for BC cell lines.

Translational *in vitro* models are highly important tools for biomedical cancer research. Since the early 1900, the 2D *in vitro* system was developed, and was considered to be the gold standard so far. However, the 2D system surely lacks cellular arrangement for *in vivo* condition, so that animal-based models are extensively used to fill this gap. But even the translation from *in vivo* models demonstrated very often inaccurate prediction in relation to the human body.

Apart from that, *in vivo* models under strict law regulations, are expensive, and the handling is very elaborate. Meanwhile, several studies showed that 3D *in vitro* systems can overcome the problem of oversimplified 2D and unrepresentative *in vivo* models. Previous findings showed that 3D *in vitro* models present a more natural morphology thus cells are arranged as spheroids or aggregates. Due to the spheroidal structure, the exposure to nutrients and oxygen is similar to *in vivo* conditions, and more pronounced cell junctions are formed. As often described for solid tumors, the spheroid core lacks exposure of nutrients and oxygen leading to a hypoxic environment and inactive cells, while the outer layer represents metabolically active cells. This distinct imbalance and generation of a unique environment also leads to a more natural cell proliferation within the spheroids, while in contrast 2D cells exhibit an unnatural rapid proliferation. Altogether, these structural and environmental factors also have an impact on the gene and protein expression, while the 3D system demonstrated a more realistic pattern compared to the 2D system(100).

The field of 3D *in vitro* culture demonstrated noticeable advantages but is not established for BC so far. By this reason, BC cell lines UROtsa, RT4, T24/83, and SCaBER were transferred from the 2D condition into a 3D application by the use of ULA plates. Culturing the cells only in basal medium was not successful for UROtsa, T24/83 and SCaBER, since the spheroids were degrading by time. Probably these cell lines were not able to produce their own matrix in basal medium to form stable and growing spheroids. This is not the case for RT4, those cells are known to form stable spheroids also in basal medium only, without any ECM enrichment(67). Under consideration of RT4 morphology in 2D, compared to the others, intensive colonized and multi-layered growth can be observed, as well as strong cohesion among the cells. This indicates that RT4 could be a high producing ECM cell line. To support the ECM, the addition of 50% UCM or CM fibroblast basal medium turned out to stabilize at least T24/83, and represented stable, growing and full integrities of the spheroids. Finally, RT4 as a non-invasive and T24/83 as an invasive BC cell line were successfully cultured under same media conditions in the 3D *in vitro* system. In contrast, UROtsa and SCaBER were not reproducible within the ULA application, and the used medium conditions. Maybe another 3D application is more suitable, as it was demonstrated previously for UROtsa and SCaBER, by the addition of type I collagen and Matrigel, respectively(101,102). Former studies on T24/83 cell line showed contrary results. First, T24/83 cells were cultured on agarose coated microplates, following the ULA principle. The Authors mentioned stable and growing T24/83 cells up to 11 days after seeding, however cultured under different medium conditions (RPMI + 10% FBS), and unfortunately they did not represent any data to underpin this statement(103). In contrast, T24/83 did not form spheroids by the addition of type I collagen within Minimum Essential Medium(101). To overcome the high impact of culture conditions to generate intact spheroids, it is commonly used to introduce Matrigel into the 3D system. Matrigel is a ECM

protein mixture derived from murine sarcoma cells, and brings the advantage to support especially cancer spheroids in shape and growth. Matrigel was former used to enrich cancer stem cells to study radiosensitivity in BC cell lines(104), and small molecules were screened on 17 different BC cell lines(102). The supporting function of Matrigel was clearly demonstrated for T24/83. The Authors cultured T24/83 as spheroids in RPMI + 10% FBS, and used them for viability analysis after 3 days of culture. They further performed invasion assays by the use of Matrigel, and observed a better developed spheroidal structure of the T24/83 spheroids(105). Altogether, these findings show the supportive function of Matrigel for spheroid culture, which seems to work well for various cell lines. However, this ECM is derived from non-human species, promotes malignant phenotype, and would be therefore not suitable for culturing benign cell lines. Despite this fact, Matrigel can vary from batch to batch which influences reproducibility. That's why Matrigel was deliberately omitted from this study(106).

## 5.2 Impact of UCM and CM on T24/83 spheroid formation and growth

Intact and proper growing spheroids of T24/83 were generated by the addition of 50% UCM or CM medium. Since the spheroids also represented stable properties without the fibroblasts conditioned variant, the fibroblast basal low-serum medium composition seems to serve as sufficient for spheroid formation and growth. The ingredients listed by the supplier are 7.5mM L-glutamine, 2% FBS, 50µg/ml ascorbic acid, 1µg/ml hydrocortisone, 5µg/ml recombinant human (rh) insulin, and 5ng/ml rh fibroblast growth factor (FGF) basic, while by mixing 50% UCM with 50% Mc Coy's + 10% FBS, results in half concentration of ascorbic acid, hydrocortisone, insulin and FGF basic in this 3D culture model. With respect to ascorbic acid, *Peng et al. (2018)* demonstrated an epigenetically change in T24 upon treatment with ascorbic acid. The exposure to 0.25mM (~44µg/ml) ascorbic acid caused a reduced cell viability in monolayer culture significantly, by increasing apoptosis, and in addition, decreasing malignant phenotype of T24 in *in vivo* xenografts(107). As it is mostly a matter of dosage, ascorbic acid also promotes collagen synthesis and stability by cancer cells and in *in vitro* culture of fibroblasts (108). In this study, the applied ascorbic acid concentration of 25µg/ml is almost half of the previous defined threshold inducing apoptosis. Thus, it can be assumed that the malignant phenotype was unchanged, collagen synthesis was induced in T24/83 cells, and therefore a stable spheroid formation was supported.

Moreover, 0.5µg/ml hydrocortisone is part of the UCM condition, and known to effect transitional cell hyperplasia negatively in a dosage dependent manner. This was former investigated in urinary bladders from Fischer rats in an organ culture. The authors determined a concentration of 0.76µg/ml (2.1µM) hydrocortisone inhibited hyperplasia by 75%(109). In addition, 1µg/ml hydrocortisone was successfully used to maintain normal adult human bladder in a long-term culture(110). In contrast to the here presented study, *S. F. Stinson et al. (1977)*

identified a much lower threshold of hydrocortisone-dependent inhibition of hyperplasia in urinary bladders from Fischer rats' organ culture. They introduced a threshold of 0.036 $\mu$ g/ml (10<sup>-7</sup>M) hydrocortisone, while concentrations above induced progressive decrease(111). With respect to *S. F. Stinson et al. (1977)*, the hydrocortisone concentration used in this present study was more than 10-fold higher, thus an impairment of malignant phenotype cannot be excluded. However, those former studies were applied on rodent species and consider only morphological features. It is clearly proven that hydrocortisone inhibits malignant appearance in a dosage-dependent manner, however the inducing dosage is not identified for T24/83 *in vitro*, so far.

Interestingly, previous studies cultured T24 cells in 3D models using ULA plates or a microwell chip platform in basal medium without Matrigel successfully(112,113). They added several supplements into the growth medium, including insulin, and/or FGF basic. As insulin and FGF basic are also part of the UCM condition, and by its addition to the basal medium stable spheroids were produced in this study, it can be assumed that those factors have a promoting impact on proper T24/83 spheroid formation and growth. Previously, scientists published the effect of high dose human insulin on T24 cell proliferation, and demonstrated an association to PI3K-independent activation of Akt signaling pathway. They treated T24 cells with 0.35 $\mu$ g/ml-3.48 $\mu$ g/ml (10IU/L-100IU/L)(114) human insulin in order to represent the link to Akt signaling(115). According to this finding, the human insulin concentration of 2.5 $\mu$ g/ml applied in this study can be assigned to the higher dose range, thus a cell proliferation promoting effect can be assumed within the 3D model of T24/83.

Furthermore, 2.5ng/ml FGF basic was also content of the UCM condition in this study. It is well known that FGF basic regulates growth, metastasis, invasiveness and angiogenesis in BC *in vitro* and *in vivo*(116–119). Also *in vitro* culturing of human bladder urothelial cells from patients with neurogenic bladder showed enhanced proliferation, migration and wound healing by FGF basic treatment, ranging from 5ng/ml-40ng/ml, in a dose-dependent manner(120). In the above mentioned *in vitro* 3D applications, T24 cells were treated with FGF basic concentrations of 20ng/ml(112,113). As in literature the effects of FGF basic on urothelial bladder cells was mainly observed upon concentrations almost 10-fold higher than used in this study, a significant effect by FGF basic treatment in this approach remains questionable.

Besides the UCM condition, a stable formation and proper growth of T24 spheroids was also observed under CM conditions. Compared to UCM, there was no significant difference in growth rate, but the spheroid morphology appeared in a rounder, more compact and smoother shape. This morphological difference must be an effect triggered by the primary normal bladder fibroblasts secretome, used as CM condition. But how can be estimated of what the 2D *in vitro* secretome of primary normal bladder fibroblasts is made of? According to *R. Kalluri*(121), quiescent fibroblasts can be activated by growth factors *in vitro*, e.g. FGF basic. Upon

activation they exhibit properties as proliferation, migration, and production of growth factors and ECM molecules. In total, they reflect properties crucial for wound healing and formation of connective tissue. *Kashpur et al. (2013)*, published a transcriptomic analysis of FGF basic treated induced regeneration-competent fibroblasts in comparison to normal adult dermal fibroblasts, and identified a unique gene expression profile. Gene expression of ECM components, adhesion molecules, matrix remodeling, cytoskeleton, and cytokines were reorganized due to FGF basic treatment(122). These findings demonstrate a high impact secretome of *in vitro* cultured fibroblasts, which is also implemented in bladder tissue regeneration, using FGF basic as promotor to regenerate tissue and improve function of neobladders(123,124). Furthermore, ingredients as ascorbic acid and insulin are known to induce collagen synthesis(108), and proliferation(125,126) *in vitro*, respectively. Moreover, the effect of hydrocortisone depends on fibroblast origin, and can support or impair cellular growth, and remodels ECM expression with respect to different types of collagens and matrix metalloproteinases(127,128).

Taking together, the rounder, smoother and more compact shape of the T24/83 spheroids, cultured under CM conditions, compared to UCM, can be explained by the secretome of 2D *in vitro* cultured primary normal bladder fibroblasts. It was previously demonstrated that the *in vitro* secretome is highly remodeled and its synthesis is pushed by FGF basic, ascorbic acid, insulin, and hydrocortisone exposure, thus the CM enriched exogenous ECM properties in the 3D *in vitro* model of T24/83. The effect of exogenous ECM enrichment by CM was observed to lead to tighter cellular, and better organized arrangements within the T24/83 spheroids.

At first, the goal was to establish a stable formation and growth of spheroids, deriving from BC cell lines. This was successfully achieved for the invasive cell line T24/83 under UCM and CM condition. Besides the different morphological appearance of T24/83 spheroids, cultured in UCM and CM, further expression analysis reveal more specific characteristics regarding 3D *in vitro* model and malignant features.

### 5.3 Invasive T24 spheroids harbor particular characteristics of 3D *in vitro* models

In a further application, T24/83 spheroids were analyzed by LC-MS, and DEP were applied for GSEA. Several 3D characteristics were identified to be up- or downregulated in comparison to 2D standard condition (Mc Coy's + 10% FBS).

As previously described, upon a particular size (~500µm), *in vitro* spheroids represent characteristic features. The aggregation of cells leads to the formation of a gradient for pH and nutrients. Cells in the inner core of the spheroid are less supplied with nutrients, and oxygen. This fact leads to a necrotic core of cells, while the superficial cells are proper exposed to nutrients, and show proliferating activity(63). As a logical consequence, apoptosis events are more frequently in spheroids(129), and due to the oxygen gradient, inner core hypoxia can be

reflected(130). Furthermore, the cells in a spheroid need to form or be provided with ECM components to stable their cellular arrangement and interaction(63). According to these facts, T24/83 spheroids where identified with less proliferative activity, higher apoptosis, greater expression of ECM, and hypoxia in contrast to the 2D model. In addition, T24/83 spheroids also demonstrated increased PTM, compared to the 2D model. Since posttranslational protein modifications, as glycosylations, are essential structures of the ECM, thus an increase could be assumed for 3D spheroid culture(131,132).

It is clearly demonstrated that 3D *in vitro* systems are more complex than 2D system, and apply a successful 3D system is highly dependent on the cell line, the selected model, the culture medium and its supplements. However, it is well known that cancer-based 3D *in vitro* models are able to reflect *in vivo* conditions more realistic. Thus, it is urgent to develop at least for a certain cancer entity a standardized procedure to guarantee comparability of 3D *in vitro* applications, and a better translation to *in vivo* conditions.

#### 5.4 Predomination of ECM-related malignant features and targets in the invasive T24/83 3D *in vitro* model

Proteomics-based GSEA revealed further characteristics of T24/83 spheroids compared to the 2D standard condition. With respect to dominantly appearing features, properties as ECS, EMT, DNA repair, cancer-related pathways, and neuronal pathways were highlighted. Since it was aimed to identify ECM-related pathways, significantly differential expressed ECM gene sets were matched against all significantly differential expressed gene sets. The results showed an involvement of ECM proteins within ECS, EMT, neuronal-, and cancer-related pathways. The significantly DEP from the resulting pathways, plus the proteins from significantly expressed glycosylations, were further validated by their mRNA expression *in vitro*, and by *in silico* mRNA expression data of MIBC patients. In addition, correlation to OS, DFS, and clinicopathological parameters was determined. Only potential targets which were significantly differential expressed on protein- and mRNA-level, as well as associated to patients' survival prediction, and progressive clinicopathological factors, were selected. By this analysis, 10 different targets resulted. All of them were upregulated on protein- and mRNA-level in T24/83 3D model, in contrast to the 2D condition. Equally, elevated mRNA expression in MIBC patients had an impact on poor outcome, with respect to survival prediction and progressive tumor properties.

Under consideration of significantly DEP, the data showed only an abundance of about 1/25 of DEP, and 1/3 of DEG for 2D UCM (3D UCM); 1/57 of DEP, and 1/4 of DEG for 2D CM (3D CM), in contrast to 2D standard condition. Based on these findings, highly significant differences between the UCM and CM condition were not expected. However, 6(10) of the final selected targets were found to be significantly expressed in the 3D CM condition, compared



to 2D standard condition. Furthermore, 2(10) targets were different in both conditions, and 2(10) only for 3D UCM. Since more than a half of the validated targets are differential expressed in the 3D CM vs 2D standard condition, this indicates that a differential genotype resulting from the 2D model under different medium conditions cannot be used as a translation to the 3D model under different medium conditions. Apparently, an interplay of the used *in vitro* model and a certain medium condition obtains a unique genotype. Thus, the genotypic effects of the used medium condition in the 3D model cannot be predicted by the lower dimensional 2D model.

#### 5.4.1 Validated ECM-based targets

The gene LAMC1 encodes for the glycoprotein laminin gamma 1 subunit, and is essential for the linkage of the extracellular basement membrane with the plasma membrane through its c-terminal integrin binding site(133). According to the conducted GSEA, LAMC1 is participating in EMT and neuronal pathways, and further in cancer-related RAF1/MAP2K1/ERK pathway, promoting cell proliferation. Interestingly, the RAF1/MAP2K1/ERK pathway was previously demonstrated as promising target to treat BC basal subtype, identified by 3D cell culture screenings(102). Furthermore, LAMC1 overexpression was reported for several solid malignancies, as glioblastoma(134–136), uterine(137,138), cervical(139), prostate(140), hepatocellular(141,142), and colorectal(143), indicating an association to poor outcome for patients, migration and metastatic features. According to these findings, similarities are consistent with the data of this study, representing elevated EMT and neuronal pathway activity for the 3D CM model of the invasive BC T24/83 cell line, and furthermore, the correlation between high LAMC1 expression with worse prediction and progression in the *in silico* validation.

The glycoprotein fibrillin-1, encoded by the gene FBN1, is the major component of microfibrils fibers located in the connective tissue. Microfibrils have structural and functional properties, and are components of the ECM. They participate in cell matrix interactions such as with integrins, and transforming growth factor- $\beta$ (144,145). A former study performed a weighted gene co-expression, and protein-protein interaction network analysis of BC expression data. They showed a link of increased FBN1 expression with poor OS, and identified an association to BC progression due to FBN1 enrichment within the ECM-receptor interaction gene set(146). Equally, elevated proteins levels of FBN1 were determined to be enriched within the ECM-receptor interaction gene set, indicating invasive properties in glioblastoma(147). Also higher FBN1 expressions were identified for gastric(148–150) and ovarian(151–153) cancer, while FBN1 was correlated with poor prognosis, and progressive features. Interestingly, FBN1 was demonstrated to be upregulated under hypoxic conditions in renal carcinoma(154), and can act as fluorescence probe for hypoxia detection in cancer cells(155). Mechanistically,

FBN1 was determined to promote EMT, invasion and metastasis in osteosarcoma(156). Compared to this study, an elevated FBN1 expression on protein-, and mRNA level for the invasive T24/83 *in vitro* 3D CM model, and its enrichment in the GSEA can be confirmed, as well as an association to poor prognosis and progression in clinical MIBC samples. This indicates an involvement of FBN1 in tumor progression, and validated the elevated hypoxia conditions of the 3D model, in contrast to the 2D standard condition.

The expressed protein of the PLOD1 gene is called procollagen-lysine,2-oxoglutarate 5-dioxygenase 1, and catalyzes the hydroxylation of lysine residues in collagen alpha chains, which is required for proper cross-linking and glycosylation of collagen fibrils(157). Previously, PLOD1 mRNA expression was positively associated to poor survival, and turned out as independent prognostic factor in BC clinical specimens. The inhibition of PLOD1 mRNA and protein function *in vitro* reduced BC cell aggressiveness(158). These findings are consistent to this study, thus a multi-omics overexpression in the invasive T24/83 3D UCM and CM model was linked to EMT events through GSEA. In addition, progressive factors were also confirmed by *in silico* validation of MIBC clinical samples, indicating PLOD1 as a significant player in bladder tumor prognosis and invasive progression. Besides BC, a hypoxia-induced PLOD1 overexpression was linked to malignancy of glioblastoma(159), while its transcriptionally activation is induced by the hypoxia-inducible factor 1 in breast cancer cells(160). Since in this study PLOD1 is overexpressed in the 3D compared to the 2D model, this aspect supports the data presented here of increased hypoxia in the 3D model of T24/83. Further connection to high PLOD1 levels and poor clinical outcome was observed for renal(161), hepatocellular(162), osteosarcoma(163,164), and colorectal and gastric carcinoma(165–167). Taking together, the ECM-based determined targets are clearly involved into tumor progression, and poor outcome of patients. They are all participating in EMT, indicating their invasive and metastatic potential. Furthermore, the associations found here, as neuronal activity pathways (LAMC1), cancer pathways (LAMC1), and hypoxia-dependency (FBN1, POLD1) are novel insights for MIBC.

#### 5.4.2 Validated ECM-interacting targets

Calumenin is a glycoprotein, encoded by the CALU gene, and its location was detected in the endoplasmic reticulum, Golgi apparatus, and the extracellular space. It acts as part of secretory mechanisms as a chaperone protein, in protein structure modeling, protein maturation, activation of enzymes located in the endoplasmic reticulum, regulation of cellular stress, and cell cycle modulation(168,169). There are no previous studies exist, describing its impact on BC, however for certain other entities associations were identified. For instance, several approaches linked an increased expression of CALU mRNA or protein to colon(170), neuronal(171), melanoma(172), and lung(173) cancer. Upon mRNA silencing, an inhibition of

cell growth, invasion, metastasis, and inducing apoptosis and cell cycle arrest was detected in mucosal melanoma *in vitro*(172). In clinical lung cancer samples, calumenin expression was elevated in metastasis positive tissue, while 80% of these patients were diagnosed with lymph node metastasis. Its impact on lung cancer invasiveness was further confirmed by mRNA silencing *in vitro*(173). According to these previous findings, the data from this study supporting the relation of an increased CALU expression and its correlation with progressive features as novel finding for MIBC. Based on the 3D CM *in vitro* model of T24/83, CALU expression was determined to be upregulated on mRNA-, protein-level, and was enriched for the EMT gene set, in contrast to the 2D standard condition. The same direction of mRNA expression was observed in the TCGA cohort of MIBC patients, and a linkage to progressive factors and worse survival prediction, indicating the involvement of CALU within invasive, and metastatic properties.

The CD109 gene encodes the CD109 antigen, a glycosylphosphatidylinositol-anchored cell-surface glycoprotein. With respect to cancer, it was mainly reported to be expressed in squamous cell carcinoma. CD109 antigen is described to mediate tumorigenicity and aggressiveness via CD109/EGFR/STAT3 signaling(174–176). In human urothelial carcinoma tissue, CD109 protein expression and phosphorylated Smad2 exhibited an inverse relationship, indicating that CD109 antigen impairs TGF- $\beta$ /Smad signaling in tumor tissues. The Authors further identified a higher CD109 protein expression in the basal layer of non-muscle-invasive species compared to muscle-invasive ones, however, no expression was detected in normal bladder epithelia. Therefore, they suggest CD109 antigen as potential target for immunotherapy, and its role in bladder tumorigenesis(177). Concerning this previous study, the data determined in this study considered the CD109 antigen and mRNA expression in muscle-invasive urothelial bladder carcinoma *in vitro* and of MIBC clinical data. For the 3D T24/83 *in vitro* model, an increased expression on protein and mRNA level was found in contrast to the 2D condition. Within the muscle-invasive population, elevated levels were validated in relation to worse prognosis and progression in patients, thus the data here supporting the CD109 antigen involvement in tumorigenesis, and its potential use as target for immunotherapy. Further the GSEA linked the CD109 antigen expression to neuronal pathways. Interestingly, previous studies on malignant neuronal disease reported an overexpression of CD109 protein in brain tumor stem cells. These studies showed that CD109 expression mediates radioresistance, and proliferation to adjacent cells(178–180). Another example for therapy resistance was observed for ovarian cancer patients. They detected CD109 protein and mRNA levels, and showed higher rates of CD109 antigen in patients with poor response to chemotherapy, compared to those with good response(181). In lung cancer studies, CD109 antigen was extensively investigated, and its overexpression was associated to invasion through TGF- $\beta$  signaling, metastasis, EMT, stem cell properties, and drug

resistance(182–185). Taking together, CD109 antigen clearly drives malignant progression in cancer, however its fully impact on BC is still poorly investigated.

The dihydropyrimidinase-related protein 3 is encoded by the DPYSL3 gene, and refers to the collapsing response mediator proteins. DPYSL3 protein is intracellularly located and activated by extracellular signals during neuronal migration, differentiation, remodeling of cytoskeleton, and neuronal growth(186). In some cancerous entities, DPYSL3 was determined as a tumor suppressor, as in prostate, hepatocellular carcinoma, and neuroblastoma(187–193). On the other hand, DPYSL3 was reported to promote tumor progression within renal, colorectal, gastric, and pancreas entity(194–198). It was described as independent predictive marker in metastatic gastric cancer patients with an increased expression promoted tumor growth and metastasis(196,197). In colorectal cancer, *in vitro* and *in vivo* applications also showed an association to proliferation and tumor growth, respectively(195). The role of DPYSL3 protein in pancreatic cancer revealed a relation to adhesion and migration *in vitro*, and metastasis *in vivo*(198). With respect to BC, no one studied the impact of DPYSL3 expression so far. Here, the results of the *in vitro* 3D model of T24/83 demonstrated an elevated level of DPYSL3 protein and mRNA, compared to the 2D standard model, and was validated in a MIBC TCGA cohort, reflected an association of high DPYSL3 expression with poor prognosis and tumor progression. In addition, the data linked DPYSL3 expression to neuronal and EMT process through GSEA, as described for other cancerous diseases. According to previous findings in other entities, the data identified in this study, indicate DPYSL3 as tumor promoter in MIBC, reflected by the 3D model and the mRNA expression profile of MIBC patients.

The low-density lipoprotein receptor-related protein 1, also called CD91 antigen, is a transmembrane receptor which mediates endocytosis and signaling pathways, encoded by the LRP1 gene. With respect to cancer, it plays an important role in cellular growth and differentiation, cytoskeleton modulation, angiogenesis, migration, and invasion(199). The expression of the LRP1 protein seems to be dependent on oxygen conditions. It was demonstrated that during hypoxic conditions, the LRP1 protein expression raised, compared to when cultured under norm oxygen conditions, as it is performed for standard 2D cell culture(200). Considering this fact, the data in this study also showed an increased LRP1 protein and mRNA expression in the 3D *in vitro* model of T24/83, compared to the 2D model, and was linked to EMT by GSEA. Furthermore, its expression was confirmed in the MIBC TCGA cohort, with regard to poor disease prognosis and progression. Previously, the same outcome of prognosis was reported for LRP1 mRNA expression, also based on the TCGA cohort of bladder urothelial carcinoma(201). Similarities were described for renal and pancreatic cancer, while elevated LRP1 protein levels were associated with higher staged tumors, lymphatic invasion, and poor prognosis(202,203). Further, LRP1 is referred as gemcitabine resistance-related gene, and higher expressed in gemcitabine-resistant BC cell

line T24(204). As demonstrated for colon cancer, targeting LRP1 protein enhanced the efficacy of neo-adjuvant radiotherapy(205). In the same entity, in 3D collagen matrices, the LRP1 protein mediated endocytosis of epithelial discoidin domain-containing receptor 1 increased cell proliferation, and decreasing apoptosis(206). Mechanistically, LRP1 triggered kinase signaling, ECM remodeling, and metastatic spread in breast cancer tumor models(207). In thyroid cancer 3D model, silenced LRP1 protein impaired cell migration(208), and restoration leads to lung metastasis in rodent tumor models(209). Since LRP1 is directly linked to drug resistance and metastasis it might serve as therapeutic biomarker for MIBC patients. On the other hand, LRP1 protein elevation is also described in an opposite direction for prostate(210) and hepatocellular carcinoma(211), indicating an entity-dependent expression pattern. However, the data presented in this study clearly contribute to raised LRP1 protein, and mRNA levels, which can be explained due to hypoxic conditions within the 3D invasive T24/83 model. The enrichment of EMT features by GSEA support the LRP1 involvement to ECM remodeling, metastatic spread, and was further confirmed through validation by TCGA MIBC patients.

The high-temperature requirement A serine peptidase 1, is expressed by the HTRA1 gene, and is secreted in the extracellular space or located in the cytoplasm, attached to microtubules. It has a digestive function in the extracellular space, while it was described as tumor suppressor intracellularly(212). Hence, the Inhibition of HTRA1 protein in the tumor stroma diminished tumor progression by deregulating angiogenesis(213). It was demonstrated that HTRA1 protein can be expressed in its native form of ~50 kDa, and as its autocatalytic form of ~35 kDa, generated by the protease activity(214). The differential expression of these forms was previously investigated in BC specimens. The study showed that the autocatalytic form was highly reduced in BC, compared to normal-looking tissue, while the native form was not differently expressed between the two cases. They further demonstrated the absence of secreted and intracellular HTRA1 protein in T24 2D cultures cell lines(215). In contrast to the study presented here, the results exhibited elevated intracellular levels of HTRA1 protein and mRNA in the 3D culture model of T24/83, compared to the 2D model. These finding could indicate a higher expression due to the use of the 3D model, and might contribute to spheroid formation, thus HTRA1 protein is attached to microtubules. Since the validation in MIBC patients was only conducted on mRNA level, increased expressions of HTRA1 mRNA can predict outcome and tumor progression, however the protein level can be regulated differently. Therefore, the results in this study do not make any statement about protein expression in patients. But the levels of HTRA1 protein was identified as tissue specific and can change during pathogenesis(216). Besides the mainly described tumor suppressive function of HTRA1 protein(217–223), an upregulation in gastric cancer is associated to worse prognosis, and higher levels in cell lines were identified to induce the transformation of normal to cancer-

associated fibroblasts(224), indicating a contrary impact of HTRA1, which seems to be dependent on cancer entity.

The prolyl 4-hydroxylase subunit alpha-2 catalyzes the hydroxylation of 4-hydroxyproline residues in collagens, and is important for the collagen triple helix stability. It is encoded by the P4HA2 gene, part of the collagen prolyl 4-hydroxylase 2 complex, and is located in the endoplasmic reticulum(225). Previously, an upregulated P4HA2 expression was extensively described for several malignant diseases, however its expression and impact on BC is still unexplored. In this study, an upregulation of P4HA2 protein and mRNA level was determined in the *in vitro* 3D model of T24/83, compared to the 2D standard condition, and its enrichment in ESC features and erb-b2 receptor tyrosine kinase 2 (also referred to HER2) signaling, detected through GSEA. Its mRNA expression was correlated with poor prognosis and tumor progression in the *in silico* validation of MIBC patients. As demonstrated in breast cancer, P4HA2 mRNA was detected to be upregulated and correlated with poor outcome, and its inhibition in 3D *in vitro* model showed reduced collagen deposition, and diminished tumor growth and lung metastasis in xenograft models(226). In addition, its abnormal expression was also detected for HER2-positive phenotypes(227). Interestingly, P4HA2 was also described to act in a hypoxic-dependent manner, while promotion of invasion and metastasis was observed in breast cancer(228). In cervical cancer, P4HA2 was suggested as oncogene by inducing EMT, and its raised protein expression is linked to a poor survival prognosis for patients(229,230). To make the list complete, similar findings were published for different squamous cell carcinoma(231–233), hepatocellular carcinoma(234,235), and melanoma(236). Covering the aspect of P4HA2 and its relation to stem-like features, the increased P4HA2 protein expression leads to high collagen deposition, and elevates ECM stiffness, which caused stem-like programming and metastatic dissemination in *in vivo* lung cancer models(237). By transferring the previous knowledge, it can be suggested that increased P4HA2 expression associate with cancer cell stem cell features, and higher probability for metastatic behavior in MIBC.

The glycosylated sulfatase-modifying factor 2 is encoded by the SUMF2 gene, and catalyzes the oxidation of a specific cysteine to C $\alpha$ -formylglycine. It was observed to be located in the luminal space of the endoplasmic reticulum as soluble protein. Its function is rarely described, but it is suggested that SUMF2 regulates the activity of sulfatases and therefore contributes to posttranslational protein modifications(238–240). In general, very less is known about SUMF2 in cancer, and no publication exists concerning BC, so far. Its expression in cancer tissue remains to be nearly unstudied. One study described the analysis of single nucleotide variation in colorectal cancer tissue. Among others, they found SUMF2 as novel significantly mutated gene, and suggest it might be a functional mutation in colorectal cancer(241). Since there is no evidence for SUMF2 expression or function in cancer so far, the data detected in this study

demonstrate an association of an elevated SUMF2 protein and mRNA expression in the *in vitro* 3D model of the invasive T24/83 BC cell line, compared to the 2D model, and further the correlation of an increased SUMF2 expression with tumor progression and worse prognosis on mRNA level in MIBC patients for the first time.

Altogether, the 10 identified ECM-related targets appeared with raised protein and mRNA levels in the 3D *in vitro* model, compared to the 2D one, of the invasive T24/83 BC cell line. Furthermore, an increased mRNA expression was linked to tumor progression and poor prognosis in MIBC patients of the TCGA cohort. In addition, except for DPYSL3 with regard to OS, they were identified as independent prognostic marker concerning OS and DFS, among the most expressive progression factors for BC, as T-stage and pN-stage. Since no molecular BC tissue marker is currently implemented to the clinic, T-stage and pN-stage are the most significant clinicopathological units for disease evaluation. Interestingly, these targets are promising biomolecules for either MIBC prognosis or future therapy concepts. Although, some of the targets were not described for BC previously (LAMC1, CALU, DPYSL3, P4HA2, SUMF2) but share remarkable features with respect to muscle-invasive behavior as described for other entities, except for SUMF2. Based on this study and previous data, properties as migration, invasion, metastasis, and EMT were associated with most of the identified targets here (LAMC1, FBN1, CALU, CD109, DPYSL3, LRP1, P4HA2), indicating their potential role in MIBC development and invasive progression. In addition, increased expression of the targets FBN1, PLOD1, LRP1, and P4HA2 were determined as hypoxia-induced, indicating *in vivo*-like properties of the 3D *in vitro* model. According to literature, the better expression of stem-like properties of the 3D model was demonstrated through increased collagen expression and deposition, leading to ECM stiffness, as indicated by the elevated expression of FBN1, P4HA2, and CD109. Furthermore, CD109 and LRP1 expression are linked to drug resistance in malignant diseases. This study offers new muscle-invasive associated targets for BC, a better expression of invasive and *in vivo*-like properties *in vitro*, stem-like properties and drug resistance-related targets, indicating the use of the T24/83 3D model as useful tool in translational MIBC research, as well as the identified targets as novel drugs and biomarker.

#### 5.4.3 Advances and limitations of the study

The application of the 3D *in vitro* model of the invasive T24/83 BC cell line expressed malignant characteristics, as EMT and stem-like properties, more abundant compared to the 2D model. Also the CM condition turned out to express invasive characteristics more dominant in contrast to the UCM condition, so that the malignancy of the T24/83 cell line is dependent on the cellular 3D arrangement and ECM enrichment. It was aimed and realized to develop a less complex, easy to use and cost effective model. This might bring limitations in its translational nature, thus it is based on a mono culture without other stroma cells, and the ECM is probably enough

to form and grow of spheroids but less complex and dynamic compared to *in vivo* conditions, while less invasive characteristics might be expressed in the 3D T24/83 *in vitro* model. To characterize the findings of the invasive 3D *in vitro* model, gene expressions were validated by mRNA expression, and clinical data of the TCGA MIBC cohort. These data are real world data derived from patients which are already collected and analyzed, public available, and ethically safe. In case of MIBC, this cohort also possesses a statistically valid number of subjects. Nevertheless, due to its retrospective characteristics, there is a lack of subject control and data generation, as well as a higher tendency for bias, which leads to more prone to errors.



## 6 CONCLUSION & OUTLOOK

The treatment and prognosis of MIBC patients is still limited due to few therapeutic advance and incomplete molecular tumor classification. The ECM has a distinct impact on MIBC onset, and offers a promising platform for future investigations of valid biomarker and new treatment strategies, however its particular function and characteristics during MIBC is not completely understood.

3D *in vitro* models are able to mimic *in vivo* conditions better as oversimplified 2D conditions. However, their use is still no standard procedure for translational BC research, and its application is highly dependent on the cell line, 3D model, and medium conditions. Therefore, it is indispensable to figure out the cell lines special needs. On the other hand, the development of an easy applicable, cost effective, and flexible model is desired. The here established Matrigel-free 3D *in vitro* model of the invasive T24/83 BC cell line, turned out to express ECM-related invasive properties more abundant, in comparison to the culture in 2D. Its association to EMT and ESC processes was significantly increased and revealed 10 ECM-related targets (LAMC1, FBN1, PLOD1, CALU, CD109, DPYSL3, LRP1, HTRA1, P4HA2, SUMF2). Some of them had also been proven to be highly influential in MIBC patients (FBN1, PLOD1, CD109, LRP1, HTRA1), while others (LAMC1, CALU, DPYSL3, P4HA2, SUMF2) were associated to MIBC for the first time. The 3D model of T24/83 offers new muscle-invasive associated targets for BC, a better expression of invasive and *in vivo*-like properties *in vitro*, stem-like properties and drug resistance-related targets to study invasive BC mechanisms and treatment options for future projects. Furthermore, follow up the 10 identified ECM-related targets could lead to promising molecular biomarker or future therapeutic targets, which is urgent to improve personalized stratification, and therapy for MIBC patients.

## 7 REFERENCES

1. Saginala K, Barsouk A, Aluru JS, Rawla P, Padala SA, Barsouk A. Epidemiology of Bladder Cancer. *Med Sci Basel Switz.* 2020 Mar 13;8(1):1–12.
2. Richters A, Aben KKH, Kiemeny LALM. The global burden of urinary bladder cancer: an update. *World J Urol.* 2020 Aug 1;38(8):1895–904.
3. Mostafa MH, Sheweita SA, O'Connor PJ. Relationship between schistosomiasis and bladder cancer. *Clin Microbiol Rev.* 1999 Jan;12(1):97–111.
4. Humphrey PA, Moch H, Cubilla AL, Ulbright TM, Reuter VE. The 2016 WHO Classification of Tumours of the Urinary System and Male Genital Organs-Part B: Prostate and Bladder Tumours. *Eur Urol.* 2016 Jul;70(1):106–19.
5. Steinberg GD, Trump DL, Cummings KB. Metastatic bladder cancer. Natural history, clinical course, and consideration for treatment. *Urol Clin North Am.* 1992 Nov;19(4):735–46.
6. Liebert M, Seigne J. Characteristics of invasive bladder cancers: histological and molecular markers. *Semin Urol Oncol.* 1996 May;14(2):62–72.
7. Shah JB, McConkey DJ, Dinney CPN. New strategies in muscle-invasive bladder cancer: on the road to personalized medicine. *Clin Cancer Res Off J Am Assoc Cancer Res.* 2011 May 1;17(9):2608–12.
8. Svatek RS, Hollenbeck BK, Holmäng S, Lee R, Kim SP, Stenzl A, et al. The economics of bladder cancer: costs and considerations of caring for this disease. *Eur Urol.* 2014 Aug;66(2):253–62.
9. Inamura K. Bladder Cancer: New Insights into Its Molecular Pathology. *Cancers.* 2018 Apr 1;10(4):1–14.
10. Smolensky D, Rathore K, Cekanova M. Molecular targets in urothelial cancer: detection, treatment, and animal models of bladder cancer. *Drug Des Devel Ther.* 2016 Oct 5;10:3305–22.
11. Sapre N, Herle P, Anderson PD, Corcoran NM, Hovens CM. Molecular biomarkers for predicting outcomes in urothelial carcinoma of the bladder. *Pathology (Phila).* 2014 Jun;46(4):274–82.
12. Aitken KJ, Bāgli DJ. The bladder extracellular matrix. Part I: architecture, development and disease. *Nat Rev Urol.* 2009 Nov;6(11):596–611.
13. Bissell MJ, Hall HG, Parry G. How does the extracellular matrix direct gene expression? *J Theor Biol.* 1982 Nov 7;99(1):31–68.
14. Hynes RO, Naba A. Overview of the matrisome--an inventory of extracellular matrix constituents and functions. *Cold Spring Harb Perspect Biol.* 2012 Jan 1;4(1):a004903.
15. Alfano M, Canducci F, Nebuloni M, Clementi M, Montorsi F, Salonia A. The interplay of extracellular matrix and microbiome in urothelial bladder cancer. *Nat Rev Urol.* 2016;13(2):77–90.

16. Humphrey JD, Dufresne ER, Schwartz MA. Mechanotransduction and extracellular matrix homeostasis. *Nat Rev Mol Cell Biol.* 2014 Dec;15(12):802–12.
17. Aitken KJ, Block G, Lorenzo A, Herz D, Sabha N, Dessouki O, et al. Mechanotransduction of extracellular signal-regulated kinases 1 and 2 mitogen-activated protein kinase activity in smooth muscle is dependent on the extracellular matrix and regulated by matrix metalloproteinases. *Am J Pathol.* 2006 Aug;169(2):459–70.
18. Longhurst PA, Eika B, Leggett RE, Levin RM. Urinary bladder function in the tight-skin mouse. *J Urol.* 1992 Nov;148(5):1611–4.
19. Liapis A, Bakas P, Pafiti A, Hassiakos D, Frangos-Plemenos M, Creatsas G. Changes in the quantity of collagen type I in women with genuine stress incontinence. *Urol Res.* 2000 Oct;28(5):323–6.
20. Hojilla CV, Mohammed FF, Khokha R. Matrix metalloproteinases and their tissue inhibitors direct cell fate during cancer development. *Br J Cancer.* 2003 Nov 17;89(10):1817–21.
21. Egeblad M, Werb Z. New functions for the matrix metalloproteinases in cancer progression. *Nat Rev Cancer.* 2002 Mar;2(3):161–74.
22. Zhang H, Shan G, Song J, Tian Y, An L-Y, Ban Y, et al. Extracellular matrix-related genes play an important role in the progression of NMIBC to MIBC: a bioinformatics analysis study. *Biosci Rep.* 2020 May 29;40(5):1–12.
23. Zhu H, Chen H, Wang J, Zhou L, Liu S. Collagen stiffness promoted non-muscle-invasive bladder cancer progression to muscle-invasive bladder cancer. *OncoTargets Ther.* 2019;12:3441–57.
24. Zhang G, Miyake M, Lawton A, Goodison S, Rosser CJ. Matrix metalloproteinase-10 promotes tumor progression through regulation of angiogenic and apoptotic pathways in cervical tumors. *BMC Cancer.* 2014 May 3;14:310.
25. Szarvas T, Becker M, vom Dorp F, Gethmann C, Tötsch M, Bánkfalvi A, et al. Matrix metalloproteinase-7 as a marker of metastasis and predictor of poor survival in bladder cancer. *Cancer Sci.* 2010 May;101(5):1300–8.
26. Wallard MJ, Pennington CJ, Veerakumarasivam A, Burt G, Mills IG, Warren A, et al. Comprehensive profiling and localisation of the matrix metalloproteinases in urothelial carcinoma. *Br J Cancer.* 2006 Feb 27;94(4):569–77.
27. Kanayama H, Yokota K, Kurokawa Y, Murakami Y, Nishitani M, Kagawa S. Prognostic values of matrix metalloproteinase-2 and tissue inhibitor of metalloproteinase-2 expression in bladder cancer. *Cancer.* 1998 Apr 1;82(7):1359–66.
28. Szarvas T, vom Dorp F, Ergün S, Rübber H. Matrix metalloproteinases and their clinical relevance in urinary bladder cancer. *Nat Rev Urol.* 2011 May;8(5):241–54.
29. Zhao H, Chen Q, Alam A, Cui J, Suen KC, Soo AP, et al. The role of osteopontin in the progression of solid organ tumour. *Cell Death Dis.* 2018 Mar 2;9(3):356.
30. Hussain SA, Palmer DH, Syn W-K, Sacco JJ, Greensmith RMD, Elmetwali T, et al. Gene expression profiling in bladder cancer identifies potential therapeutic targets. *Int J Oncol.* 2017 Apr;50(4):1147–59.

31. Wong JPC, Wei R, Lyu P, Tong OLH, Zhang SD, Wen Q, et al. Clinical and in vitro analysis of Osteopontin as a prognostic indicator and unveil its potential downstream targets in bladder cancer. *Int J Biol Sci.* 2017;13(11):1373–86.
32. Ahmed M, Sottnik JL, Dancik GM, Sahu D, Hansel DE, Theodorescu D, et al. An Osteopontin/CD44 Axis in RhoGDI2-Mediated Metastasis Suppression. *Cancer Cell.* 2016 Sep 12;30(3):432–43.
33. Zhang N, Li F, Gao J, Zhang S, Wang Q. Osteopontin accelerates the development and metastasis of bladder cancer via activating JAK1/STAT1 pathway. *Genes Genomics.* 2020 Apr;42(4):467–75.
34. Gao F, Xu T, Wang X, Zhong S, Chen S, Zhang M, et al. CIP2A mediates fibronectin-induced bladder cancer cell proliferation by stabilizing  $\beta$ -catenin. *J Exp Clin Cancer Res CR.* 2017 May 18;36(1):70.
35. Zhou X, Zhai Y, Liu C, Yang G, Guo J, Li G, et al. Sialidase NEU1 suppresses progression of human bladder cancer cells by inhibiting fibronectin-integrin  $\alpha 5\beta 1$  interaction and Akt signaling pathway. *Cell Commun Signal CCS.* 2020 Mar 12;18(1):44.
36. Giblin SP, Midwood KS. Tenascin-C: Form versus function. *Cell Adhes Migr.* 2014 Dec 6;9(1–2):48–82.
37. Richter P, Tost M, Franz M, Altendorf-Hofmann A, Junker K, Borsi L, et al. B and C domain containing tenascin-C: urinary markers for invasiveness of urothelial carcinoma of the urinary bladder? *J Cancer Res Clin Oncol.* 2009 Oct;135(10):1351–8.
38. Gecks T, Junker K, Franz M, Richter P, Walther M, Voigt A, et al. B domain containing Tenascin-C: a new urine marker for surveillance of patients with urothelial carcinoma of the urinary bladder? *Clin Chim Acta Int J Clin Chem.* 2011 Oct 9;412(21–22):1931–6.
39. Bosman FT, Stamenkovic I. Functional structure and composition of the extracellular matrix. *J Pathol.* 2003 Jul;200(4):423–8.
40. Engbring JA, Kleinman HK. The basement membrane matrix in malignancy. *J Pathol.* 2003 Jul;200(4):465–70.
41. Pradhan D, Amin M, Hooda S, Dhir R, Bastacky S, Parwani AV. Utility of the laminin immunohistochemical stain in distinguishing invasive from noninvasive urothelial carcinoma. *J Cancer Res Ther.* 2017 Dec;13(6):947–50.
42. Kang S-G, Ha Y-R, Ko Y-H, Kang S-H, Joo K-J, Cho H-Y, et al. Effect of laminin 332 on motility and invasion in bladder cancer. *Kaohsiung J Med Sci.* 2013 Aug;29(8):422–9.
43. Tsubota Y, Ogawa T, Oyanagi J, Nagashima Y, Miyazaki K. Expression of laminin gamma2 chain monomer enhances invasive growth of human carcinoma cells in vivo. *Int J Cancer.* 2010 Nov 1;127(9):2031–41.
44. Hubschmid U, Leong-Morgenthaler P-M, Basset-Dardare A, Ruault S, Frey P. In vitro growth of human urinary tract smooth muscle cells on laminin and collagen type I-coated membranes under static and dynamic conditions. *Tissue Eng.* 2005 Feb;11(1–2):161–71.
45. Li T, Wu C, Gao L, Qin F, Wei Q, Yuan J. Lysyl oxidase family members in urological tumorigenesis and fibrosis. *Oncotarget.* 2018 Apr 13;9(28):20156–64.

46. Li W-M, Chan T-C, Huang SK-H, Wu W-J, Ke H-L, Liang P-I, et al. Prognostic Utility of FBLN2 Expression in Patients With Urothelial Carcinoma. *Front Oncol.* 2020;10:570340.
47. Azevedo R, Peixoto A, Gaiteiro C, Fernandes E, Neves M, Lima L, et al. Over forty years of bladder cancer glycobiology: Where do glycans stand facing precision oncology? *Oncotarget.* 2017 Jul 21;8(53):91734–64.
48. Niedworok C, Röck K, Kretschmer I, Freudenberger T, Nagy N, Szarvas T, et al. Inhibitory Role of the Small Leucine-Rich Proteoglycan Biglycan in Bladder Cancer. *PLoS ONE.* 2013 Nov 6;8(11):1-13.e80084.
49. Sainio A, Nyman M, Lund R, Vuorikoski S, Boström P, Laato M, et al. Lack of Decorin Expression by Human Bladder Cancer Cells Offers New Tools in the Therapy of Urothelial Malignancies. *PLoS ONE.* 2013 Oct 11;8(10):1-8.e76190.
50. Zhang Q, Wu J, Chen X, Zhao M, Zhang D, Gao F. Upregulation of Versican Associated with Tumor Progression, Metastasis, and Poor Prognosis in Bladder Carcinoma. *BioMed Res Int.* 2021;2021:6949864.
51. Wullweber A, Strick R, Lange F, Sikic D, Taubert H, Wach S, et al. Bladder tumor subtype commitment occurs in carcinoma in-situ driven by key signaling pathways including ECM remodeling. *Cancer Res.* 2021 Jan 20;81(6):1552–66.
52. Ghasemi H, Mousavibahar SH, Hashemnia M, Karimi J, Khodadadi I, Mirzaei F, et al. Tissue stiffness contributes to YAP activation in bladder cancer patients undergoing transurethral resection. *Ann N Y Acad Sci.* 2020 Aug;1473(1):48–61.
53. Ringuette-Goulet C, Bolduc S, Pouliot F. Modeling human bladder cancer. *World J Urol.* 2018 Nov;36(11):1759–66.
54. Mayorca-Guilliani AE, Willacy O, Madsen CD, Rafaeva M, Elisabeth Heumüller S, Bock F, et al. Decellularization and antibody staining of mouse tissues to map native extracellular matrix structures in 3D. *Nat Protoc.* 2019 Dec;14(12):3395–425.
55. Fujiyama C, Jones A, Fuggle S, Bicknell R, Cranston D, Harris AL. Human bladder cancer invasion model using rat bladder in vitro and its use to test mechanisms and therapeutic inhibitors of invasion. *Br J Cancer.* 2001 Feb;84(4):558–64.
56. Burgués JP, Gómez L, Pontones JL, Vera CD, Jiménez-Cruz JF, Ozonias M. A chemosensitivity test for superficial bladder cancer based on three-dimensional culture of tumour spheroids. *Eur Urol.* 2007 Apr;51(4):962–9; discussion 969-970.
57. Lee SH, Hu W, Matulay JT, Silva MV, Owczarek TB, Kim K, et al. Tumor Evolution and Drug Response in Patient-Derived Organoid Models of Bladder Cancer. *Cell.* 2018 Apr 5;173(2):515-528.e17.
58. Kim MJ, Chi BH, Yoo JJ, Ju YM, Whang YM, Chang IH. Structure establishment of three-dimensional (3D) cell culture printing model for bladder cancer. *PloS One.* 2019;14(10):e0223689.
59. Kim MJ, Chi BH, Yoo JJ, Ju YM, Whang YM, Chang IH. Structure establishment of three-dimensional (3D) cell culture printing model for bladder cancer. *PLOS ONE.* 2019 Oct 22;14(10):e0223689.
60. Miermont A, Lee SWL, Adriani G, Kamm RD. Quantitative screening of the effects of hyper-osmotic stress on cancer cells cultured in 2- or 3-dimensional settings. *Sci Rep.* 2019 Sep 24;9(1):13782.

61. Shi H, Jiang H, Wang L, Cao Y, Liu P, Xu X, et al. Overexpression of monocarboxylate anion transporter 1 and 4 in T24-induced cancer-associated fibroblasts regulates the progression of bladder cancer cells in a 3D microfluidic device. *Cell Cycle Georget Tex.* 2015;14(19):3058–65.
62. Ringuette Goulet C, Bernard G, Chabaud S, Couture A, Langlois A, Neveu B, et al. Tissue-engineered human 3D model of bladder cancer for invasion study and drug discovery. *Biomaterials.* 2017 Nov;145:233–41.
63. Rodrigues J, Heinrich MA, Teixeira LM, Prakash J. 3D In Vitro Model (R)evolution: Unveiling Tumor–Stroma Interactions. *Trends Cancer.* 2020 Nov 17;0(0):1–16.
64. Vasyutin I, Zerihun L, Ivan C, Atala A. Bladder Organoids and Spheroids: Potential Tools for Normal and Diseased Tissue Modelling. *Anticancer Res.* 2019 Mar 1;39(3):1105–18.
65. Vandepitte J, Roelants M, Van Cleynenbreugel B, Hettinger K, Lerut E, Van Poppel H, et al. Biodistribution and photodynamic effects of polyvinylpyrrolidone-hypericin using multicellular spheroids composed of normal human urothelial and T24 transitional cell carcinoma cells. *J Biomed Opt.* 2011 Feb;16(1):018001.
66. Su G, Zhao Y, Wei J, Han J, Chen L, Xiao Z, et al. The effect of forced growth of cells into 3D spheres using low attachment surfaces on the acquisition of stemness properties. *Biomaterials.* 2013 Apr 1;34(13):3215–22.
67. Amaral RLF, Miranda M, Marcato PD, Swiech K. Comparative Analysis of 3D Bladder Tumor Spheroids Obtained by Forced Floating and Hanging Drop Methods for Drug Screening. *Front Physiol.* 2017;8:605.
68. Sant S, Johnston PA. The Production of 3D Tumor Spheroids for Cancer Drug Discovery. *Drug Discov Today Technol.* 2017 Mar;23:27–36.
69. Yoshida T, Sopko NA, Kates M, Liu X, Joice G, Mcconkey DJ, et al. Impact of spheroid culture on molecular and functional characteristics of bladder cancer cell lines. *Oncol Lett.* 2019 Nov;18(5):4923–9.
70. Wang Y, Day ML, Simeone DM, Palmbos PL. 3-D Cell Culture System for Studying Invasion and Evaluating Therapeutics in Bladder Cancer. *J Vis Exp JoVE.* 2018 Sep 13;(139):1-10.e58345.
71. Vinci M, Gowan S, Boxall F, Patterson L, Zimmermann M, Court W, et al. Advances in establishment and analysis of three-dimensional tumor spheroid-based functional assays for target validation and drug evaluation. *BMC Biol.* 2012 Mar 22;10:29.
72. Petzoldt JL, Leigh IM, Duffy PG, Sexton C, Masters JR. Immortalisation of human urothelial cells. *Urol Res.* 1995;23(6):377–80.
73. Rigby CC, Franks LM. A human tissue culture cell line from a transitional cell tumour of the urinary bladder: growth, chromosome pattern and ultrastructure. *Br J Cancer.* 1970 Dec;24(4):746–54.
74. Bubeník J, Barešová M, Viklický V, Jakoubková J, Sainerová H, Donner J. Established cell line of urinary bladder carcinoma (T24) containing tumour-specific antigen. *Int J Cancer.* 1973 May 15;11(3):765–73.
75. O'Toole C, Nayak S, Price Z, Gilbert WH, Waisman J. A cell line (SCABER) derived from squamous cell carcinoma of the human urinary bladder. *Int J Cancer.* 1976 Jun 15;17(6):707–14.

76. Grossman HB, Wedemeyer G, Ren L, Wilson GN, Cox B. Improved growth of human urothelial carcinoma cell cultures. *J Urol*. 1986 Oct;136(4):953–9.
77. Masters JR, Hepburn PJ, Walker L, Highman WJ, Trejdosiewicz LK, Povey S, et al. Tissue culture model of transitional cell carcinoma: characterization of twenty-two human urothelial cell lines. *Cancer Res*. 1986 Jul;46(7):3630–6.
78. Marshall CJ, Franks LM, Carbonell AW. Markers of Neoplastic Transformation in Epithelial Cell Lines Derived From Human Carcinomas. *J Natl Cancer Inst*. 1977 Jan 6;58(6):1743–51.
79. Chen W, Wong C, Vosburgh E, Levine AJ, Foran DJ, Xu EY. High-throughput Image Analysis of Tumor Spheroids: A User-friendly Software Application to Measure the Size of Spheroids Automatically and Accurately. *J Vis Exp JoVE*. 2014 Jul 8;(89):1-10.e51639.
80. Nürnberg E, Vitacolonna M, Klicks J, von Molitor E, Cesetti T, Keller F, et al. Routine Optical Clearing of 3D-Cell Cultures: Simplicity Forward. *Front Mol Biosci*. 2020;7:20.
81. Hughes CS, Moggridge S, Müller T, Sorensen PH, Morin GB, Krijgsveld J. Single-pot, solid-phase-enhanced sample preparation for proteomics experiments. *Nat Protoc*. 2019;14(1):68–85.
82. Cox J, Mann M. MaxQuant enables high peptide identification rates, individualized p.p.b.-range mass accuracies and proteome-wide protein quantification. *Nat Biotechnol*. 2008 Dec;26(12):1367–72.
83. Cox J, Neuhauser N, Michalski A, Scheltema RA, Olsen JV, Mann M. Andromeda: a peptide search engine integrated into the MaxQuant environment. *J Proteome Res*. 2011 Apr 1;10(4):1794–805.
84. R Core Team. R: A language and environment for statistical computing. R Foundation for Statistical Computing [Internet]. Vienna, Austria; 2017. Available from: <https://www.R-project.org/>
85. Tyanova S, Temu T, Sinitcyn P, Carlson A, Hein MY, Geiger T, et al. The Perseus computational platform for comprehensive analysis of (prote)omics data. *Nat Methods*. 2016;13(9):731–40.
86. Ritchie ME, Phipson B, Wu D, Hu Y, Law CW, Shi W, et al. limma powers differential expression analyses for RNA-sequencing and microarray studies. *Nucleic Acids Res*. 2015 Apr 20;43(7):e47.
87. Benjamini Y, Hochberg Y. Controlling the False Discovery Rate: A Practical and Powerful Approach to Multiple Testing. *J R Stat Soc Ser B Methodol*. 1995;57(1):289–300.
88. Sergushichev AA. An algorithm for fast preranked gene set enrichment analysis using cumulative statistic calculation. *bioRxiv*. 2016 Jun 20;1–9.
89. RStudio Team. RStudio: Integrated Development for R [Internet]. Boston, MA; 2015. Available from: <http://www.rstudio.com/>
90. Dai M, Wang P, Boyd AD, Kostov G, Athey B, Jones EG, et al. Evolving gene/transcript definitions significantly alter the interpretation of GeneChip data. *Nucleic Acids Res*. 2005 Nov 10;33(20):e175.

91. Robertson AG, Kim J, Al-Ahmadie H, Bellmunt J, Guo G, Cherniack AD, et al. Comprehensive Molecular Characterization of Muscle-Invasive Bladder Cancer. *Cell*. 2017 Oct 19;171(3):540-556.e25.
92. Reiner A, Yekutieli D, Benjamini Y. Identifying differentially expressed genes using false discovery rate controlling procedures. *Bioinforma Oxf Engl*. 2003 Feb 12;19(3):368–75.
93. Anaka M, Freyer C, Gedye C, Caballero O, Davis ID, Behren A, et al. Stem cell media culture of melanoma results in the induction of a nonrepresentative neural expression profile. *Stem Cells Dayt Ohio*. 2012 Feb;30(2):336–43.
94. Pirsko V, Cakstina I, Priedite M, Dortane R, Feldmane L, Nakazawa-Miklasevica M, et al. An Effect of Culture Media on Epithelial Differentiation Markers in Breast Cancer Cell Lines MCF7, MDA-MB-436 and SkBr3. *Med Kaunas Lith*. 2018 Mar 30;54(2).
95. Chihanga T, Hausmann SM, Ni S, Kennedy MA. Influence of media selection on NMR based metabolic profiling of human cell lines. *Metabolomics Off J Metabolomic Soc*. 2018 Jan 31;14(3):28.
96. Huang Z, Shao W, Gu J, Hu X, Shi Y, Xu W, et al. Effects of culture media on metabolic profiling of the human gastric cancer cell line SGC7901. *Mol Biosyst*. 2015 Jul;11(7):1832–40.
97. Elliott RL, Jiang X-P. The adverse effect of gentamicin on cell metabolism in three cultured mammary cell lines: “Are cell culture data skewed?” *PLoS One*. 2019;14(4):e0214586.
98. Iorio F, Knijnenburg TA, Vis DJ, Bignell GR, Menden MP, Schubert M, et al. A Landscape of Pharmacogenomic Interactions in Cancer. *Cell*. 2016 Jul 28;166(3):740–54.
99. Barretina J, Caponigro G, Stransky N, Venkatesan K, Margolin AA, Kim S, et al. The Cancer Cell Line Encyclopedia enables predictive modelling of anticancer drug sensitivity. *Nature*. 2012 Mar;483(7391):603–7.
100. Jensen C, Teng Y. Is It Time to Start Transitioning From 2D to 3D Cell Culture? *Front Mol Biosci*. 2020 Mar 6;7:1–15.
101. Wasén C, Ekstrand M, Levin M, Giglio D. Epidermal growth factor receptor function in the human urothelium. *Int Urol Nephrol*. 2018;50(4):647–56.
102. Merrill NM, Vandecan NM, Day KC, Palmboos PL, Day ML, Udager AM, et al. MEK is a promising target in the basal subtype of bladder cancer. *Oncotarget*. 2020 Nov 3;11(44):3921–32.
103. Zhuo Z, Song Z, Ma Z, Zhang Y, Xu G, Chen G. Chlorophyllin e6-mediated photodynamic therapy inhibits proliferation and induces apoptosis in human bladder cancer cells. *Oncol Rep*. 2019 Apr;41(4):2181–93.
104. Bodgi L, Bahmad HF, Araj T, Al Choboq J, Bou-Gharios J, Cheaito K, et al. Assessing Radiosensitivity of Bladder Cancer in vitro: A 2D vs. 3D Approach. *Front Oncol*. 2019;9:153.
105. Kim CJ, Terado T, Tambe Y, Mukaisho K-I, Sugihara H, Kawauchi A, et al. Anti-oncogenic activities of cyclin D1b siRNA on human bladder cancer cells via induction of apoptosis and suppression of cancer cell stemness and invasiveness. *Int J Oncol*. 2018 Jan 1;52(1):231–40.



106. Drost J, Clevers H. Organoids in cancer research. *Nat Rev Cancer*. 2018 Jul;18(7):407–18.
107. Peng D, Ge G, Gong Y, Zhan Y, He S, Guan B, et al. Vitamin C increases 5-hydroxymethylcytosine level and inhibits the growth of bladder cancer. *Clin Epigenetics*. 2018 Jul 13;10:1–13.
108. Cameron E, Pauling L, Leibovitz B. Ascorbic acid and cancer: a review. *Cancer Res*. 1979 Mar;39(3):663–81.
109. Reese DH, Friedman RD, Sporn MB. Induction of hyperplasia and its suppression by hydrocortisone in organ-cultured rat urinary bladder. *Cancer Res*. 1977 May;37(5):1421–7.
110. Knowles MA, Finesilver A, Harvey AE, Berry RJ, Hicks RM. Long-term organ culture of normal human bladder. *Cancer Res*. 1983 Jan;43(1):374–85.
111. Stinson SF, Lilga JC, Reese DH, Friedman RD, Sporn MB. Quantitation with an automated image analyzer of nuclearcytoplasmic changes induced by hydrocortisone in bladder epithelium. *Cancer Res*. 1977 May;37(5):1428–31.
112. Kim H, Lee SJ, Lee IK, Min SC, Sung HH, Jeong BC, et al. Synergistic Effects of Combination Therapy with AKT and mTOR Inhibitors on Bladder Cancer Cells. *Int J Mol Sci*. 2020 Apr 18;21(8):1–12.
113. Yang Y, Xu H, Shen J, Yang Y, Wu S, Xiao J, et al. RGD-modified oncolytic adenovirus exhibited potent cytotoxic effect on CAR-negative bladder cancer-initiating cells. *Cell Death Dis*. 2015 May;6(5):e1760.
114. Knopp JL, Holder-Pearson L, Chase JG. Insulin Units and Conversion Factors: A Story of Truth, Boots, and Faster Half-Truths. *J Diabetes Sci Technol*. 2018 Oct 13;13(3):597–600.
115. Liu S, Li Y, Lin T, Fan X, Liang Y, Heemann U. High dose human insulin and insulin glargine promote T24 bladder cancer cell proliferation via PI3K-independent activation of Akt. *Diabetes Res Clin Pract*. 2011 Feb;91(2):177–82.
116. Inoue K, Perrotte P, Wood CG, Slaton JW, Sweeney P, Dinney CPN. Gene Therapy of Human Bladder Cancer with Adenovirus-mediated Antisense Basic Fibroblast Growth Factor. *Clin Cancer Res*. 2000 Nov 1;6(11):4422–31.
117. Chikazawa M, Inoue K, Fukata S, Karashima T, Shuin T. Expression of angiogenesis-related genes regulates different steps in the process of tumor growth and metastasis in human urothelial cell carcinoma of the urinary bladder. *Pathobiol J Immunopathol Mol Cell Biol*. 2008;75(6):335–45.
118. Miyake H, Yoshimura K, Hara I, Eto H, Arakawa S, Kamidono S. Basic fibroblast growth factor regulates matrix metalloproteinases production and in vitro invasiveness in human bladder cancer cell lines. *J Urol*. 1997 Jun;157(6):2351–5.
119. Dinney CP, Bielenberg DR, Perrotte P, Reich R, Eve BY, Bucana CD, et al. Inhibition of basic fibroblast growth factor expression, angiogenesis, and growth of human bladder carcinoma in mice by systemic interferon-alpha administration. *Cancer Res*. 1998 Feb 15;58(4):808–14.

120. Yang B, Zhou L, Peng B, Sun Z, Dai Y, Zheng J. In vitro comparative evaluation of recombinant growth factors for tissue engineering of bladder in patients with neurogenic bladder. *J Surg Res.* 2014 Jan;186(1):63–72.
121. Kalluri R. The biology and function of fibroblasts in cancer. *Nat Rev Cancer.* 2016 Aug 23;16(9):582–98.
122. Kashpur O, LaPointe D, Ambady S, Ryder EF, Dominko T. FGF2-induced effects on transcriptome associated with regeneration competence in adult human fibroblasts. *BMC Genomics.* 2013 Sep 26;14:656.
123. Chen W, Shi C, Hou X, Zhang W, Li L. Bladder acellular matrix conjugated with basic fibroblast growth factor for bladder regeneration. *Tissue Eng Part A.* 2014 Aug;20(15–16):2234–42.
124. Shi C, Chen W, Chen B, Shan T, Jia W, Hou X, et al. Bladder regeneration in a canine model using a bladder acellular matrix loaded with a collagen-binding bFGF. *Biomater Sci.* 2017 Nov 21;5(12):2427–36.
125. Monaco S, Illario M, Rusciano MR, Gragnaniello G, Di Spigna G, Leggiero E, et al. Insulin stimulates fibroblast proliferation through calcium-calmodulin-dependent kinase II. *Cell Cycle Georget Tex.* 2009 Jul 1;8(13):2024–30.
126. Warnken M, Reitzenstein U, Sommer A, Fuhrmann M, Mayer P, Enzmann H, et al. Characterization of proliferative effects of insulin, insulin analogues and insulin-like growth factor-1 (IGF-1) in human lung fibroblasts. *Naunyn Schmiedebergs Arch Pharmacol.* 2010 Dec;382(5–6):511–24.
127. Russell JD, Russell SB, Trupin KM. Differential effects of hydrocortisone on both growth and collagen metabolism of human fibroblasts from normal and keloid tissue. *J Cell Physiol.* 1978 Nov;97(2):221–9.
128. Cury PR, Araújo VC, Canavez F, Furuse C, Araújo NS. Hydrocortisone affects the expression of matrix metalloproteinases (MMP-1, -2, -3, -7, and -11) and tissue inhibitor of matrix metalloproteinases (TIMP-1) in human gingival fibroblasts. *J Periodontol.* 2007 Jul;78(7):1309–15.
129. Luca AC, Mersch S, Deenen R, Schmidt S, Messner I, Schäfer K-L, et al. Impact of the 3D Microenvironment on Phenotype, Gene Expression, and EGFR Inhibition of Colorectal Cancer Cell Lines. *PLoS ONE.* 2013 Mar 26;8(3):1-11.e59689.
130. Bhattacharya S, Calar K, de la Puente P. Mimicking tumor hypoxia and tumor-immune interactions employing three-dimensional in vitro models. *J Exp Clin Cancer Res CR.* 2020 May 1;39(1):75.
131. Coelho R, Marcos-Silva L, Mendes N, Pereira D, Brito C, Jacob F, et al. Mucins and Truncated O-Glycans Unveil Phenotypic Discrepancies between Serous Ovarian Cancer Cell Lines and Primary Tumours. *Int J Mol Sci.* 2018 Jul 13;19(7).
132. Balmaña M, Mereiter S, Diniz F, Feijão T, Barrias CC, Reis CA. Multicellular Human Gastric-Cancer Spheroids Mimic the Glycosylation Phenotype of Gastric Carcinomas. *Mol Basel Switz.* 2018 Oct 30;23(11).
133. Aumailley M. The laminin family. *Cell Adhes Migr.* 2013 Feb;7(1):48–55.
134. Boyrie S, Delmas C, Lemarié A, Lubrano V, Dahan P, Malric L, et al. RND1 regulates migration of human glioblastoma stem-like cells according to their anatomical localization

- and defines a prognostic signature in glioblastoma. *Oncotarget*. 2018 Sep 18;9(73):33788–803.
135. Fowler A, Thomson D, Giles K, Maleki S, Mreich E, Wheeler H, et al. miR-124a is frequently down-regulated in glioblastoma and is involved in migration and invasion. *Eur J Cancer Oxf Engl 1990*. 2011 Apr;47(6):953–63.
  136. Huang S-X, Zhao Z-Y, Weng G-H, He X-Y, Wu C-J, Fu C-Y, et al. The correlation of microRNA-181a and target genes with poor prognosis of glioblastoma patients. *Int J Oncol*. 2016 Jul;49(1):217–24.
  137. Kunitomi H, Kobayashi Y, Wu RC, Takeda T, Tominaga E, Banno K, et al. LAMC1 is a prognostic factor and a potential therapeutic target in endometrial cancer. *J Gynecol Oncol*. 2020 Mar;31(2):e11.
  138. Kashima H, Wu R-C, Wang Y, Sinno AK, Miyamoto T, Shiozawa T, et al. Laminin C1 expression by uterine carcinoma cells is associated with tumor progression. *Gynecol Oncol*. 2015 Nov;139(2):338–44.
  139. Zacapala-Gómez AE, C Alarcón-Romero LD, Mendoza-Catalán MA, Salmerón-Bárcenas EG, I Zubillaga-Guerrero M, Torres-Rojas FI, et al. Integrin subunit  $\beta$ 1 and laminin  $\gamma$ 1 chain expression: a potential prognostic biomarker in cervical cancer. *Biomark Med*. 2020 Oct;14(15):1461–71.
  140. Nishikawa R, Goto Y, Kojima S, Enokida H, Chiyomaru T, Kinoshita T, et al. Tumor-suppressive microRNA-29s inhibit cancer cell migration and invasion via targeting LAMC1 in prostate cancer. *Int J Oncol*. 2014 Jul;45(1):401–10.
  141. Yang Z-P, Ma H-S, Wang S-S, Wang L, Liu T. LAMC1 mRNA promotes malignancy of hepatocellular carcinoma cells by competing for MicroRNA-124 binding with CD151. *IUBMB Life*. 2017 Aug;69(8):595–605.
  142. Zhang Y, Xi S, Chen J, Zhou D, Gao H, Zhou Z, et al. Overexpression of LAMC1 predicts poor prognosis and enhances tumor cell invasion and migration in hepatocellular carcinoma. *J Cancer*. 2017;8(15):2992–3000.
  143. Zu C, Liu T, Zhang G. MicroRNA-506 Inhibits Malignancy of Colorectal Carcinoma Cells by Targeting LAMC1. *Ann Clin Lab Sci*. 2016 Dec;46(6):666–74.
  144. Jensen SA, Handford PA. New insights into the structure, assembly and biological roles of 10–12 nm connective tissue microfibrils from fibrillin-1 studies. *Biochem J*. 2016 Mar 29;473(7):827–38.
  145. Sakai LY, Keene DR, Renard M, De Backer J. FBN1: The disease-causing gene for Marfan syndrome and other genetic disorders. *Gene*. 2016 Oct 10;591(1):279–91.
  146. Shi S, Tian B. Identification of biomarkers associated with progression and prognosis in bladder cancer via co-expression analysis. *Cancer Biomark Sect Dis Markers*. 2019;24(2):183–93.
  147. Shevchenko V, Arnotskaya N, Pak O, Sharma A, Sharma HS, Khotimchenko Y, et al. Molecular determinants of the interaction between glioblastoma CD133+ cancer stem cells and the extracellular matrix. *Int Rev Neurobiol*. 2020;151:155–69.
  148. Chen J, Wang X, Hu B, He Y, Qian X, Wang W. Candidate genes in gastric cancer identified by constructing a weighted gene co-expression network. *PeerJ*. 2018;6:e4692.

149. Li Y, Wang J-S, Zhang T, Wang H-C, Li L-P. Identification of New Therapeutic Targets for Gastric Cancer With Bioinformatics. *Front Genet.* 2020 Aug 18;11:1–17.
150. Tian Y, Xing Y, Zhang Z, Peng R, Zhang L, Sun Y. Bioinformatics Analysis of Key Genes and circRNA-miRNA-mRNA Regulatory Network in Gastric Cancer. *BioMed Res Int.* 2020;2020:2862701.
151. Yue H, Wang J, Chen R, Hou X, Li J, Lu X. Gene signature characteristic of elevated stromal infiltration and activation is associated with increased risk of hematogenous and lymphatic metastasis in serous ovarian cancer. *BMC Cancer.* 2019 Dec 30;19(1):1266.
152. Chen J, Cai Y, Xu R, Pan J, Zhou J, Mei J. Identification of four hub genes as promising biomarkers to evaluate the prognosis of ovarian cancer in silico. *Cancer Cell Int.* 2020;20:270.
153. Millstein J, Budden T, Goode EL, Anglesio MS, Talhouk A, Intermaggio MP, et al. Prognostic gene expression signature for high-grade serous ovarian cancer. *Ann Oncol Off J Eur Soc Med Oncol.* 2020 Sep;31(9):1240–50.
154. Chen S-C, Chen F-W, Hsu Y-L, Kuo P-L. Systematic Analysis of Transcriptomic Profile of Renal Cell Carcinoma under Long-Term Hypoxia Using Next-Generation Sequencing and Bioinformatics. *Int J Mol Sci.* 2017 Dec 7;18(12).
155. Luo S, Zou R, Wu J, Landry MP. A Probe for the Detection of Hypoxic Cancer Cells. *ACS Sens.* 2017 Aug 25;2(8):1139–45.
156. Liu W, Liu P, Gao H, Wang X, Yan M. Long non-coding RNA PGM5-AS1 promotes epithelial-mesenchymal transition, invasion and metastasis of osteosarcoma cells by impairing miR-140-5p-mediated FBN1 inhibition. *Mol Oncol.* 2020 Oct;14(10):2660–77.
157. Qi Y, Xu R. Roles of PLODs in Collagen Synthesis and Cancer Progression. *Front Cell Dev Biol.* 2018;6:66.
158. Yamada Y, Kato M, Arai T, Sanada H, Uchida A, Misono S, et al. Aberrantly expressed PLOD1 promotes cancer aggressiveness in bladder cancer: a potential prognostic marker and therapeutic target. *Mol Oncol.* 2019 Sep;13(9):1898–912.
159. Wang Z, Shi Y, Ying C, Jiang Y, Hu J. Hypoxia-induced PLOD1 overexpression contributes to the malignant phenotype of glioblastoma via NF- $\kappa$ B signaling. *Oncogene.* 2021 Jan 8;
160. Gilkes DM, Bajpai S, Wong CC, Chaturvedi P, Hubbi ME, Wirtz D, et al. Procollagen lysyl hydroxylase 2 is essential for hypoxia-induced breast cancer metastasis. *Mol Cancer Res MCR.* 2013 May;11(5):456–66.
161. Xu W-H, Xu Y, Wang J, Tian X, Wu J, Wan F-N, et al. Procollagen-lysine, 2-oxoglutarate 5-dioxygenases 1, 2, and 3 are potential prognostic indicators in patients with clear cell renal cell carcinoma. *Aging.* 2019 Aug 25;11(16):6503–21.
162. Yang B, Zhao Y, Wang L, Zhao Y, Wei L, Chen D, et al. Identification of PLOD Family Genes as Novel Prognostic Biomarkers for Hepatocellular Carcinoma. *Front Oncol.* 2020;10:1695.
163. Jiang H, Guo W, Yuan S, Song L. PLOD1 Is a Prognostic Biomarker and Mediator of Proliferation and Invasion in Osteosarcoma. *BioMed Res Int.* 2020;2020:3418398.

164. Wu X, Xiang H, Cong W, Yang H, Zhang G, Wang Y, et al. PLOD1, a target of miR-34c, contributes to cell growth and metastasis via repressing LATS1 phosphorylation and inactivating Hippo pathway in osteosarcoma. *Biochem Biophys Res Commun*. 2020 Jun 18;527(1):29–36.
165. Gawel DR, Lee EJ, Li X, Lilja S, Matussek A, Schäfer S, et al. An algorithm-based meta-analysis of genome- and proteome-wide data identifies a combination of potential plasma biomarkers for colorectal cancer. *Sci Rep*. 2019 Oct 30;9(1):15575.
166. Li S-S, Lian Y-F, Huang Y-L, Huang Y-H, Xiao J. Overexpressing PLOD family genes predict poor prognosis in gastric cancer. *J Cancer*. 2020;11(1):121–31.
167. Wang D, Zhang S, Chen F. High Expression of PLOD1 Drives Tumorigenesis and Affects Clinical Outcome in Gastrointestinal Carcinoma. *Genet Test Mol Biomark*. 2018 Jun;22(6):366–73.
168. Honoré B, Vorum H. The CREC family, a novel family of multiple EF-hand, low-affinity Ca(2+)-binding proteins localised to the secretory pathway of mammalian cells. *FEBS Lett*. 2000 Jan 21;466(1):11–8.
169. Nasri Nasrabadi P, Nayeri Z, Gharib E, Salmanipour R, Masoomi F, Mahjoubi F, et al. Establishment of a CALU, AURKA, and MCM2 gene panel for discrimination of metastasis from primary colon and lung cancers. *PloS One*. 2020;15(5):e0233717.
170. Mikula M, Rubel T, Karczmarski J, Goryca K, Dadlez M, Ostrowski J. Integrating proteomic and transcriptomic high-throughput surveys for search of new biomarkers of colon tumors. *Funct Integr Genomics*. 2011 Jun;11(2):215–24.
171. Das M, Das S. Identification of cytotoxic mediators and their putative role in the signaling pathways during docosahexaenoic acid (DHA)-induced apoptosis of cancer cells. *Apoptosis Int J Program Cell Death*. 2016 Dec;21(12):1408–21.
172. Tang H, Ma M, Dai J, Cui C, Si L, Sheng X, et al. miR-let-7b and miR-let-7c suppress tumorigenesis of human mucosal melanoma and enhance the sensitivity to chemotherapy. *J Exp Clin Cancer Res CR*. 2019 May 22;38(1):212.
173. Nagano K, Imai S, Zhao X, Yamashita T, Yoshioka Y, Abe Y, et al. Identification and evaluation of metastasis-related proteins, oxysterol binding protein-like 5 and calumenin, in lung tumors. *Int J Oncol*. 2015 Jul;47(1):195–203.
174. Mii S, Enomoto A, Shiraki Y, Taki T, Murakumo Y, Takahashi M. CD109: a multifunctional GPI-anchored protein with key roles in tumor progression and physiological homeostasis. *Pathol Int*. 2019 May;69(5):249–59.
175. Qi R, Dong F, Liu Q, Murakumo Y, Liu J. CD109 and squamous cell carcinoma. *J Transl Med*. 2018 Apr 6;16(1):88.
176. Mo X-T, Leung TH-Y, Tang HW-M, Siu MK-Y, Wan PK-T, Chan KK-L, et al. CD109 mediates tumorigenicity and cancer aggressiveness via regulation of EGFR and STAT3 signalling in cervical squamous cell carcinoma. *Br J Cancer*. 2020 Sep;123(5):833–43.
177. Hagikura M, Murakumo Y, Hasegawa M, Jijiwa M, Hagiwara S, Mii S, et al. Correlation of pathological grade and tumor stage of urothelial carcinomas with CD109 expression. *Pathol Int*. 2010 Nov;60(11):735–43.

178. Shiraki Y, Mii S, Enomoto A, Momota H, Han Y-P, Kato T, et al. Significance of perivascular tumour cells defined by CD109 expression in progression of glioma. *J Pathol.* 2017 Dec;243(4):468–80.
179. Minata M, Audia A, Shi J, Lu S, Bernstock J, Pavlyukov MS, et al. Phenotypic Plasticity of Invasive Edge Glioma Stem-like Cells in Response to Ionizing Radiation. *Cell Rep.* 2019 Feb 12;26(7):1893-1905.e7.
180. Silver DJ, Lathia JD. Revealing the glioma cancer stem cell interactome, one niche at a time. *J Pathol.* 2018 Mar;244(3):260–4.
181. Kim SY, Choi KU, Hwang C, Lee HJ, Lee JH, Shin DH, et al. Prognostic Significance of CD109 Expression in Patients with Ovarian Epithelial Cancer. *J Pathol Transl Med.* 2019 Jul;53(4):244–52.
182. Taki T, Shiraki Y, Enomoto A, Weng L, Chen C, Asai N, et al. CD109 regulates in vivo tumor invasion in lung adenocarcinoma through TGF- $\beta$  signaling. *Cancer Sci.* 2020 Dec;111(12):4616–28.
183. Lee K-Y, Kuo T-C, Chou C-M, Hsu W-J, Lee W-C, Dai J-Z, et al. Upregulation of CD109 Promotes the Epithelial-to-Mesenchymal Transition and Stemness Properties of Lung Adenocarcinomas via Activation of the Hippo-YAP Signaling. *Cells.* 2020 Dec 25;10(1).
184. Lee K-Y, Shueng P-W, Chou C-M, Lin B-X, Lin M-H, Kuo D-Y, et al. Elevation of CD109 promotes metastasis and drug resistance in lung cancer via activation of EGFR-AKT-mTOR signaling. *Cancer Sci.* 2020 May;111(5):1652–62.
185. Chuang C-H, Greenside PG, Rogers ZN, Brady JJ, Yang D, Ma RK, et al. Molecular definition of a metastatic lung cancer state reveals a targetable CD109-Janus kinase-Stat axis. *Nat Med.* 2017 Mar;23(3):291–300.
186. Ohtani-Kaneko R. Crmp4-KO Mice as an Animal Model for Investigating Certain Phenotypes of Autism Spectrum Disorders. *Int J Mol Sci.* 2019 May 20;20(10).
187. Gao X, Mao Y-H, Xiao C, Li K, Liu W, Li L-Y, et al. Calpain-2 triggers prostate cancer metastasis via enhancing CRMP4 promoter methylation through NF- $\kappa$ B/DNMT1 signaling pathway. *The Prostate.* 2018 Jun;78(9):682–90.
188. Li B, Li C. Suppression of Prostate Cancer Metastasis by DPYSL3-Targeted saRNA. *Adv Exp Med Biol.* 2017;983:207–16.
189. Li C, Jiang W, Hu Q, Li L-C, Dong L, Chen R, et al. Enhancing DPYSL3 gene expression via a promoter-targeted small activating RNA approach suppresses cancer cell motility and metastasis. *Oncotarget.* 2016 Apr 19;7(16):22893–910.
190. Li K, Pang J, Cheng H, Liu W-P, Di J-M, Xiao H-J, et al. Manipulation of prostate cancer metastasis by locus-specific modification of the CRMP4 promoter region using chimeric TALE DNA methyltransferase and demethylase. *Oncotarget.* 2015 Apr 30;6(12):10030–44.
191. Gao X, Li L-Y, Rassler J, Pang J, Chen M-K, Liu W-P, et al. Prospective Study of CRMP4 Promoter Methylation in Prostate Biopsies as a Predictor For Lymph Node Metastases. *J Natl Cancer Inst.* 2017 Jan;109(6).
192. Oya H, Kanda M, Sugimoto H, Shimizu D, Takami H, Hibino S, et al. Dihydropyrimidinase-like 3 is a putative hepatocellular carcinoma tumor suppressor. *J Gastroenterol.* 2015 May;50(5):590–600.

193. Tan F, Wahdan-Alaswad R, Yan S, Thiele CJ, Li Z. Dihydropyrimidinase-like protein 3 expression is negatively regulated by MYCN and associated with clinical outcome in neuroblastoma. *Cancer Sci.* 2013 Dec;104(12):1586–92.
194. Ma C-G, Xu W-H, Xu Y, Wang J, Liu W-R, Cao D-L, et al. Identification and validation of novel metastasis-related signatures of clear cell renal cell carcinoma using gene expression databases. *Am J Transl Res.* 2020;12(8):4108–26.
195. Chen S-L, Cai S-R, Zhang X-H, Li W-F, Zhai E-T, Peng J-J, et al. Targeting CRMP-4 by lentivirus-mediated RNA interference inhibits SW480 cell proliferation and colorectal cancer growth. *Exp Ther Med.* 2016 Oct;12(4):2003–8.
196. Chen S, Zhang X, Peng J, Zhai E, He Y, Wu H, et al. VEGF promotes gastric cancer development by upregulating CRMP4. *Oncotarget.* 2016 Mar 29;7(13):17074–86.
197. Kanda M, Nomoto S, Oya H, Shimizu D, Takami H, Hibino S, et al. Dihydropyrimidinase-like 3 facilitates malignant behavior of gastric cancer. *J Exp Clin Cancer Res CR.* 2014 Aug 6;33:66.
198. Kawahara T, Hotta N, Ozawa Y, Kato S, Kano K, Yokoyama Y, et al. Quantitative proteomic profiling identifies DPYSL3 as pancreatic ductal adenocarcinoma-associated molecule that regulates cell adhesion and migration by stabilization of focal adhesion complex. *PLoS One.* 2013;8(12):e79654.
199. Xing P, Liao Z, Ren Z, Zhao J, Song F, Wang G, et al. Roles of low-density lipoprotein receptor-related protein 1 in tumors. *Chin J Cancer.* 2016 Jan 6;35:6.
200. Montel V, Gaultier A, Lester RD, Campana WM, Gonias SL. The low-density lipoprotein receptor-related protein regulates cancer cell survival and metastasis development. *Cancer Res.* 2007 Oct 15;67(20):9817–24.
201. Gonias SL, Karimi-Mostowfi N, Murray SS, Mantuano E, Gilder AS. Expression of LDL receptor-related proteins (LRPs) in common solid malignancies correlates with patient survival. *PLoS One.* 2017;12(10):e0186649.
202. Gheysarzadeh A, Ansari A, Emami MH, Razavi AE, Mofid MR. Over-expression of low-density lipoprotein receptor-related Protein-1 is associated with poor prognosis and invasion in pancreatic ductal adenocarcinoma. *Pancreatol Off J Int Assoc Pancreatol IAP AI.* 2019 Apr;19(3):429–35.
203. Feng C, Ding G, Ding Q, Wen H. Overexpression of low density lipoprotein receptor-related protein 1 (LRP1) is associated with worsened prognosis and decreased cancer immunity in clear-cell renal cell carcinoma. *Biochem Biophys Res Commun.* 2018 Sep 10;503(3):1537–43.
204. An Q, Zhou L, Xu N. Long noncoding RNA FOXD2-AS1 accelerates the gemcitabine-resistance of bladder cancer by sponging miR-143. *Biomed Pharmacother Biomedicine Pharmacother.* 2018 Jul;103:415–20.
205. Lee KJ, Ko EJ, Park Y-Y, Park SS, Ju EJ, Park J, et al. A novel nanoparticle-based theranostic agent targeting LRP-1 enhances the efficacy of neoadjuvant radiotherapy in colorectal cancer. *Biomaterials.* 2020 Oct;255:120151.
206. Le CC, Bennisroune A, Collin G, Hachet C, Lehrter V, Rioult D, et al. LRP-1 Promotes Colon Cancer Cell Proliferation in 3D Collagen Matrices by Mediating DDR1 Endocytosis. *Front Cell Dev Biol.* 2020;8:412.

207. Fayard B, Bianchi F, Dey J, Moreno E, Djaffer S, Hynes NE, et al. The serine protease inhibitor protease nexin-1 controls mammary cancer metastasis through LRP-1-mediated MMP-9 expression. *Cancer Res.* 2009 Jul 15;69(14):5690–8.
208. Appert-Collin A, Bennisroune A, Jeannesson P, Terryn C, Fuhrmann G, Morjani H, et al. Role of LRP-1 in cancer cell migration in 3-dimensional collagen matrix. *Cell Adhes Migr.* 2017 Jul 4;11(4):316–26.
209. Salama Y, Lin S-Y, Dhahri D, Hattori K, Heissig B. The fibrinolytic factor tPA drives LRP1-mediated melanoma growth and metastasis. *FASEB J Off Publ Fed Am Soc Exp Biol.* 2019 Mar;33(3):3465–80.
210. Gilardoni MB, Remedi MM, Oviedo M, Dellavedova T, Sarría JP, Racca L, et al. Differential expression of Low density lipoprotein Receptor-related Protein 1 (LRP-1) and matrix metalloproteinase-9 (MMP-9) in prostate gland: From normal to malignant lesions. *Pathol Res Pract.* 2017 Jan;213(1):66–71.
211. Huang X-Y, Shi G-M, Devbhandari RP, Ke A-W, Wang Y, Wang X-Y, et al. Low level of low-density lipoprotein receptor-related protein 1 predicts an unfavorable prognosis of hepatocellular carcinoma after curative resection. *PLoS One.* 2012;7(3):e32775.
212. Fex Svenningsen Å, Löring S, Sørensen AL, Huynh HUB, Hjäresen S, Martin N, et al. Macrophage migration inhibitory factor (MIF) modulates trophic signaling through interaction with serine protease HTRA1. *Cell Mol Life Sci CMLS.* 2017 Dec;74(24):4561–72.
213. Klose R, Adam MG, Weis E-M, Moll I, Wüsthube-Lausch J, Tetzlaff F, et al. Inactivation of the serine protease HTRA1 inhibits tumor growth by deregulating angiogenesis. *Oncogene.* 2018 Aug;37(31):4260–72.
214. Chien J, Aletti G, Baldi A, Catalano V, Muretto P, Keeney GL, et al. Serine protease HtrA1 modulates chemotherapy-induced cytotoxicity. *J Clin Invest.* 2006 Jul;116(7):1994–2004.
215. Lorenzi T, Lorenzi M, Altobelli E, Marzioni D, Mensà E, Quaranta A, et al. HtrA1 in human urothelial bladder cancer: a secreted protein and a potential novel biomarker. *Int J Cancer.* 2013 Dec 1;133(11):2650–61.
216. Zurawa-Janicka D, Wenta T, Jarzab M, Skorko-Glonek J, Glaza P, Gieldon A, et al. Structural insights into the activation mechanisms of human HtrA serine proteases. *Arch Biochem Biophys.* 2017 May 1;621:6–23.
217. Xiong Z, Fu Z, Shi J, Jiang X, Wan H. HtrA1 Down-regulation Induces Cisplatin Resistance in Colon Cancer by Increasing XIAP and Activating PI3K/Akt Pathway. *Ann Clin Lab Sci.* 2017 May;47(3):264–70.
218. Cheng H, Zhu H, Cao M, Lu C, Bao S, Pan Y. HtrA1 suppresses the growth of pancreatic cancer cells by modulating Notch-1 expression. *Braz J Med Biol Res Rev Bras Pesqui Medicas E Biol.* 2018 Nov 23;52(1):e7718.
219. Gagné A, Têtu B, Orain M, Turcotte S, Plante M, Grégoire J, et al. HtrA1 expression and the prognosis of high-grade serous ovarian carcinoma: a cohort study using digital analysis. *Diagn Pathol.* 2018 Aug 21;13(1):57.
220. Globus O, Evron T, Caspi M, Siman-Tov R, Rosin-Arbesfeld R. High-Temperature Requirement A1 (Htra1) - A Novel Regulator of Canonical Wnt Signaling. *Sci Rep.* 2017 Dec 21;7(1):17995.



221. Zurawa-Janicka D, Kobiela J, Slebioda T, Peksa R, Stanislawowski M, Wierzbicki PM, et al. Expression of HTRA Genes and Its Association with Microsatellite Instability and Survival of Patients with Colorectal Cancer. *Int J Mol Sci.* 2020 May 31;21(11).
222. Altobelli E, Latella G, Morroni M, Licini C, Tossetta G, Mazzucchelli R, et al. Low HtrA1 expression in patients with long-standing ulcerative colitis and colorectal cancer. *Oncol Rep.* 2017 Jul;38(1):418–26.
223. Wang W, Zhao M, Cui L, Ren Y, Zhang J, Chen J, et al. Characterization of a novel HDAC/RXR/HtrA1 signaling axis as a novel target to overcome cisplatin resistance in human non-small cell lung cancer. *Mol Cancer.* 2020 Sep 2;19(1):134.
224. Wu H, Ma S, Xiang M, Tong S. HTRA1 promotes transdifferentiation of normal fibroblasts to cancer-associated fibroblasts through activation of the NF- $\kappa$ B/bFGF signaling pathway in gastric cancer. *Biochem Biophys Res Commun.* 2019 Jun 30;514(3):933–9.
225. Vasta JD, Raines RT. Collagen Prolyl 4-Hydroxylase as a Therapeutic Target. *J Med Chem.* 2018 Dec 13;61(23):10403–11.
226. Xiong G, Deng L, Zhu J, Rychahou PG, Xu R. Prolyl-4-hydroxylase  $\alpha$  subunit 2 promotes breast cancer progression and metastasis by regulating collagen deposition. *BMC Cancer.* 2014 Jan 2;14:1.
227. Toss MS, Miligy IM, Gorringer KL, AlKawaz A, Khout H, Ellis IO, et al. Prolyl-4-hydroxylase A subunit 2 (P4HA2) expression is a predictor of poor outcome in breast ductal carcinoma in situ (DCIS). *Br J Cancer.* 2018 Dec;119(12):1518–26.
228. Gilkes DM, Bajpai S, Chaturvedi P, Wirtz D, Semenza GL. Hypoxia-inducible factor 1 (HIF-1) promotes extracellular matrix remodeling under hypoxic conditions by inducing P4HA1, P4HA2, and PLOD2 expression in fibroblasts. *J Biol Chem.* 2013 Apr 12;288(15):10819–29.
229. Cao Y, Han Q, Li J, Jia Y, Zhang R, Shi H. P4HA2 contributes to cervical cancer progression via inducing epithelial-mesenchymal transition. *J Cancer.* 2020;11(10):2788–99.
230. Li Q, Wang Q, Zhang Q, Zhang J, Zhang J. Collagen prolyl 4-hydroxylase 2 predicts worse prognosis and promotes glycolysis in cervical cancer. *Am J Transl Res.* 2019;11(11):6938–51.
231. Reis PP, Tokar T, Goswami RS, Xuan Y, Sukhai M, Seneda AL, et al. A 4-gene signature from histologically normal surgical margins predicts local recurrence in patients with oral carcinoma: clinical validation. *Sci Rep.* 2020 Feb 3;10(1):1713.
232. Chang K-P, Yu J-S, Chien K-Y, Lee C-W, Liang Y, Liao C-T, et al. Identification of PRDX4 and P4HA2 as metastasis-associated proteins in oral cavity squamous cell carcinoma by comparative tissue proteomics of microdissected specimens using iTRAQ technology. *J Proteome Res.* 2011 Nov 4;10(11):4935–47.
233. Kisoda S, Shao W, Fujiwara N, Mouri Y, Tsunematsu T, Jin S, et al. Prognostic value of partial EMT-related genes in head and neck squamous cell carcinoma by a bioinformatic analysis. *Oral Dis.* 2020 Apr 11;
234. Lei Y, Yan W, Lin Z, Liu J, Tian D, Han P. Comprehensive analysis of partial epithelial mesenchymal transition-related genes in hepatocellular carcinoma. *J Cell Mol Med.* 2021 Jan;25(1):448–62.

235. Wang T, Fu X, Jin T, Zhang L, Liu B, Wu Y, et al. Aspirin targets P4HA2 through inhibiting NF- $\kappa$ B and LMCD1-AS1/let-7g to inhibit tumour growth and collagen deposition in hepatocellular carcinoma. *EBioMedicine*. 2019 Jul;45:168–80.
236. Atkinson A, Renziehausen A, Wang H, Lo Nigro C, Lattanzio L, Merlano M, et al. Collagen Prolyl Hydroxylases Are Bifunctional Growth Regulators in Melanoma. *J Invest Dermatol*. 2019 May;139(5):1118–26.
237. Pankova D, Jiang Y, Chatzifrangkeskou M, Vendrell I, Buzzelli J, Ryan A, et al. RASSF1A controls tissue stiffness and cancer stem-like cells in lung adenocarcinoma. *EMBO J*. 2019 Jul 1;38(13):e100532.
238. Fang C, Li X, Liang H, Xue L, Liu L, Yang C, et al. Downregulation of SUMF2 gene in ovalbumin-induced rat model of allergic inflammation. *Int J Clin Exp Pathol*. 2015 Oct 1;8(10):12053–63.
239. Zito E, Fraldi A, Pepe S, Annunziata I, Kobinger G, Di Natale P, et al. Sulfatase activities are regulated by the interaction of the sulfatase-modifying factor 1 with SUMF2. *EMBO Rep*. 2016 Dec;17(12):1901.
240. Mariappan M, Preusser-Kunze A, Balleininger M, Eiselt N, Schmidt B, Gande SL, et al. Expression, Localization, Structural, and Functional Characterization of pFGE, the Paralog of the C $\alpha$ -Formylglycine-generating Enzyme \*. *J Biol Chem*. 2005 Apr 15;280(15):15173–9.
241. Liang Y, Jiang L, Zhong X, Hochwald SN, Wang Y, Huang L, et al. Discovery of Aberrant Alteration of Genome in Colorectal Cancer by Exome Sequencing. *Am J Med Sci*. 2019 Nov;358(5):340–9.

## 8 APPENDIX

**Table 8: Cell concentrations for 3D culture seeding**

<b>Cell count per well</b>	<b>Cell concentration [cells/ml]</b>
100	$10^3$
200	$2 \times 10^3$
500	$5 \times 10^3$
800	$8 \times 10^3$
1000	$10^4$
2500	$2.5 \times 10^4$
3000	$3 \times 10^4$
5000	$5 \times 10^4$
10000	$10^5$
15000	$1.5 \times 10^5$
20000	$2 \times 10^5$
25000	$2.5 \times 10^5$
30000	$3 \times 10^5$
35000	$3.5 \times 10^5$
40000	$4 \times 10^5$
50000	$5 \times 10^5$

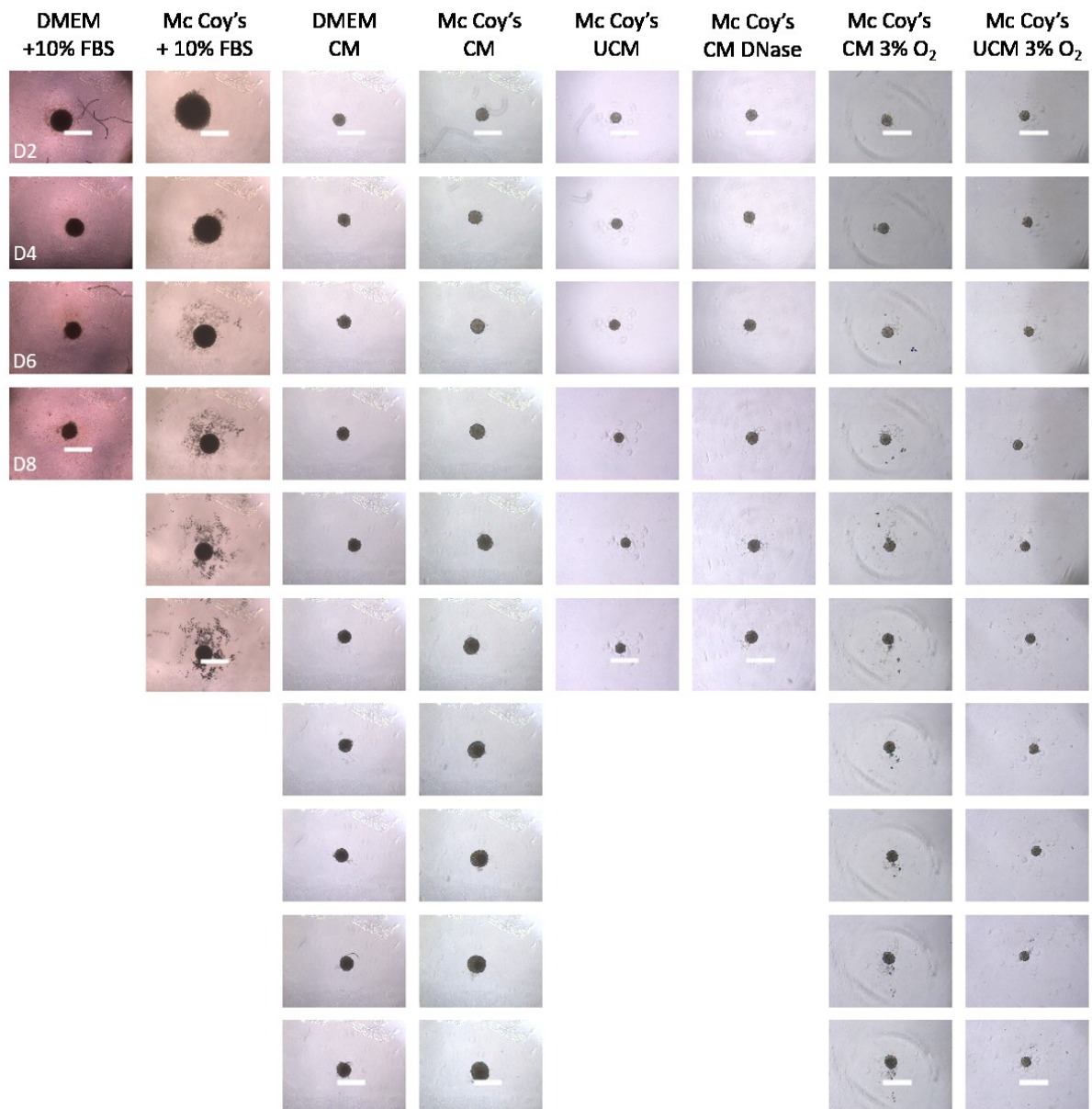


**Figure 16: 3D spheroid formation of UROtsa cell line under different medium conditions**

The cell line UROtsa was seeded onto 96-well ULA plates under different medium conditions. Half of the medium was changed every 2<sup>nd</sup> day and light microscopic images were taken daily. Scale bar = 500µm; magnification = 5x.



**Figure 17: 3D spheroid formation of RT4 cell line under different medium conditions**

The cell line RT4 was seeded onto 96-well ULA plates under different medium conditions. Half of the medium was changed every 2<sup>nd</sup> day and light microscopic images were taken daily. Scale bar = 500µm; magnification = 5x.

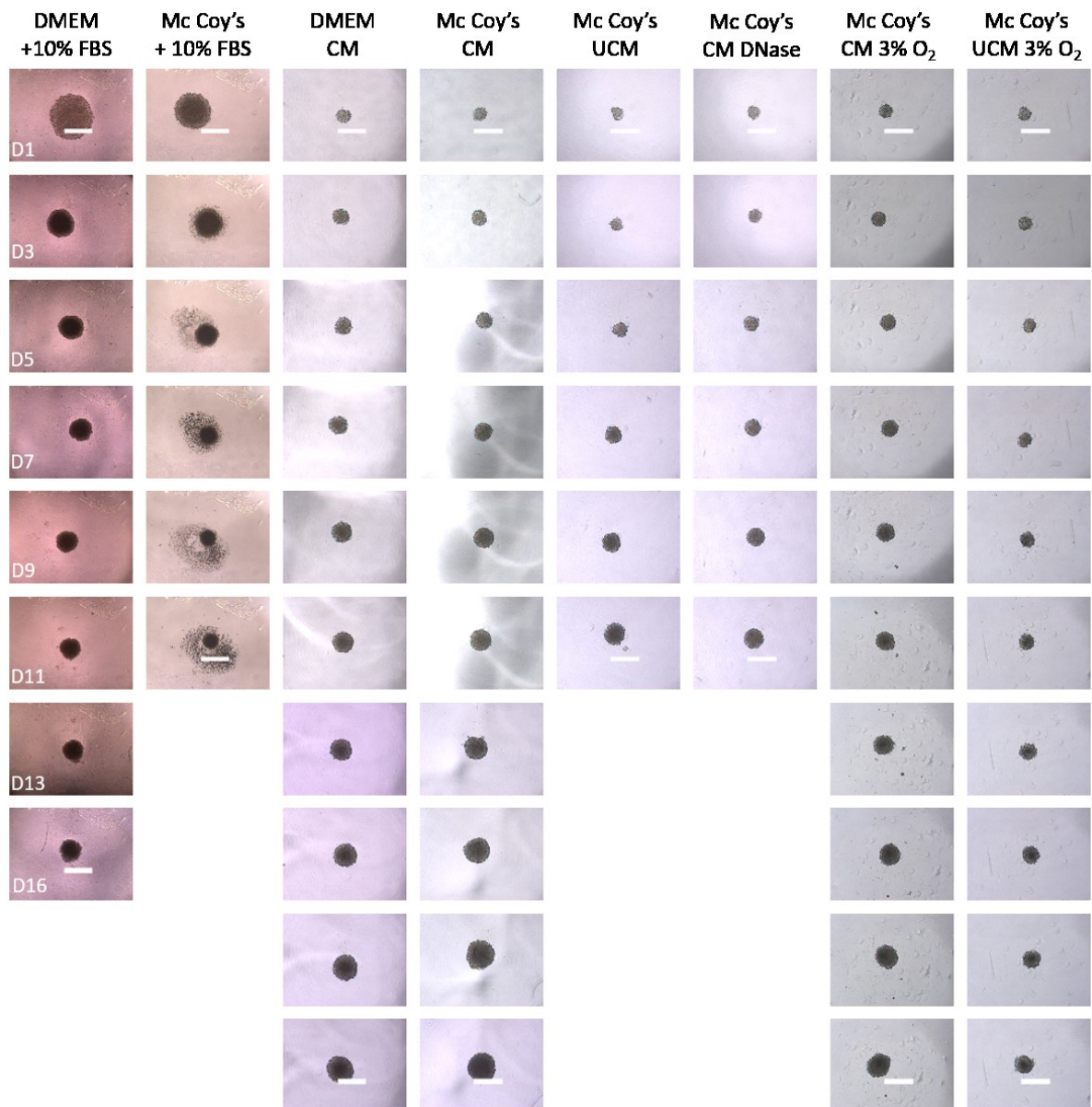


**Figure 18: 3D spheroid formation of T24/83 cell line under different medium conditions**

The cell line T24/83 was seeded onto 96-well ULA plates under different medium conditions. Half of the medium was changed every 2<sup>nd</sup> day and light microscopic images were taken daily. Scale bar = 500µm; magnification = 5x.



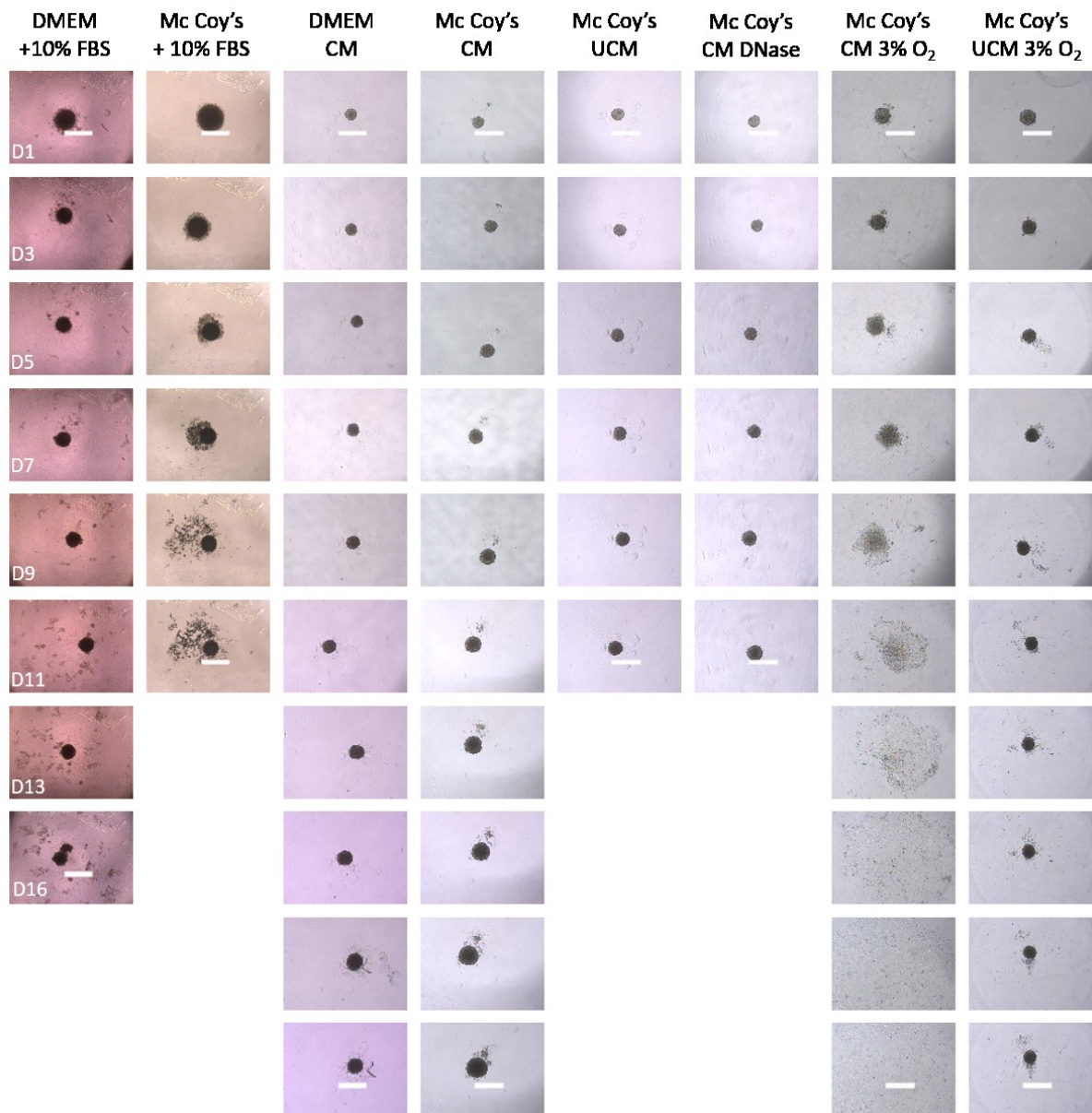


**Figure 19: 3D spheroid formation of SCaBER cell line under different medium conditions**

The cell line SCaBER was seeded onto 96-well ULA plates under different medium conditions. Half of the medium was changed every 2<sup>nd</sup> day and light microscopic images were taken daily. Scale bar = 500µm; magnification = 5x.

RT4 vs 2D Mc Coy's

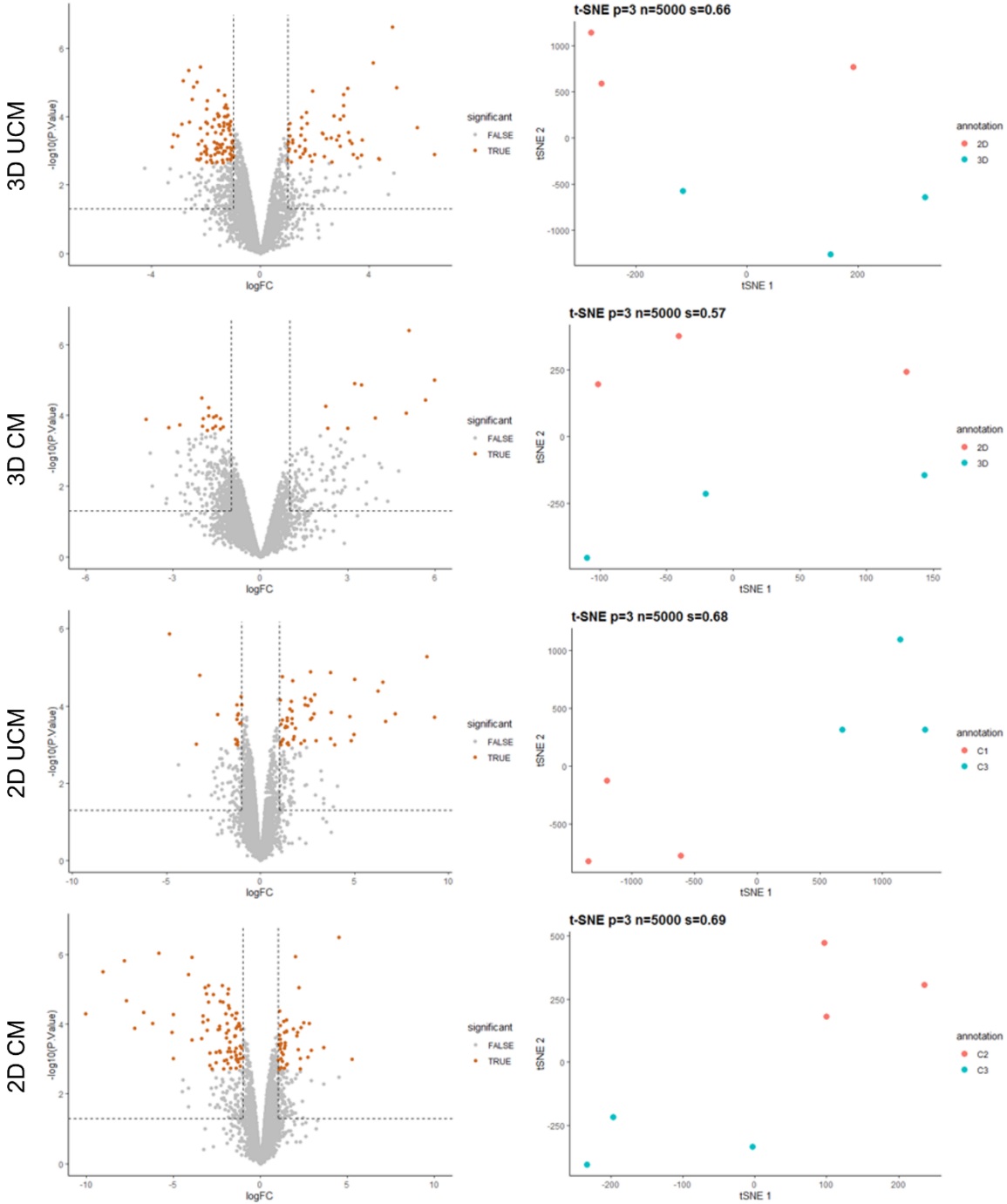
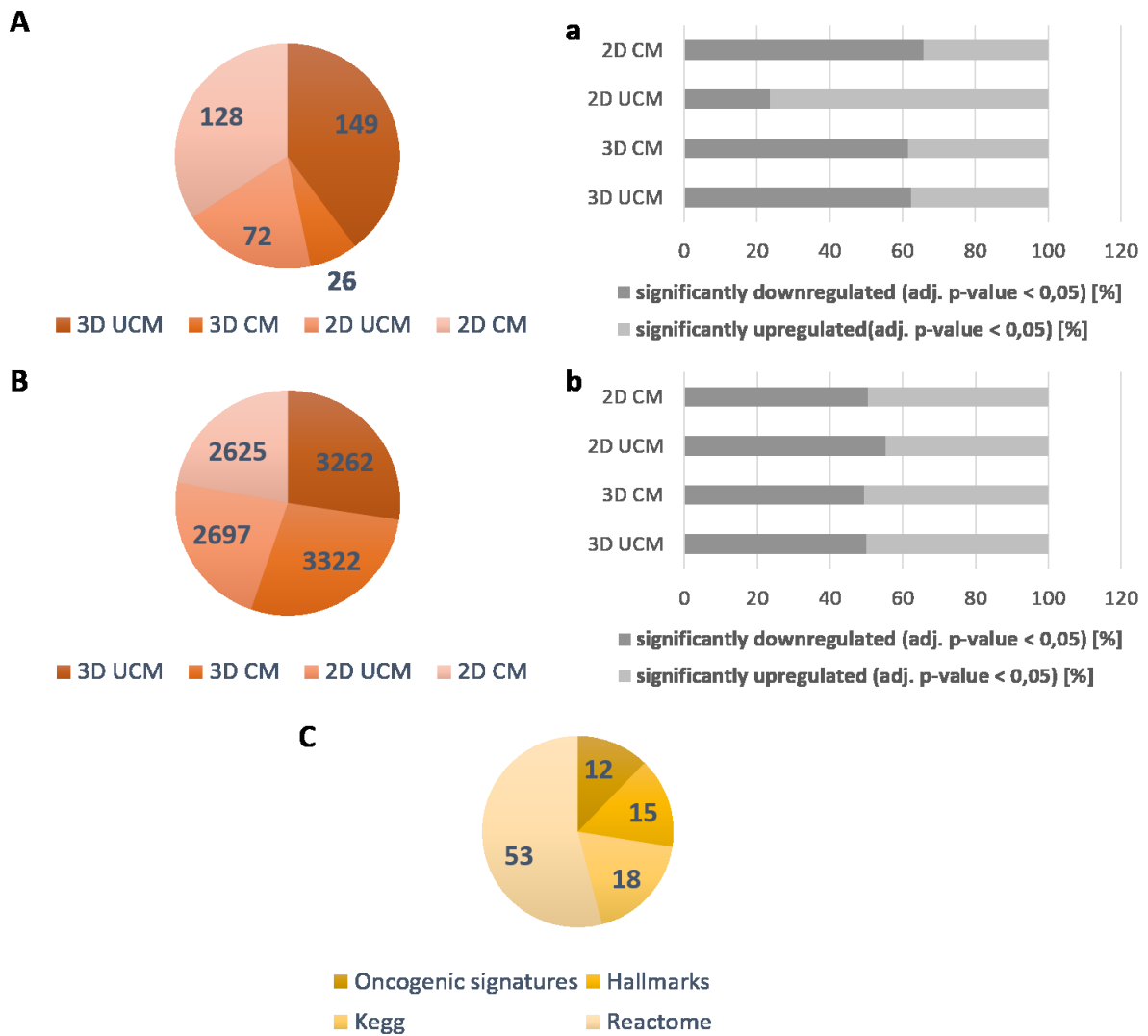


Figure 20: Volcano plot and related t-SNE annotation of DEP for RT4

DEP for RT4 were analyzed by limma statistics and displayed by volcano and t-SNE plot. The comparison of the 3D model (UCM and CM), and 2D model (UCM and CM), in contrast to the 2D standard condition (Mc Coy's+10% FBS) was conducted. A brown data point of the volcano plot represents one significantly DEP within the particular comparison. C1 (2D UCM); C2 (2D CM); C3 (2D Mc Coy's+10% FBS); 2D (2D Mc Coy's+10% FBS).





**Figure 21: Counts of significantly DEP and DEG in RT4 in relation to the 2D standard condition**

Significantly DEP (A) and DEG (B) for RT4 were analyzed by limma statistics and one-way ANOVA, respectively. The comparison of the 3D model (UCM and CM), and 2D model (UCM and CM), in contrast to the 2D standard condition (Mc Coy's+10% FBS) was conducted. Further, the proportion of up- and downregulated, significantly DEP (a) and DEG (b) is shown. The GSEA analysis was performed by the use of Kegg, Reactome, Hallmark, and oncogenic signatures gene sets, and the amount of significantly differential regulated pathways is given for each gene set database, detected for RT4 (C).

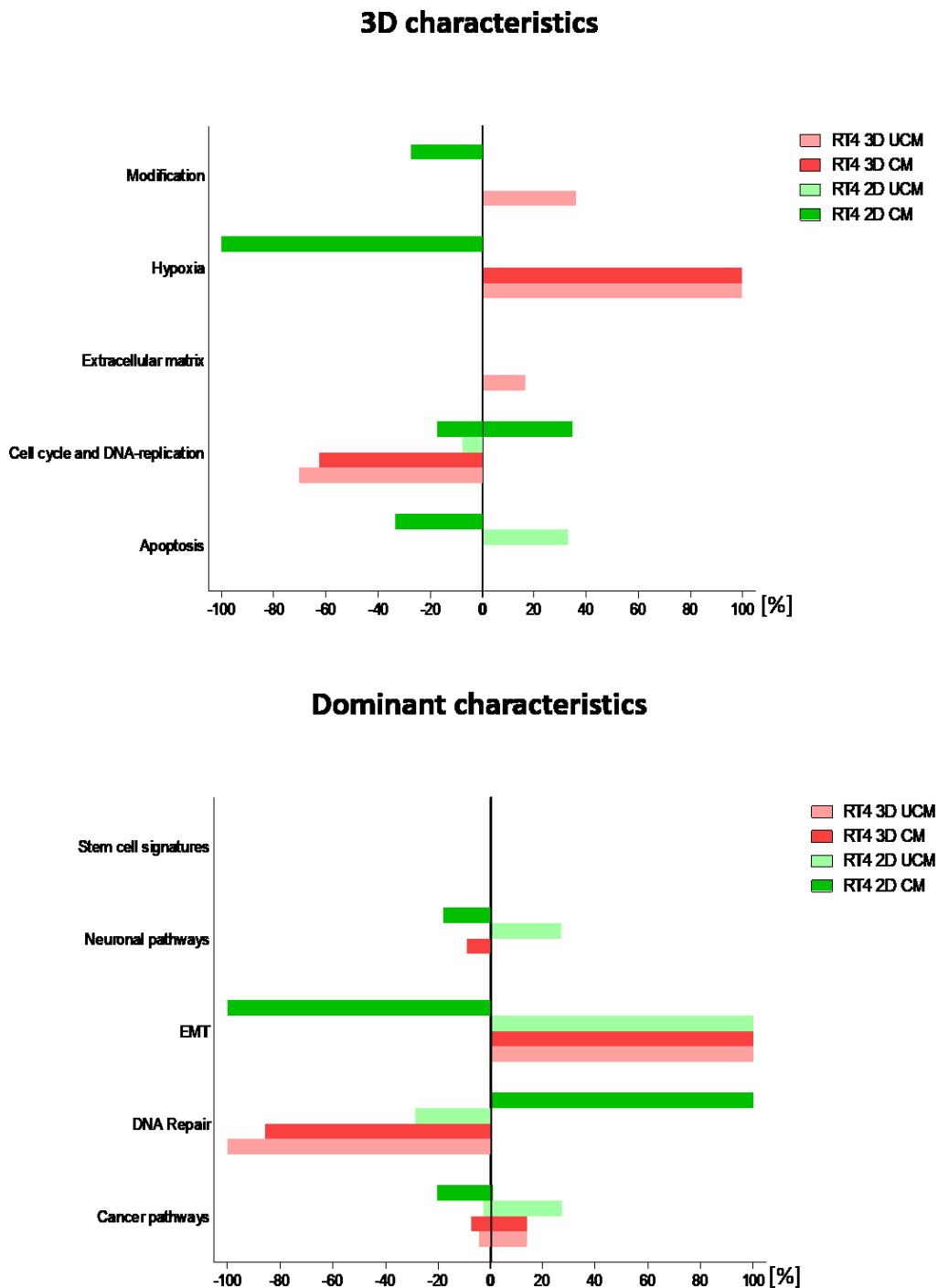


**Figure 22: GSEA outcome of biological functions for RT4 in relation to 2D standard condition**

Significantly, differential expressed gene sets have been grouped according to their biological function. Typical 3D characteristics (upper chart) and further dominant characteristics (lower chart) revealed for RT4. Each biological function plotted on the y-axis consists of functional related gene sets, which are shown as percentage depending if the gene set is significantly over- or under-representation.

## 9 CURRICULUM VITAE

### PERSONAL DATA

Name and first name: Wahby Sarah  
Date of birth: May 15<sup>th</sup> 1985  
Place of birth: Heidelberg  
Marital status: single  
Mother: Hewer-Wahby Monika  
Father: Wahby Farid

### SCHOOL CARRER

2004 - 2006 Johannes-Gutenberg-Schule Heidelberg in Germany  
07/04/2006 Subject-Related University Entrance Qualification  
State-certified Biotechnology Assistant

### ACADEMIC CARRER

SS2007 Bachelor of Science in Biological Chemistry  
Hochschule Mannheim – University of Applied Sciences  
2007 - 2012 "Optimization and standardization of the AChE assay for the  
detection of neurotoxic effects on zebrafish (*Danio rerio*) embryos"  
10/17/2012 Final grade: 1,8  
WS2014 Master of Science in Biomedical Science and Technology  
Hochschule Mannheim – University of Applied Sciences  
"Glycosyltransferase expression *in vivo* and glycocalyx profiling *in vitro*: An integrative analysis in muscle-invasive urothelial carcinoma of the bladder"  
2014 - 2016  
12/30/2016 Final grade: 1,4

## 10 ACKNOWLEDGEMENT

At this point, I would like to express my great gratitude to Prof. Dr. Michel for the excellent opportunities to work on this dissertation.

I would especially like to thank Prof. Dr. Erben and Prof. Dr. Hafner for providing me with the topic of this dissertation, their excellent supervision, and tremendous support in the implementation of the entire work.

I am also very thankful for the provision of the doctoral scholarship from the Albert and Anneliese Konanz Foundation.

A special thanks to Philipp, Annette and Katja who always believed in me in a professional and personal way and with whom I very appreciate to work with. Thank you so much for the great years working together. You are an amazing team and I will miss to work with you.

Greatly thanks to Carolina, Torsten and Florian for you time to implementing my measurements, as well as Fabian to introduce me into the world of programming. I very enjoyed the collaborative work with you guys.

Thanks to all the doctoral students who brought a lively atmosphere and a lot of fun to the lab. Especially thank you Vanessa for deep scientific and private discussions during breaks, and thank you Minca for your great collaboration. I very appreciate to supervise your thesis.

To my family, especially Monika and Karim, and to my friends, especially Julia, Niki, Christiane, Linda and Christin, I thank you for your constant encouragement, presence, and understanding during this special time in my life. I am looking forward to spend more time with you in future.

Ronja, Grace, Paula, Tony and Eddy, I am extremely grateful for you. You always cheered me up whenever we met so the earth stopped turning once in a while.